Synthesis and characterisation of high silica zeolites for methane reforming

Sian Elizabeth Woodfine

Doctor of Philosophy in Chemistry

18 March 2020

Abstract

In this study, the ability of the MTBA cation to effectively direct the formation of the nanosized MFI framework was present for the first time. Two nanosized materials from different SDAs were synthesised and investigated with a variety of different analytical techniques to ascertain the mechanism of formation. X-ray diffraction and dynamic light scattering studies showed varying results between the TPA and MTBA SDAs used, with the TPA templated material suggesting rapid crystallisation and the MTBA template material suggesting an aggregation mechanism. ^{13}C and ^{29}Si SSNMR studies of both materials suggest a spontaneous crystallisation mechanism is taking place. Conclusive evidence of a mechanism of formation was not observed, however it was concluded that the most likely mechanism was that of spontaneous rapid crystallisation. Further work into the mechanism of crystallisation needs to be conducted with a focus on size control and the effect of the SDA used.

The effect of crystallite size and framework topology on the catalysis of methane reforming was also studied using incorporated nickel as the active species. The catalytic activities for a nano sized and a micron sized nickel containing MFI zeolite were tested. The nano sized material was found to have a higher activity for the partial oxidation of methane, whereas the micron sized material was found to have a higher activity for the biogas reforming of methane. The catalytic activity for nickel containing MEL and MTW type materials was also tested. The MTW material showed a much higher activity for all methane reforming when compared to the MEL material. For the partial oxidation of methane, the MTW nickel containing material showed the highest activity, and for biogas reforming the micron sized MFI material showed the highest activity. It was concluded that the zeolite framework plays an important role in the catalysis of methane reforming and is not simply acting as a support for the active nickel species as the non- ‘doped’ materials show no catalytic activity. The effect of crystallite size is not shown to be equal for all reforming reactions. Further work into the location and activity of the nickel species with the framework needs to be conducted along with additional investigations into the wide variety of framework topologies available.

Table of Contents

List of Figures, Tables and Equations

Chapter 1.0

Chapter 2.0

Chapter 3.0

Chapter 4.0

Chapter 5.0

Chapter 6.0 Figures

Abbreviations

^{13}C {^{1}H} NMR	Proton decoupled carbon nuclear magnetic resonance
AlPO	Aluminium phophates
B_0	Magnitude of the magnetic field used for NMR
BEA	Zeolite type beta
Biogas	Methane reforming using a 2:1 mixture of methane to carbon dioxide
CP MAS NMR resonance	Cross-polarised magic angle spinning nuclear magnetic
DC	Direct current
DLS	Dynamic light scattering
EXDS	Energy-dispersive X-ray spectroscopy
FWHM	Full width at half maximum
GaPO	Gallium phosphates
IZA	International zeolite association
MEL	Zeolite type MEL
MFI	Zeolite type MFI (Mordenite framework inverted)
$MTBA^+$	Methyl tributyl ammonium cation
MTW	Zeolite type MTW
PBU	Primary building unit
POx	Partial oxidation of methane
PXRD	Powder X-ray diffraction
Q3/Q4	Notation for Si atoms linked to four oxygen atoms, with the number describing the number of Si units attached through oxygen sharing
Q_8M_8	Octakis(trimethylsiloxy)silsesquioxane
QMS	Quadrupole mass spectrometer
REDOR NMR	Rotation echo double resonance nuclear magnetic resonance
RF	Radio frequency
SBU	Secondary building unit
SDA	Structure directing agent
SEM	Scanning electron microscope
SS NMR	Solid state nuclear magnetic resonance

Syn-gas	Synthesis gas
TEOS	Tetra ethyl orthosilicate
TMP^{2+}	Trimethylenebis (N-methyl, N-benzyl piperidinium)
TMS	Tetra methyl silane
TOx	Total oxidation of methane
TPA^{+}	Tetra propyl ammonium cation
TPO	Temperature programmed oxidation
TPR	Temperature programmed reduction
XAFS	X-ray absorption fine structure
XRD	X-ray diffraction
ZSM-5	Zeolite Socony Mobil–5
ZSM-11	Zeolite Socony Mobil–11
ZSM-12	Zeolite Socony Mobil–12

Acknowledgments

Life rarely affords us the opportunity to thank loved ones for simply helping us make it through, so I fully intend to grasp this one.

To my parents, thank you for your unending support, even during the small hours when I think the world is ending! You are my life and I love you.

To Dan, there are no words that could ever express my gratitude for you. You kept me moving forward and held me up along the way. I love you.

To Daniel, Keely and Lilah, thank you for providing the fun and distraction from the workload. I can’t wait see you build an amazing life together.

To Mandy, Matt, Clare and Mike, thank you for being my second family.

To Richard, thanks for this difficult but equally exciting ride. Thank you for your continued support for too many years to count, you're a saint for putting up with me this long. Most importantly thank you for your friendship.

To John, thank you for the never ending conversation, your wisdom of the world and chemistry and for the ridiculous debates about the wind and space and time.

To Drs Lucy and Shelley, thank you for allowing me to laugh, moan and cry (and everything in between).

To my lab rats, thank you for being the most fun people to work with, you make the dull exciting and the ridiculous hilarious.

And to anyone I may have forgotten, you'll have to forgive me this has been an awfully long journey and I think I need a good sleep!

I wish to dedicate this thesis to Sylvia Evans and Ray Spencer.

1.0 Background, theory and aims of the study

1.1 Zeolite Background and Structure

Zeolite is the name given to the group of microporous aluminosilicates that can be both synthetic and naturally occurring. The term zeolite originated in 1758 from Baron Axel Fredrik Cronstedt[1], a Swedish mineralogist, whom had discovered nickel seven years prior. The word zeolite comes from the Greek word 'zein' which means 'to boil', due to Cronstedt's observation of water loss on heating of the material, and 'lithos' meaning rock, as at the time zeolites were only known to be naturally occurring minerals[1].

These complex aluminosilicates are comprised of frameworks of linked tetrahedra, for which the central cation is Si^{4+} or Al^{3+} and the four corners are oxygen atoms[2]. This results in the neutral SiO_4 unit and the negatively charged $[AlO_4]^-$. These tetrahedra are linked via the sharing of the corner oxygen atoms, and as there are four corner atoms, one tetrahedron can be linked to four others through this atom sharing[2]. This connectivity of tetrahedra gives rise to a complex, three dimensional, connected framework. As the tetrahedra have four points of linkage they are able to connect in a variety of different conformations, leading to the formation of pores and channels within the framework[3]. With such opportunity for variation to occur, it is no wonder that as of December 2018 there are 239 confirmed different types of zeolite by the International Zeolite Association (IZA)[4], with each zeolite type is denoted by a three letter code given by the IZA structure commission. These three letter codes are only used to describe the framework type and not the chemical composition of the material.

There are now more purely synthetic zeolite types than there are naturally occurring. Today the word zeolite encompasses much more than just frameworks comprised of aluminium and silicon, it now describes pure silica frameworks as well as aluminium and gallium phosphates, AlPOs[5] and GaPOs[6]. Examples are shown in Figure 1.1.

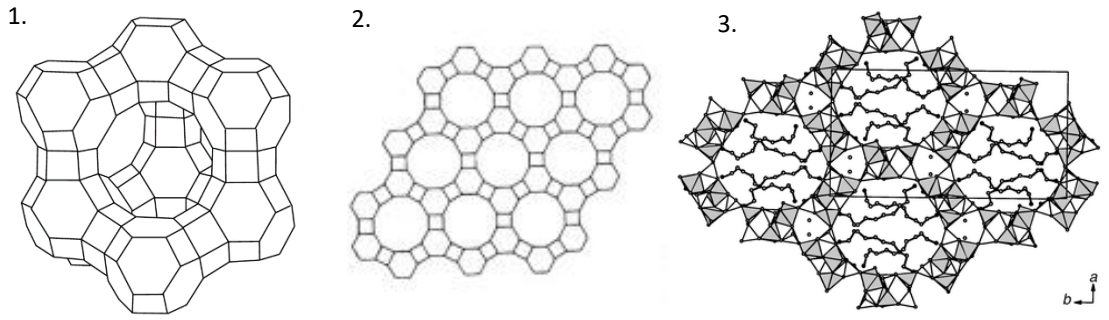

Figure 1.1. Framework structues of 1. Zeolite A[7], 2. AlPO4-5[5], 3. GaPO- MEL-5[6].

Naturally occurring zeolites can be found within both igneous and sedimentary rocks. They are thought to have been formed under high pressure and temperature and to have crystallised very slowly over many thousands of years. These natural zeolites are rarely found in their pure form and are often present with other minerals and metals.

The pores and channels within the zeolite framework, commonly between 3 and 15Å in diameter, connect to give a molecular-sized labyrinth, which is able to take in small molecules such as water and other 'guest molecules'. This ability to take in small molecules is why many refer to zeolites as 'molecular sieves', due to the fact it can separate smaller molecules from larger ones.

The general way of expressing a zeolite composition is $M_x(Si_{1-x}+Al_x)O_2.zH_2O$, where M is a cation with either a +1 or +2 charge. This 'M' cation, commonly Na^+, Ca^{2+} or Mg^{2+}, plays the part of charge-balancing the material, a result of the negatively charged $[AlO_4]^-$ tetrahedra. The letter z in the general composition expression relates to the quantity of water occluded in the channels of the framework. This composition neglects the presence of so called structure directing agents (SDAs) within the pores and channels of the material (see Chapter 1.2).

Zeolites frameworks can be thought of as being comprised of small repeating units, called secondary building units (SBUs)[8]. These SBUs join together to form an extended network to give the final zeolite framework.

As zeolites do not have a distinctive size or number of connected SBUs, this extended network in theory could be infinitely large and still considered one molecule. There are many known secondary building units, the most common are shown in Figure 1.2, and are themselves formed of smaller primary building units (PBUs).

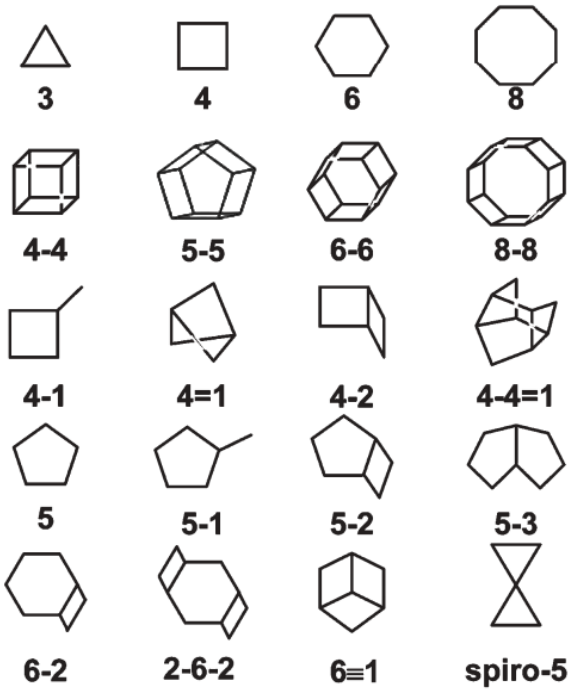

Figure 1.2. Common secondary building units found in zeolites. (Adapted from Morris, 2005[8].).

The crystal morphology between different zeolite types can be dramatically different, as shown in Figure 1.3.

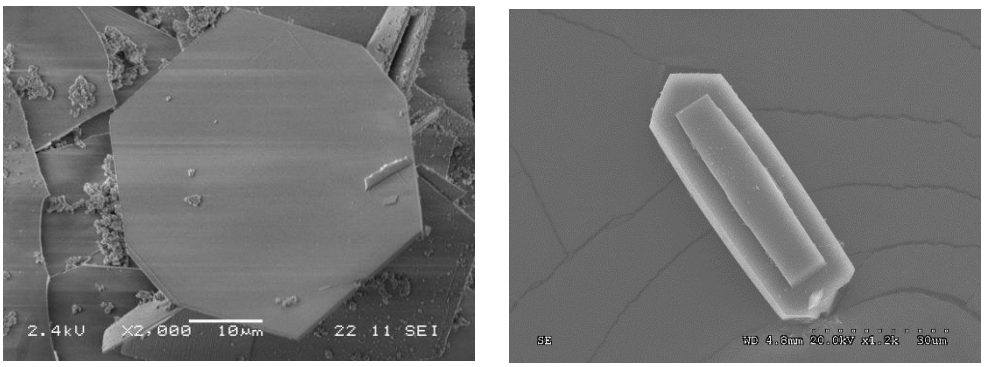

Figure 1.3. Zeolite crystal morphology, a sample of ferrierite is pictured left and an MFI-type zeolite is on the right[9].

This difference in morphology is a result of the gel composition, the kinetics of crystal growth, the nucleation process and the chemistry that is occurring on the crystal surface.

1.2 Synthesis of Zeolites

The synthesis of zeolites is a very well-studied area of materials chemistry. Due to their variety of different applications, discussed in Chapter 1.4, and their importance to many large industries, the knowledge of the synthesis of these porous materials is vital to efficiently utilising them. Early work into zeolite synthesis focussed on the production of analogues to naturally occurring zeolites. It was not until 1948 that the first fully synthetic zeolite was synthesised by Barrer[10-12], later identified as the framework type KFI.

1.2.1 Hydrothermal synthesis method

The most commonly utilised method of synthesis is the hydrothermal method, first developed in the 1940s by the Milton group[13]. This method involves the reactant mixture, usually a solution or gel, being placed in a Teflon-lined stainless steel autoclave and at a temperature of approximately 100 °C with an autogenous pressure. Average reaction times are approximately three days.

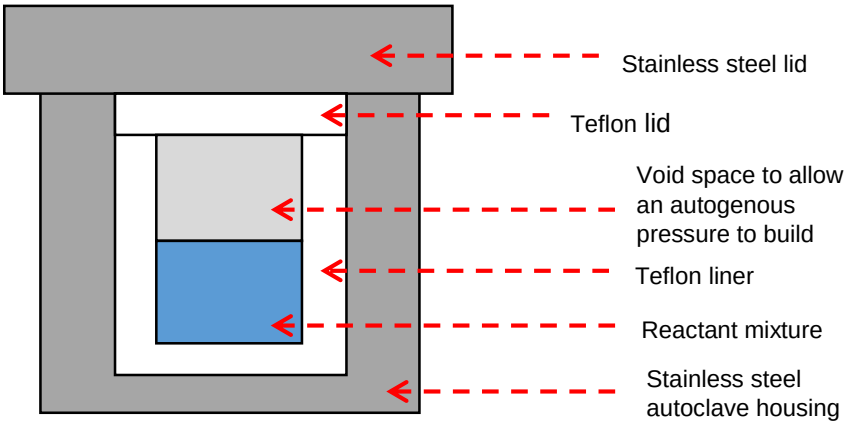

Figure 1.4. Schematic of a Teflon-lined stainless steel autoclave.

Prior to the implementation of the hydrothermal method, zeolite scientists aimed to replicate the high temperatures (> 200 °C) and pressures (> 100 bar) under the which the zeolite naturally forms. The development of the hydrothermal method allowed zeolite synthesis to become a much easier and less energy intensive process. Another significant development in synthetic zeolite chemistry was the utilisation of tetramethylammonium cations, first reported by Barrer and Denny[14,15]. The incorporation of these cations into the synthesis mixture gave rise to another level of control over the synthesis. These quaternary ammonium cations are commonly referred to as structure directing agents (SDAs) or templates. The organic structure directing agents operate as their name suggests and direct the formation of the framework structure during synthesis. These SDAs are commonly quaternary ammonium salts, where the length and configuration of the alkyl chains vary considerably for different zeolite types. Many zeolite types have multiple SDAs that can direct their formation[16,17].

A common zeolite synthesis now consists of a silica and/or alumina source, a structure directing agent, water and a mineralising agent. The purpose of the mineralising agent is to ensure that the semi-soluble silica and alumina sources are in solution. Many early syntheses relied on hydroxide ions, OH^-, to act as a mineraliser, however, this has the effect of elevating the pH of the reaction. It was not until 1976 that Flanigen and Patton[18] used fluoride ions in place of the hydroxide as the mineralising agent. This allowed syntheses to be carried out at a reduced pH. When used in a pure silica synthesis, the fluoride ions were noted to have another favourable effect, larger crystals with fewer framework defects were observed[18]. These defects arise from the incorporation of the OH^- ions into the framework to form SiOH which then leads to a charge imbalance. As these defects are observed less frequently when using a fluorinated synthesis mixture, the resulting zeolite crystals are often used as comparison materials for characterisation.

1.2.2 Clear solution synthesis method

Another method of synthesis is the clear-solution method, which is used to obtained nanosized zeolite crystals[19-21]. This method is commonly used to yield pure or high silica

nanozeolites. The hydrothermal method commonly yields crystals on the micron scale. This method has a standard reflux set up in which the temperature is around 100 °C and the pressure is limited to that of the room, i.e. 1 atmosphere. The zeolite product crystallises from a clear-colourless solution over a period of 1 to 2 weeks. As the reaction is placed under reflux, the reaction mixture differs to that used for the hydrothermal method, namely the silica source; it is not common for an alumina containing material to be synthesised in this manner. The silica source for a standard hydrothermal synthesis is fumed silica, as this is a dry powder that can also be used a thickening agent it is unsuitable for use in a reflux reaction. The alternative silica source is tetraethyl orthosilicate (TEOS) which upon addition to water forms a water soluble silicon dioxide and ethanol, see equation 1.1.

$$Si(C_2H_5O)_4 + 2\ H_2O \longrightarrow SiO_2 + 4\ C_2H_5OH \qquad \text{Equation 1.1}$$

For these clear solution reactions, the mineralising agent is often incorporated as part of the SDA, i.e. the quaternary ammonium cation will have a hydroxide anion. In the hydrothermal method this is not always the case, the anion is commonly a chloride ion, and the mineraliser is added as a separate species e.g. NaOH or NH_4F.

A benefit of the clear-solution method is that it is much easier to follow than the hydrothermal method, since the reaction occurs in standard glassware and at atmospheric pressure. Sampling of the reaction can be easily accomplished as the reaction does not have to be quenched by removing it from the heat source, a major drawback of the hydrothermal method.

The implementation of the clear-solution method and the ease in which it can be sampled, has given rise to a significant debate over the mechanism of formation of the zeolite framework. This has been most extensively studied by the group of Martens *et al.*[22-28] who have suggested that an aggregative mechanism occurs. They have proposed that the tetrahedra aggregate under the influence of the structure directing agent to form many silicate poly-anions such as the bicyclic pentamer, penta-cyclic octamer and the tetra-cyclic undecamer shown in Figure 1.5 along with others.

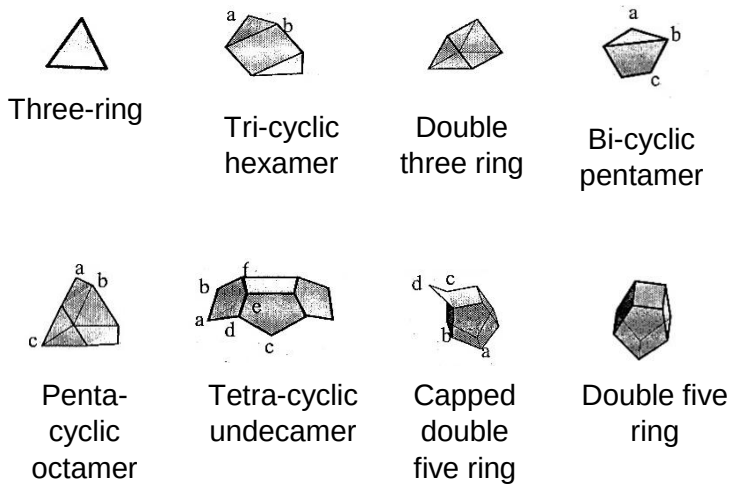

Figure 1.5. Structures of the various silicate poly-anions assigned by the Martens group from their obtained ^{29}Si solution NMR spectra. (Adapted from Kirschhock *et al*. 1999[22]).

These poly-anions are then thought to go through a poly-condensation process to selectively form a 33-atom tetrahedral precursor building unit. Four of these precursor building units are then said to aggregate to form a 'nanoslab'. These nanoslabs then further aggregate forming so-called 'nanoblocks'.

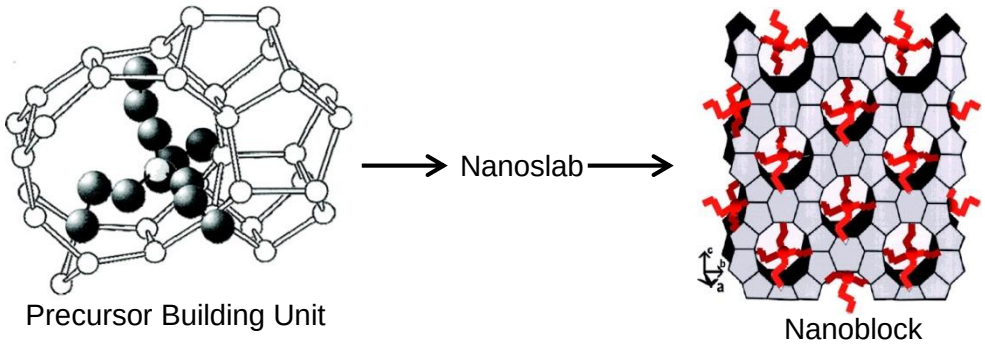

Figure 1.6. Schematic representation of the 33-atom tetrahedral precursor building unit and the process of aggregation to yield the nanoblock. Adapted from Fyfe *et al.* 2008[20].

Four nanoblocks are postulated to aggregate to form a tablet which then in turn keep aggregating to generate the extended framework of the zeolite. Previous successful syntheses have yielded crystals in a wide range of particle sizes from very small 10 nm

crystals to larger 1000 nm crystals. This variation in size is most likely due the variation in reaction conditions, such as temperature, and the overall length of time of the reaction.

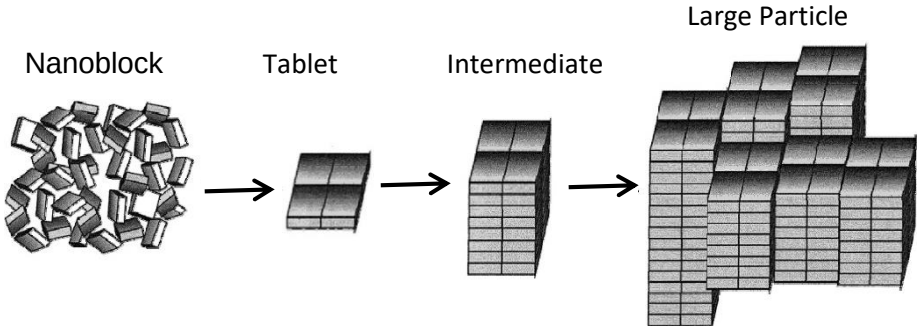

Figure 1.7. Schematic representation of the formation of the extended MFI framework from nanoblocks to the large framework particle. Adapted from Fyfe *et al.* 2008[20].

Despite the large amount of work presented by the group of Martens *et al.* on this topic, many other researchers studying this mechanism of formation are highly critical of the proposed aggregative mechanism[20,29-37]. These opposing groups cite low-angle X-ray and neutron diffraction as evidence that the most likely mechanism involves the formation of amorphous colloidal silica particles, which are thought to have some SDA anion trapped within them. The nano-sized zeolites are then thought to crystallise out from this solution. The high criticism of the proposed aggregative mechanism is evidenced in a comment from Knight and Kinrade[29] to the Martens group in which it is argued that the ^{29}Si spectral assignments of the resonances to the building unit and its polyanion precursors, shown in Figure 4, are in fact due to other, previously known structural units that are not mentioned in the paper. The criticism goes as far as to say that the "implications of the work in terms of understanding the molecular level mechanism of zeolite formation could not be more damaging"[29]. Fyfe *et al*[20]. conducted a study into the mechanism of formation of nanosized MFI type zeolite, using the tetrapropyl ammonium cation as a template. They utilised X-ray diffraction, particle size measurements and solid state NMR to characterise the material from various samples taken as the reaction proceeded. They also concluded that crystallisation was most likely from an amorphous gel.

It is therefore vital to investigate the mechanism of formation of the nanozeolite framework, to allow further conclusions to be drawn and to help ascertain which of the conflicting theories is most accurate.

1.3 Characterisation of Zeolites

A variety of different techniques are used to characterise zeolites, the main technique and the one that has been used since the 1940s is X-ray diffraction (XRD). The most commonly utilised X-ray diffraction technique is that of powder samples. Powder XRD (PXRD) allows the user to quickly identify if the material is crystalline and if a specific zeolite type has been formed. It has also been used to solve the structures of materials, including the all-silica ITQ-4[38]. More recently, single crystal XRD has been used to characterise materials[39] and to see if any changes are observed with changes in temperature. The use of single crystal X-ray diffraction does however rely on the availability of a suitably sized crystal sample for mounting.

To complement the use of X-ray diffraction, solid state NMR (SSNMR) can be utilised to help understand the local structure of the materials[40-42]. It should be noted however that SSNMR is not often used as the main characterisation technique for zeolites, this challenge is left to X-ray diffraction.

Microscopy, in particular scanning electron microscopy (SEM), is used to study the morphology, surface structure and particle size of the zeolites crystals. With SEM and its combination with energy-dispersive X-ray spectroscopy (EDXS) the elemental composition of the surface can be studied and elemental location ‘maps’ can be obtained to see if any incorporated elements are localised to a specific region.

The particle size of the materials can be measured through ‘viewing’ by SEM or if the material is too small, as could be the case with nanosized zeolites, dynamic light scattering (DLS) of zeolite suspensions can be used. DLS yields a particle size distribution of all material within the suspension so it is important to ensure that any amorphous starting

materials such as silica sources are completely removed before measurements are performed.

Other characterisation techniques that can be utilised are computational methods for modelling of reactions and for structure solving, neutron diffraction, in the same way as XRD, and infrared spectroscopy (IR), as it is sensitive to the zeolite type and the Si^{4+} to Al^{3+} ratio.

The most important aspect of characterisation of these porous materials is the complementary nature of these techniques in gaining a 'full picture'.

1.4 Applications of Zeolites

Due to the variety in terms of their crystal size, morphology and frameworks these porous materials have a vast selection of applications, with more being discovered every year. To name all of these applications would be beyond the scope of this thesis, however, the three main areas of application will be discussed, these are separation, ion exchange and heterogeneous catalysis.

As previously mentioned, zeolites are often referred to as 'molecular sieves', this term comes from one of their common applications of separation and are frequently used to separate gases from each other. As the porous system of the frameworks vary in size and shape, these materials can be selective with regards to the molecules that pass through them. This means they can be used to completely remove certain molecules from a mix or selectively increase the concentration of another. An example of a zeolite being used for separation is in the case of natural gas, for which they are utilised to remove water and other undesirable constituents from the stream of gas[43]. They can also be used to treated polluted water to remove contaminants such as arsenic[44] and ammonium cations[45].

Another common application of zeolites is that of ion exchange. As the frameworks carry a negative charge, due to the aluminium tetrahedra, they are capable of taking in and retaining a variety of different cations. One of the most widespread applications of zeolites being used for ion exchange is within washing powders. They are present in these commercially available products as water softeners which facilitate the formation of a lather.

This water softening is achieved by ion-exchanging Na^+ in the pore system with Ca^{2+} and Mg^{2+} from the water[46].

Heterogeneous catalysis is another area in which zeolites are commonly used. Again, this is mainly due to their diverse range of shapes and size of the pore system allowing them a selectivity towards certain products of reaction, but also because of their ability to hold a variety of different molecules. As the aluminium tetrahedra carry a negative charge, the framework is able to carry cations, such as H^+ ions. The intake of these charge balancing protons leads to the framework becoming highly acidic, which can then be utilised for acid catalysis. One of the most common and well-known examples of a zeolite being used for shape selective catalysis is that of ZSM-5 in the isomerisation of xylene[47]. ZSM-5 is an aluminosilicate zeolite of the MFI type framework. Zeolite Socony Mobil-5 (ZSM-5) was patented in 1972 by the Mobil Oil company[48] and is widely utilised in the petrochemical industry for isomerisation of hydrocarbons. For the catalysis of xylene isomerisation, from the meta to the *para* substituted isomer, ZSM-5 shows a shape selectivity towards the *para*-xylene product over its *ortho* and *meta* counterparts[47].

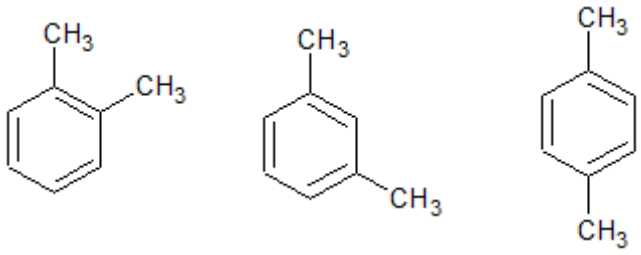

Figure 1.8. Structure of *ortho*-, *meta*- and *para*- xylene.

This is due to the shape of the *para* isomer, having a straighter and more streamlined structure, allowing it to diffuse through the pores of the zeolite more quickly than the other isomers. Another example of ZSM-5 being used in catalysis is that in acid-catalysed reactions. The charge balancing protons present within the framework lead to the formation of Brønsted acid sites which can then be utilised for cracking, isomerisation and alkylation of hydrocarbons in the petrochemical industry[49].

New applications, and improvements to existing ones will inevitably arise from the gaining of a deeper understanding of these materials, their structures and how they behave. This thesis aims to contribute knowledge to this aspect of zeolite science.

1.5 Heterogeneous catalysis

Heterogeneous catalysis, a common zeolite application, refers to the type of reaction in which the catalyst and reactants are in a different phase, commonly it is the catalyst in the solid state, and the reactants in the gaseous or liquid state. For these reactions, adsorption on the catalyst surface is usually the first step, this adsorption can be in the form of either physisorption, in which the adsorbate is attracted to the surface via van der Waals forces, or chemisorption, in which the adsorbate chemically bonds to the surface. There are three mechanisms of catalysis that are used to describe these surface reactions; the Langmuir-Hinshelwood mechanism[50], the Rideal-Eley mechanism[51] and the precursor mechanism[52]. These three mechanisms are depicted in Figure 1.9. In the Langmuir-Hinshelwood mechanism the reactant molecules (A and B) both adsorb to the surface, react to form the product (AB) and then desorb from the surface as the 'new' molecule (AB). The Rideal-Eley mechanism describes how only one of the reactant adsorbs onto the surface (A), the second molecule (B) then reacts with the adsorbed molecule without adsorbing to the surface itself, the resulting product (AB) then desorbs from the surface. The precursor mechanism, as the name suggests, involves the formation of a mobile precursor (MP). The first reactant molecule (A) adsorbs onto the surface, the second reactant molecule (B) then collides with the surface and forms a mobile precursor (MP), it is important to note that this does not involve the second molecule adsorbing to the surface and therefore results in its mobility. This mobile precursor (MP) then collides with the first reactant (A) adsorbed on the surface and the resulting product (AMP) desorbs. All three can occur in the reverse of how they are described and can also occur in combination with each other.

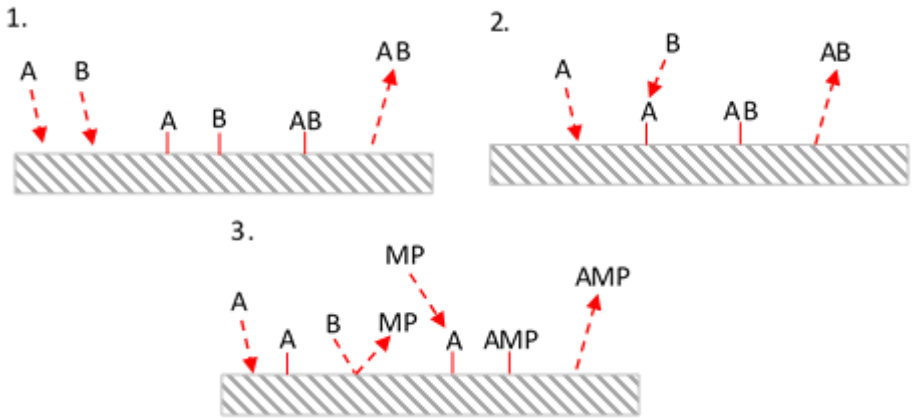

Figure 1.9. Depictions of the catalysis mechanisms 1. Langmuir-Hinshelwood 2. Rideal-Eley 3. the precursor mechanism. Where A and B are precursor molecules, AB is a product molecule, MP is a mobile precursor and AMP is a product molecule.

Heterogeneous catalysts can lose their ability to catalyse a reaction through a variety of processes, collectively known as deactivation[53]. These deactivation processes cause a change to the surface of the catalyst rendering it unable to adsorb as much as or any of the reactant molecules. A common mode of deactivation is carbon deposition, also known as coking, in which carbon or carbon rich substances are laid on the catalyst surface, blocking adsorption. Sintering of the catalyst material, in which the material is heated to the point of compaction but not to its melting point, can also lead to its deactivation as it results in a dramatic change to the surface[54]. Another method of deactivation is the poisoning of the catalyst by a compound binding to its surface e.g. sulphur[55]. It does so by blocking the surface of the catalyst to the adsorbate and again halting or diminishing reactant adsorption.

1.6 Reforming of methane

Methane reforming is the heterogeneously catalysed process by which hydrogen is produced. The production of hydrogen is a valuable process as it is utilised in many ways, including the Haber process for the production of ammonia and for use in combination with fuel cells to generate electricity[56].

The most common method of hydrogen production is the reforming of methane with steam, known as steam reforming[57]. Other methods of reforming can also be used, such as dry

reforming of methane with carbon dioxide[58] and partial oxidation (POx) of methane in the presence of oxygen[59]. These reactions result in the formation of synthesis gas (syn-gas), a variable mixture of hydrogen and carbon monoxide.

In comparison to other hydrogen production methods mentioned, steam reforming yields the largest H_2:CO ratio which is very clearly beneficial. The equations of reaction for steam reforming and steam reforming with an excess of steam are shown below in Equations 1.2 and 1.3 respectively.

$$CH_4 + H_2O \rightleftharpoons CO + 3\ H_2 \qquad \text{Equation 1.2}$$

$$CH_4 + 2\ H_2O \rightleftharpoons CO_2 + 4\ H_2 \qquad \text{Equation 1.3}$$

As an endothermic process, steam reforming occurs at a high temperature, which can lead to methane decomposition and therefore carbon deposition. An excess of steam is often used for these reactions to drive the formation of hydrogen, to limit coking and to push the equilibrium of the water-gas shift reaction to the hydrogen formation. This excess of steam does however lead to the evolution of carbon dioxide gas which has a negative impact on the environment.

Dry reforming of methane involves the utilisation of carbon dioxide to reform methane into syn-gas, shown in Equation 1.4. This utilisation of carbon dioxide is extremely favourable as it consumes two greenhouse gases, CO_2 and CH_4, simultaneously. The mixture of methane and carbon dioxide is commonly referred to as biogas as it results from the degradation of organic matter in an oxygen deficient environment. As with steam reforming, dry reforming is an endothermic process and therefore has the same issue with high operating temperatures and carbon deposition. The reverse water-gas shift reaction, Equation 1.5, can occur if the concentration of carbon dioxide in the biogas is too high, which leads to a lesser yield of hydrogen. The Boudouard reaction, Equation 1.6, occurs when there is an excess of carbon monoxide present, which leads to the formation of carbon dioxide and elemental carbon. The carbon then leads to the deactivation of the catalyst.

$$CH_4 + CO_2 \rightleftharpoons 2\ CO + 2\ H_2 \qquad \text{Equation 1.4}$$

$$CO + H_2O \rightleftharpoons H_2 + CO_2 \qquad \text{Equation 1.5}$$

$$2\ CO \rightleftharpoons CO_2 + C \qquad \text{Equation 1.6}$$

The partial oxidation (POx) of methane, Equation 1.7, can also be utilised for hydrogen production, however it requires the correct ratios of reactants to be present, otherwise combustion will occur, also known as total oxidation (TOx), Equation 1.8. A hydrogen rich synthesis gas results from the successful partial oxidation of methane.

$$CH_4 + \tfrac{1}{2}\ O_2 \rightleftharpoons 2\ H_2 + CO \qquad \text{Equation 1.7}$$

$$CH_4 + 2\ O_2 \rightleftharpoons 2\ H_2O + CO_2 \qquad \text{Equation 1.8}$$

Unlike the other methane reforming reactions, POx is exothermic and occurs at lower temperatures, however at these lower temperatures TOx of methane becomes more favourable over the POx.

1.7 Zeolite catalysed methane reforming

Previous work with the use of zeolites as catalysts on the reforming of methane has mainly focussed around dry reforming. Commonly, only an equal ratio of methane to carbon dioxide is used and the reaction is studied at one stable temperature. Works by Frontera *et al*.[60,61] study Silicalite-1, the all silica form of the MFI framework. They determined that the silylation of the support surface leads to a higher percentage conversion of the methane and carbon dioxide which in turn leads to the limiting of coking and catalyst deactivation.

Halliche *et al.*[62] studied the dry reforming of the materials using ZSM-5 (described in Chapter 4), USY and mordenite at various temperatures between 400 °C and 700 °C. They determined that the catalytic performance improved on the increase of the CO_2 to CH_4 ratio above 1.

The study by Izquierdo *et al.*[63] carried out methane reforming testing of Zeolite L, Ni monometallic catalysts and rhodium-nickel bimetallic catalysts. They studied dry reforming, steam reforming, partial oxidation, as well as tri-reforming, which combines all three techniques. They determined that dry reforming is best suited when the aim is to convert all the CO, and that the nanosized, 30-60 nm, Rh-Ni Zeolite-L material is “a promising catalyst”. From the literature it is clear that more investigations into zeolite catalysed reforming is needed[64,65]. Limited work into the partial oxidation and the effect of the zeolite size and type could be mean that a better performing and more efficient catalyst could remain undiscovered.

1.8 Aims and Objectives of the study

The aim of the work presented in this thesis is to further understanding into the synthesis mechanism of the nanosized zeolites and to utilise the knowledge gained to aid in the application of these nanosized zeolites in the reforming of methane. This aim can be broken down into several key objectives:

1. To show that the nanosized MFI type zeolite material can be successfully synthesised using a different structure directing agent than in previous studies.
2. To compare the use of two structure directing agents to gain a further understanding into the mechanism of formation of these nano sized zeolites.
3. To apply these MFI type nano sized zeolites to the catalysis of methane reforming and compare them with their micron sized counterparts.
4. To study the effect of the change in zeolite type on the catalysis of methane reforming, utilising the zeolite types MEL and MTW.

1.9 References

1. Masters AF, Maschmeyer T. Zeolites - From curiosity to cornerstone. Micropor Mesopor Mat. 2011;142(2-3):423–38.
2. Li Y, Yu J. New stories of zeolite structures: their descriptions, determinations, predictions, and evaluations. Chem Rev. 2014;114(14):7268–316.
3. Cundy CS, Cox PA. The hydrothermal synthesis of zeolites: History and development from the earliest days to the present time. Chem Rev. 2003;103:663–701.
4. International Zeolite Association. Database of Zeolite Structures [Internet]. 2015. Available from: http://www.iza-structure.org/databases/
5. Rouquerol F, Rouquerol J, Sing KSW, Llewellyn P, Sing K, Maurin G. Adsorption by Clays, Pillared Clays, Zeolites and Aluminophosphates. In: Adsorption by Powders and Porous Solids. 2nd Edition. France: Academic Press. 2012. p. 467-527.
6. Sassoye C, Loiseau T, Taulelle F, Férey G. A new open-framework fluorinated gallium phosphate with large 18-ring channels (MIL-31). Chem Commun. 2000;(11):943-944.
7. Lutz W. Zeolite Y: Synthesis, Modification, and Properties—A Case Revisited. Adv Mater Sci Eng. 2014; 1-20.
8. Morris R. Modular materials from zeolite-like building blocks. J Mater Chem. 2005;15(9):931-938.
9. Darton RJ. Structural Studies of Zeolites by Solid State NMR and Microcrystal X-ray Diffraction. Thesis submitted to University of St. Andrews. 2004.
10. Barrer R, Hinds L, White E. 299. The hydrothermal chemistry of silicates. Part III. Reactions of analcite and leucite. J Chem Soc. 1953;1466-1475.
11. Barrer R, Marcilly C. Hydrothermal chemistry of silicates. Part XV. Synthesis and nature of some salt-bearing aluminosilicates. J Chem Soc A. 1970; 2735-2745.

12. Barrer R. Synthesis of a zeolitic mineral with chabazite-like sorptive properties. J Chem Soc. 1948; 127-132.
13. Milton RM. ACS Symp Ser., 1989; 398, 1.
14. R. M. Barrer, P. J. Denny and E. M. Flanigen, US Pat. 3306922, 1967.
15. Barrer R, Denny P. 201. Hydrothermal chemistry of the silicates. Part IX. Nitrogenous aluminosilicates. J Chem Soc. 1961;971-982.
16. Dib E, Gimenez A, Mineva T, Alonso B. Preferential orientations of structure directing agents in zeolites. Dalton Trans. 2015;44(38):16680-16683.
17. Brace S, Wormald P, Darton R. The effect of structure directing agents on the ordering of fluoride ions in pure silica MFI zeolites. Phys Chem Chem Phys. 2015;17:11950-11953.
18. Flanigen EM, Patton RL. US Pat. 4073865, 1978.
19. Schoeman B. The homogeneous nature of clear TPA-silicalite-1 precursor solutions. Microporous Mater. 1997;9(5-6):267-271.
20. Fyfe C, Darton R, Schneider C, Scheffler F. Solid-State NMR Investigation of the Possible Existence of “Nanoblocks” in the Clear Solution Synthesis of MFI Materials. Journal Phys Chem C. 2007;112(1):80-88.
21. Tosheva L, Valtchev VP. Nanozeolites: Synthesis, Crystallization Mechanism, and Applications. Chem Mater. 2005;17:2494–2513.
22. Kirschhock CE a, Ravishankar R, Verspeurt F, Grobet PJ, Jacobs PA , Martens JA. Identification of precursor species in the formation of MFI zeolite in the TPAOH-TEOS-H2O system. J Phys Chem B. 1999;103:4965–4971.
23. Kirschhock CE. Mechanism of transformation of precursors into nanoslabs in the early stages of MFI and MEL zeolite formation from TPAOH-TEOS-H_2O and TBAOH-TEOS-H_2O. J Phys Chem B. 1999;103(24):4972-4978.
24. Kirschhock CE, Ravishankar R, Jacobs PA, Martens JA. Aggregation Mechanism of Nanoslabs with Zeolite MFI-Type Structure. J Phys Chem B. 1999;103(50):11021–11027.

25. Kirschhock CEA, Ravishankar R, Verspeurt F, Grobet PJ, Jacobs PA, Martens JA. Reply to the Comment on “Identification of Precursor Species in the Formation of MFI Zeolite in the TPAOH-TEOS-H_2O System.” J Phys Chem B. 2002;106(12):3333–3334.
26. Kirschhock CE, Kremer SPB, Grobet PJ, Jacobs PA, Martens JA, Centrum V, *et al*. New Evidence for Precursor Species in the Formation of MFI Zeolite in the Tetrapropylammonium Hydroxide-Tetraethyl Orthosilicate-Water System. J Phys Chem B. 2002;106(19):1–4.
27. Kirschhock CEA, Buschmann Â, Kremer S, Ravishankar R, Houssin CJY, Mojet BL, *et al*. Zeosil Nanoslabs: Building Blocks in nPr_4N^+-Mediated Synthesis of MFI Zeolite. Angew Chem Int Edit. 2001;40(14):2637–2630.
28. Ravishankar R, Kirschhock CE a., Knops-Gerrits P-P, Feijen EJP, Grobet PJ, Vanoppen P, et al. Characterization of Nanosized Material Extracted from Clear Suspensions for MFI Zeolite Synthesis. J Phys Chem B. 1999 Jun;103(24):4960–4964.
29. Knight CTG, Kinrade SD. Comment on “Identification of Precursor Species in the Formation of MFI Zeolite in the TPAOH -TEOS-H_2O System.” J Phys Chem B. 2002;106(12):3329–3332.
30. Kragten DD, Fedeyko JM, Sawant KR, Rimer JD, Vlachos DG, Lobo RF, *et al*. Structure of the silica phase extracted from silica/(TPA)OH solutions containing nanoparticles. J Phys Chem B. 2003;107:10006–10016.
31. Ramanan H, Kokkoli E, Tsapatsis M. On the TEM and AFM evidence of zeosil nanoslabs present during the synthesis of silicalite-1. Angew Chem Int Edit. 2004;43(35):4558–4561.
32. Fedeyko JM, Rimer JD, Lobo RF, Vlachos DG. Spontaneous formation of silica nanoparticles in basic solutions of small tetraalkylammonium cations. J Phys Chem B. 2004;108:12271–12275.
33. Provis JL, Vlachos DG. Silica Nanoparticle Formation in the TPAOH-TEOS-H_2O System: A Population Balance Model. J Phys Chem. 2006;110(7):3098–3108.

34. Cheng C-H, Shantz DF. ^{29}Si NMR studies of zeolite precursor solutions. J Phys Chem B. 2006;110(1):313–318.
35. Rimer JD, Vlachos DG, Lobo RF. Evolution of Self-Assembled Silica-Tetrapropylammonium Nanoparticles at Elevated Temperatures. J Phys Chem. 2005;109:12762–12771.
36. Rimer JD, Lobo RF, Vlachos DG. Physical Basis for the Formation and Stability of Silica Nanoparticles in Basic Solutions of Monovalent Cations. J Phys Chem. 2005;21(16):8960–8971.
37. Fedeyko JM, Vlachos DG, Lobo RF. Formation and Structure of Self-Assembled Silica Nanoparticles in Basic Solutions of Organic and Inorganic Cations. Langmuir. 2005;21(11):5197–5106.
38. Villaescusa LA, Barrett PA, Camblor MA. Synthesis and structure of ITQ-9: a new microporous SiO2 polymorph. Chem Commun. 1998;21:2329-2330.
39. Villaescusa L, Wheatley P, Bull I, Lightfoot P, Morris R. The Location and Ordering of Fluoride Ions in Pure Silica Zeolites with Framework Types IFR and STF; Implications for the Mechanism of Zeolite Synthesis in Fluoride Media. J Am Chem Soc. 2001;123(36):8797-8805.
40. Fyfe CA. Solid-state NMR comes of age. Nature. 1987;325(6101):194-194.
41. Fyfe CA, Kennedy GJ, De Schutter CT, Kokotailo GT. Sorbate-induced Structural Changes in ZSM-5 (Silicalite). J Chem Soc, Chem Commun. 1984;8:541-542
42. Fyfe CA, Strobl H, Kokotailo GT, Kennedy GJ, Barlow GE. Ultra-High-Resolution ^{29}Si Solid-State MAS NMR Investigation of Sorbate and Termperature-Induced Changes in the Lattice Structure of Zeolite ZSM-5. J Am Chem Soc. 1999;110:3373-3380.
43. Li Y, Chung T-S. Exploratory Development of Dual-Layer Carbon–Zeolite Nanocomposite Hollow Fiber Membranes with High Performance for Oxygen Enrichment and Natural Gas Separation. Micropor Mesopor Mater. 2008;113(1-3)315-324.

44. Shevade S, Ford RG. Use of Synthetic Zeolites for Arsenate Removal from Pollutant Water. Water Res. 2004;38(14-15)3197-3204.
45. Kalló D. Applications of Natural Zeolites in Water and Wastewater Treatment. Rev Mineral Geochem. 2001;45(1):519-550.
46. Applebaum SB, Behrman AS. Applications of Carbonaceous Zeolites to Water Softening [with Discussion]. J Am Water Works Ass. 1938;30(6):947-978
47. Primo A, Garcia H. Zeolites as catalysts in oil refining. Chem Soc Rev. 2014;43(22):7548-7561.
48. Exxon Mobil Oil Corp. US Pat. 3702886A. 1972
49. Xu B, Sievers C, Hong SB, Prins R, van Bokhoven JA. J Catal. 2006;244(2):163-168.
50. Baxter RJ, Hu P. Insight into why the Langmuir–Hinshelwood mechanism is generally preferred. Journal Chem Phys. 2002;116(11):4379-4381.
51. Weinberg W. Eley−Rideal Surface Chemistry: Direct Reactivity of Gas Phase Atomic Hydrogen with Adsorbed Species. Acc Chem Res. 1996;29(10):479-487.
52. Harris J, Kasemo B. On Precursor Mechanisms for Surface Reactions. Surf Sci Lett. 1981;105(2-3):L281-L287.
53. Guisnet M, Ribeiro FR. Deactivation and Regeneration of Zeolite Catalysts. Portugal:World Scientific; 2011.
54. Teixeira ACSC, Giudici R. Deactivation of Steam Reforming Catalysts by Sintering: Experiments and Simulation. Chem Eng Sci. 1999;51(16-16):3609-3618.
55. Struis RPWJ , Schildhauer TJ, Czekaj I, Janousch M, Biollaz SMA, Ludwig C. Sulphur poisoning of Ni catalysts in the SNG production from biomass:A TPO/XPS/XAS study. Appl Catal A-Gen. 2009;362(1-2):121-128.
56. Wojcik A, Middleton H, Damopoulos I, Van herle J. Ammonia as a Fuel in Solid Oxide Fuel Cells. J Power Sources. 2003;118(1-2):342-348.
57. Trimm DL. Catalysts for the Control of Coking During Steam Reforming. Catal Today. 199;49(1-3):3-10.

58. Zhang J, Wang H, Dalai AK. Development of Stable Bimetallic Catalysts for Carbon Dioxide Reforming of Methane. J. Catal. 2007;249(2);300-310.
59. Enger BC, Lodeng R, Holmen A. A Review of Catalytic Partial Oxidation of Methane to Synthesis Gas with Emphasis on Reaction Mechanisms over Transition Metal Catalysts. Appl Catal A-Gen. 2008;346(1-2):1-27.
60. Frontera P, Macario A, Aloise A, Crea F, Antonucci P, Nagy J *et al*. Catalytic Dry-Reforming on Ni–Zeolite Supported Catalyst. Catal Today. 2012;179(1):52-60.
61. Frontera P, Macario A, Aloise A, Antonucci P, Giordano G, Nagy J. Effect of Support Surface on Methane Dry-Reforming Catalyst Preparation. Catal Today. 2013;218-219:18-29.
62. Halliche D, Cherifi O, Taarit Y, Auroux A. Catalytic Reforming of Methane by Carbon Dioxide over Nickel-Exchanged Zeolite Catalysts. Kinet Catal. 2008;49(5):667-675.
63. Izquierdo U, Barrio V, Bizkarra K, Gutierrez A, Arraibi J, Gartzia L *et al*. Ni and Rh-Ni Catalysts Supported on Zeolites L for Hydrogen and Syngas Production by Biogas Reforming Processes. Chem Eng J. 2014;238:178-188.
64. De Jesus A, Maloncy M, Batista M. Effect of MgO Loading over Zeolite-Supported Ni Catalysts in Methane Reforming with Carbon Dioxide for Synthesis Gas Production. React Kinet Mech Cat. 2017;122(1):501-511.
65. Bawah A, Malaibari Z, Muraza O. Syngas production from CO_2 Reforming of Methane over Ni Supported on Hierarchical Silicalite-1 Fabricated by Microwave-Assisted Hydrothermal Synthesis. Int J Hydrogen Energ. 2018;43(29):13177-13189.

2.0 Synthesis of high-silica zeolites

2.1 Synthesis of all-silica MFI

2.1.1 Introduction

The MFI framework is one of the most commonly studied zeolite framework types. It has been shown that a variety of different structure directing agents (SDAs) are able to direct its formation[1,2] and is able to be formed via a number of different synthesis methods[1,2,3]. Previous work by Fyfe *et al*. 2008[3], has shown that the tetrapropylammonium (TPA) salt can be used to form the nano-sized MFI zeolite under clear solution reaction conditions. As previously mentioned in Chapter 1.2, the mechanism of formation of the MFI framework is under considerable debate. The use of a different SDA could provide new insight into this mechanism. Brace *et al*.[2] showed that a methyl tributylammonium (MTBA) salt can successfully yield the MFI framework, this template was therefore chosen alongside the TPA salt to use as a comparison.

1.

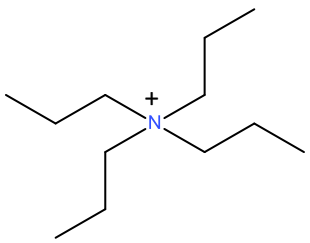

2.

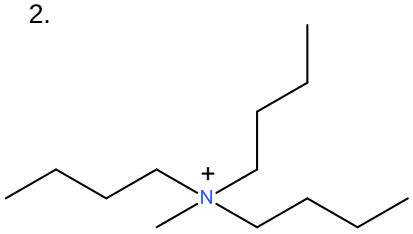

Figure 2.1 The structures of MFI SDA cations 1. TPA 2. MTBA

In this work the aim was to utilise the clear solution method to synthesise the nano-sized MFI framework with using two different SDAs, during which samples were to be taken at specific times during the reaction to allow the characterisation of each reaction over time.

2.1.2 Structure directing agents for MFI synthesis

As tetraethylorthosilicate (TEOS) is used for clear solution syntheses it was necessary to have the SDAs in their hydroxide forms to allow the hydrolysis of the tetraethyl orthosilicate

(TEOS). The two quaternary ammonium cations chosen are both commercially available so it was not necessary to synthesis either, however only TPA was available to purchase in its hydroxide form. MTBA Cl was ion-exchanged using Ambersep 900 OH resin to form MTBA OH, yielding a final concentration of 0.98 M.

2.1.3 Hydrothermal synthesis of the F-MFI framework

For comparative reasons, a high-resolution sample of the MFI framework was needed. As fluorinated zeolites give the most resolved peaks for X-ray diffraction it was decided an F-MFI framework would be synthesised.

MTBA Cl (3.18 M ,4.05 g), NH_4F (0.63 g) and deionised H_2O (2.10 g) was placed in a teflon-liner. Fumed silica (1.0 g) was then added and mixed until homogenous. This liner was then sealed and placed in an autoclave at 180 °C for 6 days, after which the resulting solid was collected via centrifugation and dried in a 60 °C oven.

The resulting X-ray diffraction pattern showed well resolved peaks indicative of the MFI framework.

2.1.4 Clear solution synthesis of nano-sized MFI zeolites

This method was adapted from Fyfe *et al.* 2008[3]. The clear solution syntheses containing TPA and MTBA were carried out simultaneously, which allows for any external factors, such a laboratory temperature, to be nullified when the reactions are compared. Table 2.1 shows the quantities of reagents used in each. For each reaction, the SDA and the deionised water were weighed directly into a 50 mL round bottomed flask. The TEOS was then added dropwise, whilst stirring, to avoid the reaction mixture gelling. Once combined the solution was left to stir at room temperature for 24 hours before being equipped with a reflux condenser and heated to 95 °C for 2 weeks. Even though the reaction was not fully at reflux, a condenser was required to limit the loss of water from the reaction mixture.

Table 2.1. Quantities of each reagent for the clear-solution syntheses.

Reagent	Quantity used for the TPA reaction	Quantity used for the MTBA reaction
TPA OH (1.0 M in water)	13.98 g	-
MTBA OH (0.98 M in water)	-	13.91 g
Deionised H_2O	10.52 g	10.47 g
TEOS (reagent grade solution)	7.56 g	7.53 g

For both syntheses, timepointed samples of the reaction mixture were taken to allow the reaction to be characterised over time. These samples, 1 mL each, were pipetted straight from the reaction vessel, placed in a microfuge tube and placed in freezer to stop the reaction progressing any further. In total, 24 samples were taken for the reactions. They are referred to in relation to their time, in hours, when they were sampled from the reaction mixture. The 0 hour samples indicate samples that were taken before heating but after the 24 hour long room temperature stir. The timepointed samples are listed below:

0, 24, 30, 45, 52, 67, 75, 91, 100, 115, 123, 139, 148, 163, 172, 187, 195, 215, 240, 260, 284, 309, 315, 336 (hours).

After all samples were collected, they were allowed to thaw and any solid that had formed was collected via centrifugation, 16000 rpm for 15 minutes. The resulting solid was then oven dried at 60 °C and then characterised using a variety of different techniques, described in Chapter 3.

2.1.5 Synthesis of MFI-type zeolite catalysts

To allow catalytic testing to be carried out on these materials, as with many catalysts, they were first required to be ‘doped’ with a catalytically active metal. In this case nickel was

chosen due to its well established activity for catalysis[4] but also for its cost in relation to other active metals such as platinum and palladium.

The aim of these syntheses was to form a Ni containing material in the micrometer and nanometer size range to allow for a comparison of catalytic activity versus particle size. As mentioned in Chapter 1, it was postulated that the smaller particle size would minimise diffusion limitations within the material and therefore increase the efficiency of catalysis.

The nano-sized sodium containing material was synthesised using the clear-solution method using the same ratios of reagents as with the timepointed synthesis (Chapter 2.2.4), however also incorporating sodium chloride (0.21 g), which was dissolved in the deionised water before being added. The reaction was heated to 95 °C for 2 weeks.

The micron-sized sodium containing material was synthesised using the hydrothermal method used for the F-MFI framework. As the silicon source was fumed silica, the SDA was not required to be in the hydroxide form. MTBA Cl (3.18 M, 0.785 mL), NaOH (9.13 mL, 1 M) and deionised H_2O (35.1 g) was mixed together in a teflon-lined stainless steel autoclave. Once mixed, fumed silica (5.0 g) was added slowly and stirred until a homogeneous reaction mixture was yielded. The autoclave was then sealed and heated at 150 °C for 4 days.

Once both reactions had gone to completion, the resulting white solids were collected via centrifugation and oven dried at 60 °C. The yielded sodium containing samples were then characterised via X-ray diffraction to ensure the MFI framework had been formed.

As catalysis requires the channels of the zeolite framework to be empty, the structure directing agents occluded in the channels had to be removed. The samples were calcined under a flow of oxygen for 3 hours at 450 °C.

Once cool approximately 1.0 g of the calcined material was placed in a $Ni(NO_3)_2$ solution (0.05 M, 100 mL) and stirred for 3 hours. This was repeated three times, each time with a ‘fresh’ quantity of nickel nitrate to ensure the maximum amount of ion exchanged between the material and the solution. In this step, the sodium was exchanged for nickel in the solution. The replacement of the nickel solution allowed the equilibrium formed between the materials to be ‘reset’ and allowed more nickel to be ‘doped’ into the zeolite samples. The

samples were recovered via centrifugation, washed with deionised water to remove excess nickel on the zeolite surface and dried in a 60 °C oven.

These nickel containing samples were then tested for their methane reforming capabilities as described in Chapter 3.4.

2.1.6 Conclusions

Two structure directing agents were utilised to yield 24 timepointed samples of a nano-sized MFI zeolite reaction. These samples were then characterised as described in Chapter 3, to allow further insight into the mechanism of formation of the zeolite framework.

A fluorine containing MFI framework has been synthesised to give a standard sample for comparison.

Two nickel containing all silica MFI-type zeolites have been synthesised, via an intermediate sodium containing zeolite. The sodium containing material will act as a control sample for the catalytic testing described in Chapter 3. The Ni containing materials were tested for their methane reforming capabilities as described in Chapter 3.

2.2 Synthesis of high-silica MEL

2.2.1 Introduction

As the MFI and MEL frameworks commonly occur as intergrowths a logical comparison for MFI zeolite catalytic activity is the MEL type zeolite. The synthesis method used, adapted from the 1984 patent by Valyocsik[5], incorporates a small amount of aluminium into the framework and utilises commercially available 1,8-diaminooctane as the SDA. The MEL nickel containing catalyst is formed via a potassium containing intermediate, as opposed to the sodium containing intermediate used in the MFI catalyst synthesis.

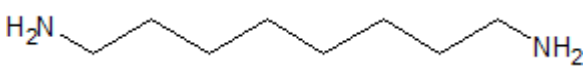

Figure 2.2 The structure of the MEL template 1,8-diamino octane.

2.2.2 Synthesis of an MEL-type zeolite catalyst

As with the micron-sized MFI zeolite mentioned previously, the hydrothermal method was used to in the synthesis of the MEL-type catalyst.

$Al(OH)_3$ (0.3 g) in deionised water (3 mL), KOH (0.675 g) in deionised water (3 mL), 1,8-diaminooctane (1.74 g) in deionised water (4.5 mL) and a 40 % Silica solution (6 mL) in deionised water (4.5 mL) was mixed until homogenous in a teflon-lined stainless steel autoclave. Once stirred, the autoclave was sealed and placed in a 160 °C oven for 14 days. After which the resulting precipitate was collected via centrifugation and dried in a 60 °C oven. The resulting XRD pattern confirmed the successful formation of the MEL framework. As with the MFI catalysts, the SDA was removed from the channels of framework via calcination under a flow of oxygen at 450 °C for 4 hours. Once cooled, the potassium within the framework was ion-exchanged for nickel using $Ni(NO_3)_2$, as in section 2.1.5.

2.2.3 Conclusion

A nickel containing MEL zeolite catalyst was synthesised. Unlike the MFI catalyst synthesised in the previous section, the MEL catalyst was formed via a potassium containing intermediate. This Ni ‘doped’ material was tested for its methane reforming capabilities as described in Chapter 3.

2.3 Synthesis of high-silica MTW

2.3.1 Introduction

The MTW framework type was chosen as it is also a ‘five-rings’ zeolite like the MFI and MEL types previously. The synthesis method chosen was adapted from the Larlus *et al*[6] paper, describing a synthesis for zeolite beta (type code BEA) which resulted in the reliable formation of MTW, utilising the hydrothermal method to yield an all-silica framework. In the same manner as the MFI catalysts, the MTW counterpart was synthesised via a sodium containing intermediate. Prior to the zeolite synthesis, the structure directing agent 4,4’-

trimethylenebis (N-methyl, N-benzyl piperidinium) hydroxide, hereby referred to as $TMP(OH)_2$, was synthesised.

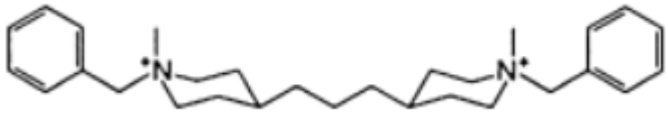

Figure 2.3 The structure of the MTW SDA TMP cation (Taken from Hould *et al.*[7]).

2.3.2 Synthesis of $TMP(OH)_2$

The preparation for $TMP(OH)_2$ was taken from Larlus et al. 2011[5], and proceeds via first synthesising $TMPBr_2$. 4,4'-trimethylenebis (1-methylpiperidine) (12.02 g) in acetone (50 mL) was placed in a round bottom flask and cooled in ice before being mixed with ice cooled benzyl bromide (17.10 g) in acetone (100 mL). The reaction, equipped with a reflux condenser, was heated overnight at 50 (°C). The resulting solid was recrystallised in acetone and ethanol with a small amount of diethyl ether to recover the product. This $TMPBr_2$ was then dissolved in deionised water (100 mL) and treated with Ambersep 900 OH resin to yield the final product $TMP(OH)_2$ with a concentration of 0.59 M in respect to the hydroxide ions.

2.3.3 Synthesis of an MTW-type zeolite catalyst

The synthesis of the nickel containing MTW-type catalyst was taken from the Larlus *et al.*[5] paper, achieved through the use of the hydrothermal method, as with the MFI and MEL catalysts.

$TMP(OH)_2$ (1.816 g, 0.59 M) NaCl (0.016 g) and deionised water (7.5 g) were placed in a teflon-lined stainless steel autoclave. Fumed silica (1.0 g) was then stirred into the solution until homogenous, after which the autoclave was sealed and placed in a 150 °C oven for 14 days. The resulting white precipitate was collected via centrifugation and dried in a 60 °C oven.

The sample was then calcined to remove the SDA from within the framework channels. This was again achieved by heating the sample under a flow of oxygen. Unlike the catalysts mentioned in the Chapter, the MTW catalyst required a higher temperature to fully removed the SDA. This was determined via a colour change of the sample from white to orange after the initial calcination at 450 °C, indicating that the SDA had burnt but not fully driven out of the sample. The remaining SDA removed after subsequent heating to 650 °C for 3 hours. Once cooled the sodium in the framework was ion-exchanged out for nickel, using $Ni(NO_3)_2$, was described in section 2.1.5.

2.3.4 Conclusion

A nickel containing MTW zeolite catalyst was synthesised via a sodium containing intermediate. This Ni 'doped' material was tested for its methane reforming capabilities as described in Chapter 3.4.

2.4 Conclusions

Four different structure directing agents have been utilised to yield three different zeolite types.

Two timepointed nano-sized MFI reactions were carried out for comparative reasons and to give further insight into the mechanism of formation of the MFI framework. An F-MFI framework has also been synthesised to allow for a comparison for the timepointed samples.

Four nickel containing zeolite catalysts have been synthesised to allow for testing of their methane reforming capabilities, described in Chapter 3.4. These catalysts were made via either a sodium or potassium containing intermediate. After calcination, this sodium or potassium was then ion-exchanged out to yield the final nickel containing materials.

2.5 References

1. Dib E, Gimenez A, Mineva T, Alonso B. Preferential Orientations of Structure Directing Agents in Zeolites. Dalton T. 2015;44(38):16680-16683.

2. Brace S, Wormald P, Darton R. The effect of structure directing agents on the ordering of fluoride ions in pure silica MFI zeolites. Phys Chem Chem Phys. 2015;17:11950-11953.

3. Fyfe C, Darton R, Schneider C, Scheffler F. Solid-State NMR Investigation of the Possible Existence of “Nanoblocks” in the Clear Solution Synthesis of MFI Materials. Journal Phys Chem C. 2007;112(1):80-88

4. Evans SE, Good OJ, Staniforth JZ, Ormerod RM, DartonRJ. Overcoming Carbon Deactivation in Biogas Reforming using a Hydrothermally Synthesised Nickel Perovskite Catalyst. RSC Adv. 2014;4(58):30816-30819.

5. Valyocsik, EW. US Pat. 4902406A. 1984.

6. Larlus O, Mintova S, Wilson S, Willis R, Abrevaya H, Bein T. A Powerful Structure-Directing Agent for the Synthesis of Nanosized Al- and High-Silica Zeolite Beta in Alkaline Medium. Micropor Mesopor Mater. 2011;142(1):17-25.

7. Hould N, Haouas M, Nikolakis V, Taulelle F, Lobo R. Mechanisms of Quick Zeolite Beta Crystallization. Chem Mater. 2012;24(18):3621-3632.

3.0 Methodology

3.1 X-Ray Diffraction (XRD)

3.1.1 X-ray diffractometer

X-ray diffraction patterns were obtained using a Bruker D8 Advance X-ray Diffractometer, containing a CuKα radiation source with a wavelength of 1.5418 Å at 40 KV and 40 mA tube voltage and current respectively. Diffraction patterns for the zeolite samples were collected using two different 'stages'.

The Bruker 'flipstick' flat plate sample changer stage allows the user to queue up to nine samples at a time. Ground samples were placed in a sample holder, with a 1 cm depth and 2.5 cm diameter, and compacted using a glass slide to yield a smooth surface. The 2-theta scan range was 5-60°, with a step size of 0.07° and a dwell of 4 seconds.

The capillary stage only allows only one sample at a time, which does not allow for queueing of samples. This stage was used to yield diffraction patterns at lower angle, for sample in lower quantity, and timepointed samples still in solution. The samples were placed in 1.0 mm diameter capillaries which were then sealed with molten wax. The samples were analysed in the 2θ range of 0.5° to 25°, with 0.4 mm slits and a step size of 0.03°.

3.1.2 X-ray diffraction theory

X-ray diffraction utilises the unique crystal structure of individual materials to allow their structural characterisation. The crystal structure of a material is most easily described in relation to the simplest three-dimensional repeating unit, known as the unit cell. These unit cells are defined by their lattice parameters i.e. the length of the three edges *a*,*b*,*c* and the size of the three angles α, β, γ. Each unit cell can be grouped into one of seven crystal systems, shown in table 3.1. Within each unit cell are lattice points, where it is likely to find an atom. It is from the electron cloud of these atoms that X-rays are scattered.

Table 3.1. Crystal Systems and their associated lattice parameters.

Crystal System	Edges	Angles
Cubic	a = b = c	α = β = γ = 90°
Tetragonal	a = b ≠ c	α = β = γ = 90°
Orthorhombic	a ≠ b ≠ c	α = β = γ = 90°
Monoclinic	a ≠ b ≠ c	α = γ = 90° β ≠ 90°
Rhombohedral	a = b = c	α = β = γ ≠ 90°
Hexagonal	a = b ≠c	α = β = 90° γ = 120°
Triclinic	a ≠ b ≠ c	α ≠ β ≠ γ

The X-ray beam used for diffraction is collimated and of a single wavelength, produced from the bombardment of a Cu target by high energy electrons and the use of a crystal monochromater. These X-rays are then directed to the sample, where some will pass straight through, whilst others will be scattered from electrons within the material. When a beam is reflected from a plane, the angle of incidence and reflectance are the same. If another beam is also reflected but this time from an adjacent plane, the resulting scattered X-ray will interact with its counterpart from the nearby plane. This interaction is either constructive or destructive interference, depending on the relative phase of each beam. This is known as Bragg's theory[1].

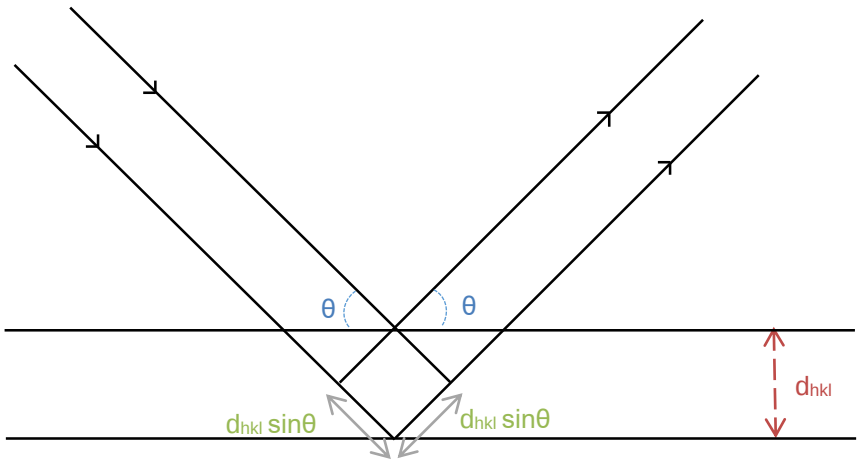

Figure 3.1. Bragg diffraction from a set of planes with a spacing of d_{hkl}.

In the case of constructive interference, the extra distance travelled by one of the scattered X-rays is a whole number of wavelengths. Bragg theory shows that this extra distance travelled, nλ, is related to the lattice spacing, d_{hkl}, and the angle of incidence, θ, by the following equation:

$$n\lambda = 2d_{hkl}\sin\theta \qquad \text{Equation 3.1.}$$

The letters h, k and l refer to the Miller indices assigned to a specific plane cutting the unit cell. Each letter is given a number to quantify the intercept of the plane with the three edges of the unit cell. For each plane, there will be a diffraction maximum where the constructive interference will be at its maximum. The Bragg equation allows the spacing between the planes to be calculated. For simple cubic systems, when combined with Equation 3.2 the Miller indices, hkl, can be assigned for each diffraction maxima, known as indexing. The lengths of the edges in Equation 3.2 are denoted a_0, as in a cubic system all edges are of equal length.

$$d_{hkl} = a_0 / (\sqrt{h^2 + k^2 + l^2}) \qquad \text{Equation 3.2.}$$

Miller indices are the reciprocals of the fractional intercepts the plane makes within the unit cell according to each length abc, i.e. notation to indicate the direction a plane cuts the unit cells.

3.2 Dynamic Light Scattering (DLS)

3.2.1 Methodology

The particle sizes of the timepointed nano- and micron- sized all-silica MFI samples were measured using a Malvern Instruments Zetasizer Nano ZS, capable of detecting particles in the size range 0.3 nm to 10 µm. A representative spread of the timepointed samples were chosen for particle sizing to limit analysis time, these were; 30, 52, 91, 123, 163, 195, 284 and 336 hours. Prior to any measurements, all samples were filtered using a 0.5 µm syringe filter to remove any large contaminants, such as dust particles, aggregates or bacteria.

Once filtered the samples were placed into plastic cuvettes, with a path length of 1 cm, and topped up with deionised water to yield a translucent suspension of particles.

The length of each measurement is automatically determined by the Zetasizer from the count rate detected, with each measurement divided into a series of 10 second sub-runs. A typical sample will have 11 to 15 sub-runs.

3.2.2 Dynamic Light Scattering theory

Dynamic light scattering (DLS) is commonly used to determine the particle size of samples down to the nano-scale. It is a non-invasive technique for samples in suspension and as such allowed samples to be analysed and then used for further work.

The light used for scattering is a laser, in this instance a He-Ne laser with a wavelength of 633 nm. The scattering occurs as a result of its interaction with the electron cloud of a particle. The incident photon, initiates an oscillating dipole in this electron cloud which then results in energy being radiated in all directions, this energy is known as scattered light[2].

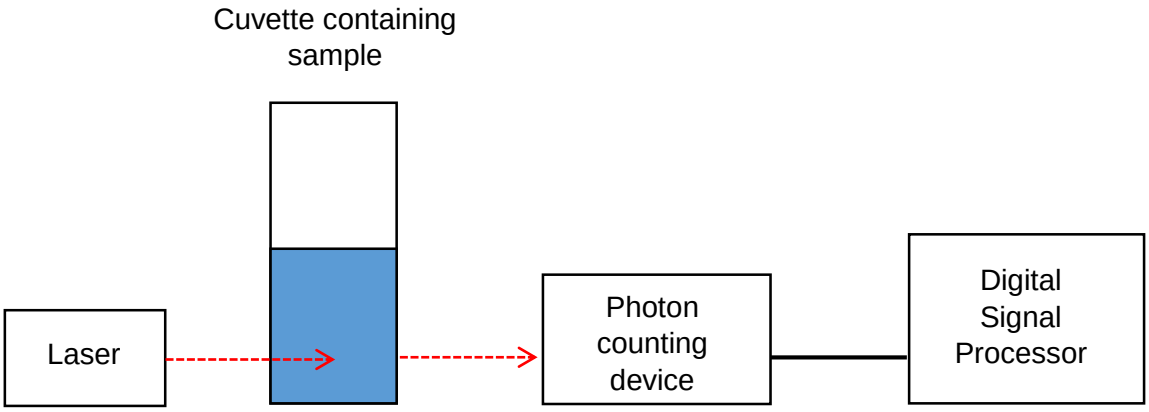

Figure. 3.2 Schematic of the Zetasizer used for dynamic light scattering measurements.

As shown in Figure 3.2, the monochromatic light emitted from the laser is directed towards the sample contained in a plastic cuvette, with a path length of 1 cm. The resulting scattered light is then detected via a photon counting device from which the digital signal is then processed to yield the logarithmically scaled size versus intensity distributions.

There are many different properties of a particle that a particle sizer can measure, shown in Figure 3.3. These are then reported as an equivalent spherical diameter; these different techniques commonly give different sizes for the same sample[2].

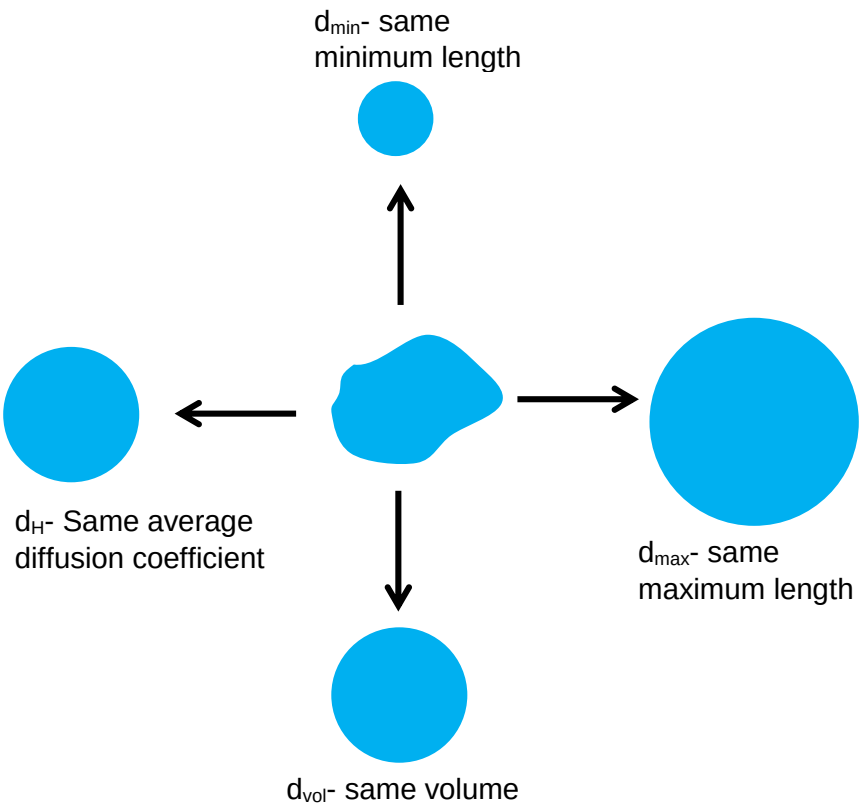

Figure. 3.3 A representation of the different particle properties that can be measured to yield different equivalent spheres, d_{min}, d_{max}, d_{vol} and d_H.

DLS measures the rate of movement of particles undergoing Brownian motion, which describes the random movement of particles in solution due to collisions with other particles, whether, that be with an equivalent or the solvent[3]. The random movements are influenced by the size of the particle, the temperature and the viscosity of the sample. The larger the particle the slower the particle undergoes Brownian motion. The temperature must be accurately known as convection currents within the sample can cause non-random movements.

The velocity of this Brownian motion can be utilised to yield the particle size via the use of the Stokes-Einstein equation, show below. The Stokes-Einstein equation yields the

hydrodynamic diameter (d_H), shown in Figure 3.3, which is the equivalent sphere diameter of a particle that has the same diffusion rate as the particle being measured.

$$D_H = kT / 3\pi\eta D \qquad \text{Equation 3.3.}$$

where d_H is the hydrodynamic diameter, k is the Boltzmann constant, T is the temperature, η is the viscosity, and D is the diffusion coefficient.

The diffusion coefficient (D) is determined from a correlation function. In DLS, correlation is used to determine the time dependence of a signal from within the noise, i.e. it tracks the intensity of a signal over time in relation to the noise. The intercept and baseline at infinity from the correlation function can then be used in conjunction with an exponential expression to give the diffusion coefficient (D) at various times. These can then be fitted with an algorithm to yield the average diffusion coefficient of the sample as a whole.

The value for D can then be used in the Stokes-Einstein equation to yield the mean particle size, z-average diameter (Z_D). As this value is dependent upon the intensity of the scattering it is sensitive to larger sized contaminants such as aggregates or dust. To reduce the likelihood of analyses being affected by the presence of these large contaminants, samples should be filtered prior to any analysis. The analysis is also divided up into a set of 10 second sub-runs to allow the effects of any contaminants to be minimised during testing.

3.3 Solid State Nuclear Magnetic Resonance (SSNMR)

3.3.1 Methodology

All solid state NMR spectra were obtained using a Bruker Avance III HD 400 MHz spectrometer operating at 100.59 MHz for ^{13}C, 400.13 MHz for ^{1}H and 79.47 MHz for ^{29}Si using 2.5 mm rotors and a spinning rate of 6 kHz. The probe used was a 2.5 mm H/X/Y triple resonance CP-MAS probe capable of spinning samples at rate up to 35 kHz. ^{13}C chemical shifts were referenced to tetramethylsilane (TMS) using adamantane as an

external secondary standard. ^{29}Si chemical shifts were referenced TMS using Q_8M_8 as an external secondary standard. Samples were packed into 2.5 mm zirconia rotors with Teflon end caps.

For the ^{13}C {^{1}H} experiments, the CP pulse program was used with a sweep width of 171.393 ppm, an acquisition time of 0.1 seconds, a dwell time of 29 μs and a recycle delay of 3 seconds. The number of scans was 4096 with 0 dummy scans.

For the ^{29}Si {^{1}H} experiments, the CP pulse program was used with a sweep width of 164.995 ppm, an acquisition time of 0.1 seconds, a dwell time of 38 μs and a recycle delay of 3 seconds. The number of scans was 16384 with 0 dummy scans.

3.3.2 NMR Theory

Nuclear magnetic resonance (NMR) spectroscopy is one of the most used and powerful tools used to characterise materials. This is due to its ability to probe the local environment of each atom within a molecule. From a basic point of view NMR probes energy level transitions for atomic nuclei within a magnetic field. NMR analysis can be carried out on samples in both the solution and solid state, however the latter is more complex and time intensive. Solution state NMR is an easily accessible technique for users of varying knowledge due its ability to be performed via automation and the relatively short time in which spectra can be obtained. Solid state NMR on the other hand cannot be performed via automation and therefore requires the user to have a greater knowledge of the system to be able to obtain meaningful results.

Many materials, such as minerals, cannot be studied through solution state NMR due to their insolubility. These materials are commonly studied via X-ray diffraction, however, that technique does not provide the same detail into the structure of the material as solid state NMR does, due to its study of the local environment of nuclei rather than just the material in general.

Nuclear magnetic resonance is able to probe each nuclei as each has an inherent angular momentum known as spin. Each nucleus is assigned a spin quantum number denoted by the letter I. The spin quantum number is determined from the number of unpaired protons and neutrons, where protons, neutrons and electrons all have spins of ½. If the spins all pair up then I will equal zero, if they do not all pair then I for that nuclei will be non-zero, as shown in table 3.2.

Table 3.2. Nuclear spin quantum numbers (I) of commonly occurring nuclides.

Spin Quantum Number (I)	Nuclide
0	^{12}C, ^{16}O
1/2	^{1}H, ^{13}C, ^{15}N, ^{19}F, ^{29}Si, ^{31}P
1	^{2}H, ^{14}N
3/2	^{11}B, ^{23}Na, ^{35}Cl, ^{37}Cl
5/2	^{17}O, ^{27}Al
3	^{10}B

It is important to note that isotopes of the same element can have a different spin quantum number and that some isotopes, such as 12C and 16O, have a spin equal to zero which means it does not have a magnetic moment and is therefore ‘NMR inactive’.

When placed in a magnetic field, each nuclear spin system will interact with that field, this interaction is known as the Zeeman interaction[4]. This interaction is dependent on the orientation of the spin system to the magnetic field, B_0. This orientation dependence leads to a great difference in how solution and solid state NMR are conducted, see below. The Zeeman interaction exists for all nuclei that have a spin, I, and a nuclear magnetic moment, μ. The interaction leads to the formation of 2I+1 energy levels, where I is the spin nuclear quantum number, therefore for a spin-½ nucleus the number of energy levels created by the splitting is 2 and for a spin-1 nucleus 3 energy levels are present. The difference in energy between two energy levels is described in Equation 3.4.

$$\Delta E_z = h\gamma B_0 / 2\pi \qquad \text{Equation 3.4.}$$

where h is Planck's constant, γ is the magnetogyric ratio and B_0 is magnitude of magnetic field.

The population of these two energy levels is described by a Boltzmann distribution[4] shown in Equation 3.5.

$$N_\alpha / N_\beta = \exp(-\Delta E_z / kT) \qquad \text{Equation 3.5.}$$

Where N_α and N_β are the lower and upper energy levels respectively, k is the Boltzmann constant and T is temperature.

The spin systems also have other interactions dependent on the orientation of the spin, such as chemical (magnetic) shielding, dipolar coupling, quadrupolar coupling and spin-spin coupling (also known as J-coupling), however it should be noted that these interactions are small in comparison to the Zeeman interaction. These smaller interactions do however allow insight into the arrangement of atoms within a molecule.

The resonant frequency of a nucleus depends on the gyromagnetic ratio and the strength of the magnetic field it sits in. Due to this, different field strengths will give different resonant frequencies e.g. in a 9.4 T field protons resonate at 400 MHz but in a 23.5 T field they resonate at 1000 MHz. However, the local environment within the molecule also has an effect. The chemical shielding present within the molecule leads to the effective field strength, B_{eff}, on the nucleus being different to that of the magnetic field, B_0. This difference in the effective field strength gives rise to the chemical shift which allows the user to gain insight into the local structure of the molecule.

The strong and stable magnetic field is provided by a superconducting coil of wire with a persistent current running through to generate a magnetic field. This superconducting wire is cooled in liquid helium which removes resistance and allows the current to persist without any need for further electrical power. To ensure the magnetic field is homogenous for

experimentation a set of shim coils are present which each give a different smaller spatial magnetic field which can be adjusted until the field is as required. The probe is fitted at the bottom of the bore hole and the small coil within it is responsible for the excitation and detection of the magnetisation. It does so by pulsing high power monochromatic radiofrequency radiation at the sample and then immediately switching to detection, to avoid any of the high-power pulse energy being picked up by the receiver. The signal detected by the probe is very small therefore it is amplified, through the pre-amp and then into the console, to a high enough level before being digitised.

Solid state NMR requires a different approach to yield meaningful spectra. As the Zeeman interaction depends on the angle between the nuclear spin and the spectrometer magnetic field, and in the solid state molecules are in a fixed position, a range of resonant frequencies are expected to be seen, thus yielding a broad line. Line broadening is also a result of chemical shielding, dipolar interaction between nuclear spins and quadrupolar interactions. In the solution state the rapid tumbling of species leads to the line broadening interactions being averaged to zero. In the solid state this averaging does not happen which causes lines to be up to thousands of hertz wide, however, this line broadening can be reduced and/or removed by a technique known as magic angle spinning (MAS). The ‘magic angle’ is 54.74°, in relation to the magnetic field (B_0), as shown in Figure 3.4.

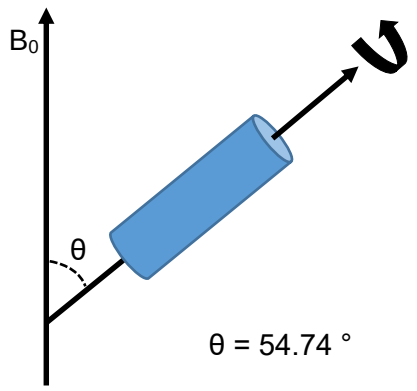

Figure. 3.4. Magic angle spinning.

This number results from the fact that the line broadening interactions, such as chemical shift anisotropy and dipolar interactions, depend on the geometric factor $3\cos^2\theta-1$. For these interactions to be successfully removed the rate at which the sample is spun must be greater than the effect of the interaction.

Heteronuclear dipolar couplings are removed in SSNMR through the use of high power decoupling, this technique is most commonly used to remove coupling between proton spins and the observed nucleus. High powers are required for decoupling in the solid state when compared with its solution counterpart, as the dipolar couplings observed in the solid state are much larger than the smaller scalar couplings in solution. These high powers required however can be utilised to aid the sensitivity of the experiment through the use of cross polarisation (CP). In these experiments polarisation from an abundant, high γ nucleus is transferred to a dilute spin using the dipolar couplings.

Magic angle spinning and cross polarisation are frequently used together to yield a high intensity and well resolved spectrum, particularly for as-synthesised high-silica zeolites.

3.4 Catalyst Testing

3.4.1 Catalytic Testing Rig Setup

A custom built catalytic testing rig was used to carry out all catalytic testing on the Ni 'doped' zeolites. The rig can be thought of as five distinct units connected together to form one complete system, shown schematically in Figure 3.5.

The individual gas inlet feeds of helium, hydrogen, methane, oxygen, carbon dioxide and synthesis gas, allow each gas to be independently turned on or off. These are connected, via stainless steel piping, to mass flow controllers, giving the ability to control the volumes of each gas passing through the system. The gases are then channelled through to a stainless steel manifold, where they can be combined to yield the required reaction composition.

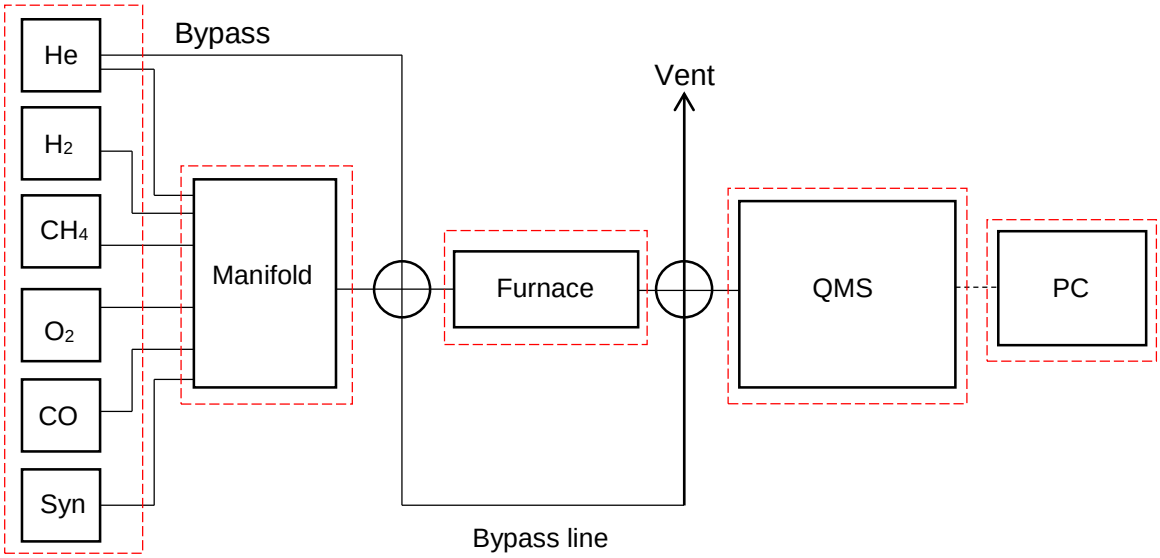

Figure 3.5. Schematic of the catalytic testing rig, highlighting the five distinct units comprising the system; gas inlet feeds, manifold, furnace, QMS and PC.

The resulting gaseous mixture was fed into a quartz reactor tube; length 240 mm, inner diameter 5 mm, thickness 1 mm; sitting in a brick furnace, secured using Cajon Swagelok fittings. The furnace consists of two hollowed out insulating bricks with heating elements sitting within these hollowed out sections. The heating elements are comprised of Nichrome wire coiled around ceramic tubes; the temperature was monitored and regulated by a k-type thermocouple connected to a Eurotherm 818 controller. The sample (40 mg ± 0.5 mg) sits within the quartz reactor tube between two quartz wool plugs, to stop any movement of the sample as the gaseous mixture passes over it.

The catalytic testing rig contains two four-way values allowing control of gas flow through two different lines; the reactive line, going through the quartz tube in the furnace, and the bypass line, which runs parallel to the reactive line and out to a vent. The use of two gas flow lines allows the reactant gas mixture to settle down before being passed over the catalyst, and for an inert atmosphere, of helium, to be present around the catalyst pre-reaction.

Once settled, the reactant gas mixture was passed over the catalyst and the resulting gaseous products are channelled via a glass capillary into a quadrupole mass spectrometer

(QMS), MKS minilab. The MKS minilab used was a quadrupole mass spectrometer able to follow up to twelve mass fragments simultaneously. The capillary line leading to the mass spectrometer was heated to approximately 150 °C to ensure continued gas flow, and to allow quantification of the products produced.

3.4.2 Catalyst Reduction

Prior to any reaction taking place, the material must first be reduced. The reduction was carried out using a 10% hydrogen in helium mix, where the total flow rate was 20 mL min^{-1}. The reaction carried out was a temperature controlled reduction (TPR) where the temperature of was increased at 10 mL min^{-1} up to 900 °C. The hydrogen consumption and water production were monitored using the QMS, with measurements being taken every 20 seconds. The area under each of the resulting traces is proportional to the amount of nickel present within the material. Once the temperature reached 900 °C, the material was cooled under the 10% hydrogen mixture to ensure the material remains in the reduced state.

3.4.3 Reforming Reactions

Reforming reactions were carried out using a variety of gaseous mixtures and two different thermal conditions.

Catalytic activity was tested using four different reaction mixtures. The partial oxidation, dry reforming and biogas reforming of methane were studied, along with the oxidation of synthesis gas, a product of methane reforming. The partial oxidation of methane was carried out using a 2:1 mixture of methane to oxygen. The mixture comprised 10% or 20% methane and 5% or 10% oxygen diluted in helium, to yield a total flow rate of 20 mL min^{-1}. The dry reforming of methane was carried out using a 1:1 mixture of methane to carbon dioxide. The mixture comprised 5% or 10% methane and 5% or 10% carbon dioxide, diluted in helium, to yield a total flow rate of 20 mL min^{-1}. The biogas reforming was carried out using

a 2:1 mixture of methane to carbon dioxide. The mixture comprised 10 % methane and 5% carbon dioxide, diluted in helium to yield a total flow rate of 20 mL min^{-1}. The oxidation of synthesis gas was carried out using a 2:1:1 mixture of hydrogen to carbon monoxide to oxygen. The mixture comprised 10% hydrogen, 5% carbon monoxide and 5% oxygen, diluted in helium to yield a total flow rate of 20 mL min^{-1}.

As mentioned above there were two different thermal conditions used to test the catalytic activity; a temperature programmed reaction and an isothermal reaction. For temperature programmed reactions, the reaction profile was monitored for both increasing and decreasing temperature. The temperature was increased at 10 °C min^{-1} up to 900 °C and then decreased at 5 °C min^{-1} to 200 °C or until the reaction has stopped. Measurements were taken every 12 seconds to yield an accurate reaction profile. The reaction was monitored for both the increasing (forward) and decreasing (reverse) temperature to elucidate any hysteresis effects. For isothermal reactions, the reaction profile was monitored at a constant temperature to elucidate the stability of the catalyst for a particular reaction over time. The temperature for the isothermal reactions was chosen from the reaction profile obtained in the temperature programmed reaction for the same material and the same reaction mixture. The reactant mixture was passed through the bypass line to allow the gases to settle and so the furnace could reach the desired temperature. The reactant mixture was then passed over the catalyst and left for the desired amount of time. Measurements were taken every minute to yield a reaction profile over time.

3.4.4 Catalyst Oxidation

Post reaction, an oxidation was performed to ascertain how much carbon had been deposited on the catalyst surface. The temperature programmed oxidation (TPO) was carried out using a 10% oxygen in helium mix, where the total flow rate was 20 mL min^{-1}. The production of carbon dioxide and carbon monoxide was monitored using the QMS, with measurements being taken every 20 seconds, where the area under the traces is

proportional to the amount of carbon deposition. A standard carbon curve was setup, from known masses of carbon, to allow a mass of carbon to be obtained. It should be noted that the masses obtained are only that of the 'observable' carbon, which is dictated by the limits of the mass spectrometer, and therefore it is conceivable that there is a small amount of additional carbon not reported.

3.4.5 Control Samples

The intermediate samples of the Ni catalyst syntheses were tested for their methane reforming capabilities to ensure that the catalytic activity was due to the 'doping' of the zeolite framework with nickel. For the MFI and MTW materials, the sodium containing intermediates were tested and for the MEL material the potassium material was tested. In addition to the control zeolite samples, the catalysis of the quartz tube and quartz wool were tested. For all control samples mentioned, no catalytic activity was observed, therefore confirming that the catalysis observed in this study is due to the presence of the nickel in the zeolite framework.

3.4.6 Mass Spectrometry

Mass spectrometry is a very common characterisation technique and due to its high sensitivity, it can be utilised in many different ways.

As part of the analysis, a mass spectrometer carries out three basic functions; to produce gaseous ions, to separate those ions and then to detect and record their abundance.

Compounds entering the spectrometer for analysis are first converted into gas phase ions. The spectrometer used for the catalytic testing produces these gas phase ions through electron ionisation. These ions are formed via the electron bombardment of the sample, with electrons produced from a heated filament. This bombardment produces a molecular radical cation with an odd number of electrons.

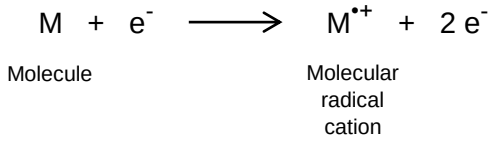

Figure 3.6. Electron bombardment of a molecule producing a molecular radical cation.

The molecular radical cations resulting from the initial electron bombardment then undergoes fragmentation to form either an ion, with an even number of electrons, and a radical or a new molecule and a radical cation.

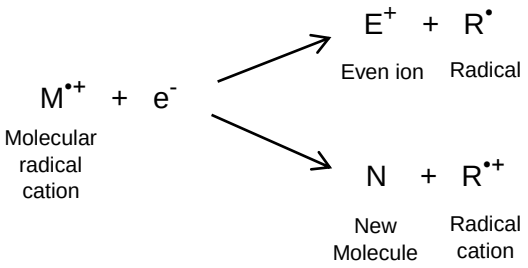

Figure 3.7. Fragmentation of the molecular radical cation forming either an ion and a radical or a new molecule and a radical cation.

These new species can then in turn undergo further fragmentation, to yield progressively smaller species. This fragmentation pattern is unique to each parent molecule and each fragment will have a distinct mass to charge ratio. Once detected, the resulting spectrum of the mass to charge ratios from each fragment is akin to a fingerprint for each parent molecule.

The mass spectrometer used as part of the catalysis rig was a quadrupole mass spectrometer able to follow up to twelve gas fragments simultaneously. Quadrupole mass spectrometers are named due to the nature of the mass analysers within them. These quadrupole mass analysers, as the name would suggest, consist of four electrically conducting parallel rods, where the opposite pairs of electrodes are electronically

connected[5]. The pairs of rods are oppositely charged whereby the rods of the same charge are spatially opposite each other, as shown in Figure 3.8. Each pair of rods has a direct current (DC) and radio frequency (RF) field applied to it. As quadrupoles rely on the ion's trajectory stability to separate them by their mass to charge ratios (m/z) the rods must be perfectly parallel[5].

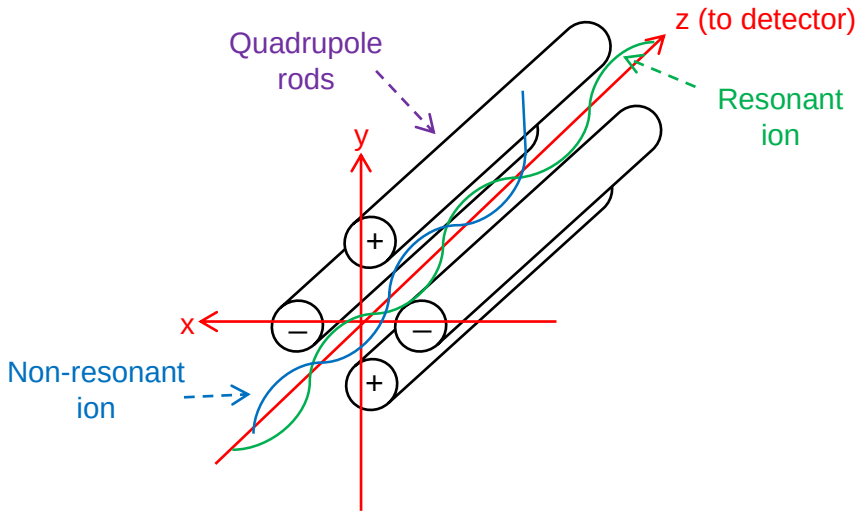

Figure 3.8. A schematic of a quadrupole analyser, showing the four parallel rods with opposing charges in the different planes.

The ions, resulting from the electron bombardment and subsequent fragmentation, are channelled through the quadrupole. These positively charged ions are drawn towards the negatively charged rods. As they approach the rod there are two possibilities, the first is that the ions continue this path, where they eventually collide with the rod and are subsequently discharged. The second possibility is again these ions are drawn towards the negatively charged rods, however, if the RF field switches before the ion is discharged, it will change direction, back towards the central space between the rods. Ions that are able to pass through the quadrupole without being discharged, will reach the detector. The applied DC and RF voltages can be used in two ways, either to focus on an ion with a particular m/z or to continually scan for a range of m/z values by varying the voltage.

The ions that successfully travelled through the quadrupole will then reach the detector. In mass spectrometry ions are detected by; their charge, their mass or their velocity. The

detector in the mass spectrometer used in this work has a dual system utilising both a Faraday cup and a secondary electron multiplier (channeltron). In a faraday system the ions from the quadrupole strike the surface of a dynode which then emits electrons and generates an electrical current, which is in turn amplified and detected. This type of dynode is a conversion dynode where the ion collision is directly converted to a current. With a secondary multiplier, in this case a channeltron, the ions collide with a continuous curved amplification dynode where there is an emission if secondary particles, including both positive and negative ions, electrons and neutrals[5]. These secondary particles are then either attracted to the conversion dynode to create a current or to the continuous dynode from which a cascade of electrons is produced. This cascade results in an amplification of the signal up to magnitudes of 10^7, which is then collected by a metal anode and the current measured.

3.5 References

1. Bragg WH, Bragg WL. The Reflection of X-rays by Crystals. Proceedings of the Royal Society A: Mathematical, Physical and Engineering Sciences. 1913;88(605):428-438.

2. Chu B. Dynamic Light Scattering. In: Soft Matter Characterization. USA: Springer. 2008. p. 335-372.

3. Goldburg W. Dynamic light scattering. Am J Phys. 1999;67(12):1152-1160.

4. Hore P. Nuclear Magnetic Resonance. Oxford: Oxford University Press; 2015.

5. Hoffmann E, Stroobant V. Mass spectrometry. Chichester: John Wiley & Sons; 2012.

4.0 Synthesis and Characterisation of Nanosized MFI types Zeolites

4.1 Introduction

The MFI framework type was first reported in 1972 by the Mobil Oil company[1], in its aluminosilicate form, known as ZSM-5 or Zeolite Socony Mobil-5. In 1978 Flanigen *et al*[2]. reported its all silica analogue Silicalite-1.

The MFI framework is formed via the linkage of the pentasil five membered ring unit, and due to such it is part of the family of zeolites with the same name, the pentasil family, where this linkage is characteristic. It also part of the group of zeolites known as 'five-rings' where each zeolite is comprised of five-member ring linkage, but not exclusively the pentasil unit.

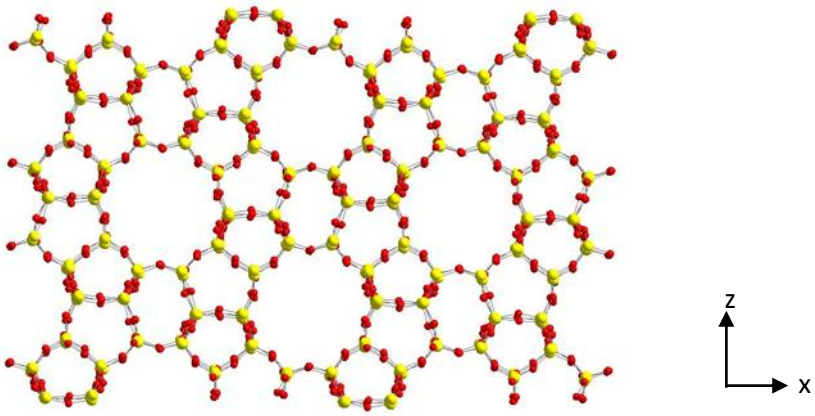

Figure 4.1. Framework structure of MFI, where red atoms are oxygen and yellow atoms are silicon, viewed down the (010) plane.

At room temperature the MFI material has orthorhombic framework symmetry with a Pnma space group and cell parameters *a* = 20.07 Å, *b* = 19.92 Å, *c* = 13.42 Å and α=β=γ= 90 °. The pore system within this framework is composed of two perpendicular 10 membered ring channels; a straight channel parallel to the (010) plane and a sinusoidal (zig-zag)

channel parallel to (100) plane[3]. It is at this intersection of these two channels that the structure directing agent sits, as shown in Figure 4.2.

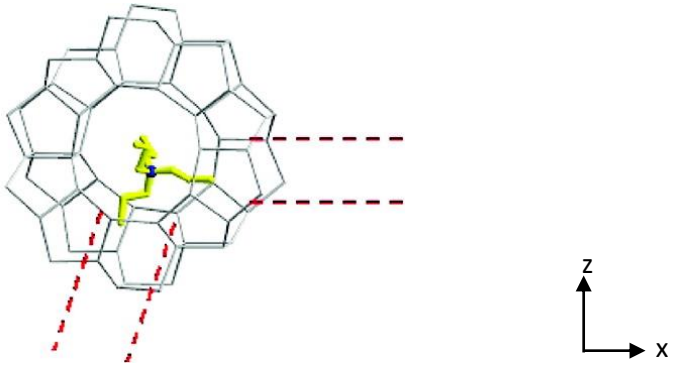

Figure 4.2. Schematic of the SDA cation within the MFI channel intersection, viewed down the straight channel. The dashed red lines outline the zig-zag channel. Taken from Fyfe *et al.* 2008[4].

As previously discussed in Chapter 1.0, structure direction and the understanding of such, plays an important role in efficiently utilising zeolites for a variety of applications. Zeolite catalysis is a particular focus for improvement in terms of efficiency of the catalysis and also the synthesis of the catalyst itself.

It is thought that the reduction of the catalyst particle size leads to a reduction of the diffusion limitations within the material, giving rise to more efficient catalysis. It is therefore vital to understand the process by which this smaller sized material forms. Previous work has been carried out into the mechanism of formation of nanosized zeolites, leading to a significant debate amongst many groups, discussed in Chapter 1.2. As such there is a needed to contribute knowledge to allow a further understanding.

Previous work with the nanosized MFI type zeolite has focused on using the tetrapropylammonium (TPA) cation for structure direction[4], however it has been shown numerous times that multiple SDAs can be used to obtain the micron sized crystals with the MFI framework[5,6]. Therefore, using one of these alternate SDAs for nanosized synthesis may yield an improved material for catalysis or have a more efficient synthesis pathway.

For the purpose of this study, the methyl tributylammonium (MTBA) cation was chosen as it is not dissimilar in size to the commonly used TPA cation and has been proven many times to be effective in yielding the MFI framework, albeit on a micron scale.

4.2 Aims

The aims of this study were to first show that the MTBA directed nanosized MFI framework could be synthesised using an alternate SDA, and then in turn utilise this synthesis in comparison with the TPA cation directed synthesis to allow insight into the mechanism of formation.

The comparison would be carried out utilising the 'timepointed' synthesis method and analysis carried out using a variety of characterisation techniques to yield a large amount of data to contribute to the mechanism debate.

4.3 Synthesis of nanosized MFI

The nanosized MTBA templated MFI material was synthesised via the clear-solution method, discussed in Chapter 2. The presence of the MFI framework was confirmed via X-ray diffraction analysis, shown in Figure 4.3. As the fluorinated (F-MFI) material is known to give the most resolved powder pattern, due to the limiting of the number of framework defects when using fluoride as a mineraliser, it was used as a comparison with the synthesised nanosized material to confirm the presence of the MFI framework. The simulated powder pattern from the International Zeolite Association (IZA) database[3] was also used as a comparison to ensure that all peaks could be accounted for.

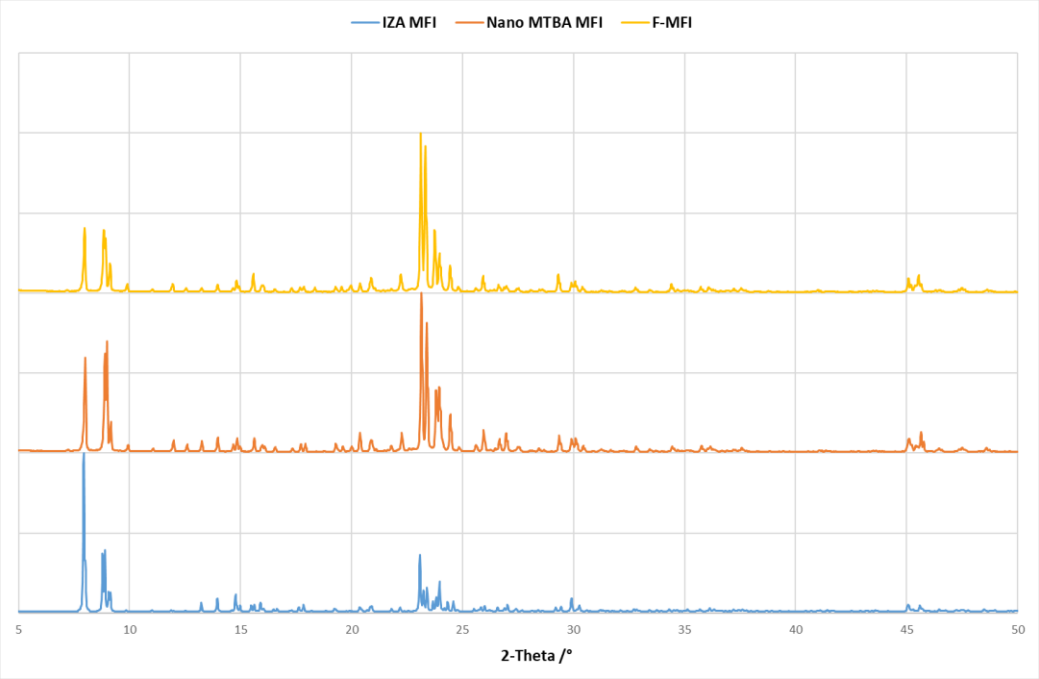

Figure 4.3. Powder pattern of the nano MTBA MFI zeolite with the F-MFI powder pattern and simulated IZA[3] pattern for comparison.

This clearly shows that a nanosized MFI zeolite can synthesised from clear solution using the MTBA cation as a structure directing agent. The resulting material gives a well resolved powder pattern, showing that the material is crystalline.

The timepointed samples, synthesis described in Chapter 2, from the MTBA and TPA cation templated reactions were characterised by capillary X-ray diffraction, solid state NMR and dynamic light scattering. These analyses allowed the reactions to be followed over time and gave further insight into the mechanism of formation of these nanosized zeolites and the effectiveness of each template to form the MFI framework.

4.4 Capillary XRD studies

The capillary X-ray diffraction analysis, and the preparation of samples for such, was carried out as described in Chapter 3.1. The advantage of using the capillary stage for powder diffraction over the standard sample holder is that lower angles can be investigated and

also small amounts of samples can be investigated which would otherwise not be suitable for the standard powder sample holders. For the purposes of clarity, only the Bragg region, between 7.5° and 9.2° of the powder patterns will be shown. The two peaks found within this region are diagnostic of the formation of the MFI framework, focussing on this region therefore allows slight changes between each timepointed sample to be seen.

4.4.1 TPA mediated reaction XRD results

The stacked plot of the Bragg region for the TPA mediated MFI material is shown in Figure 4.4.

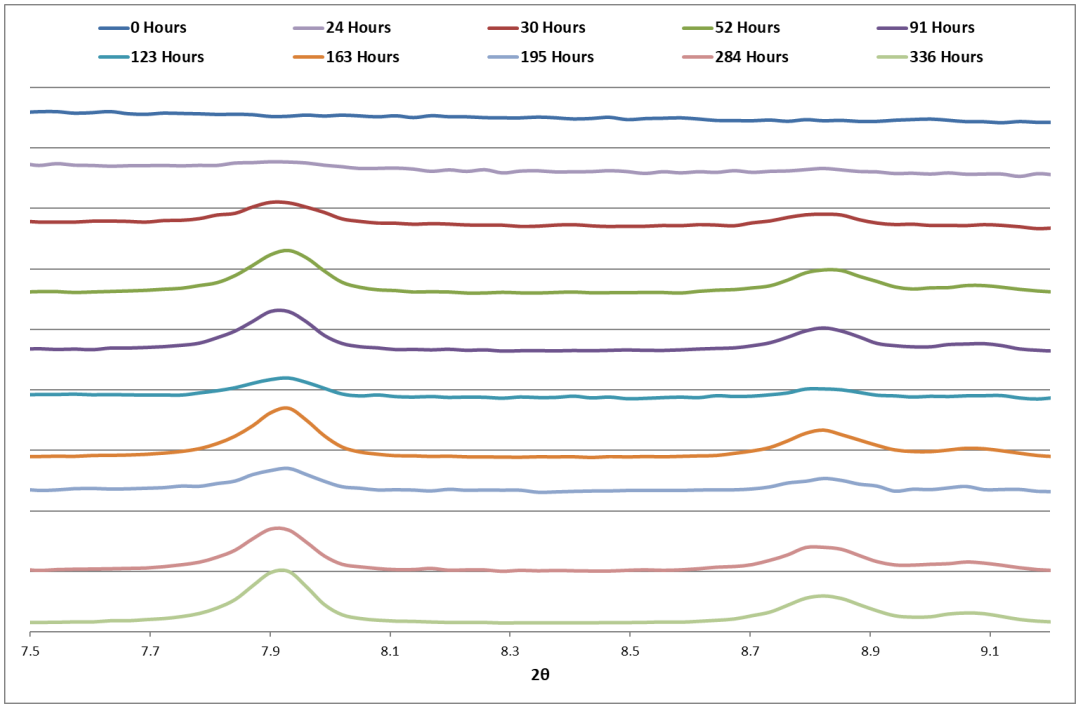

Figure 4.4. Stacked powder patterns of the Bragg region for the TPA mediated timepoint samples.

The TPA mediated reaction shows the presence of low intensity Bragg peaks from the 24 hour timepointed sample. The occurrence of such indicated that there a small amount of crystalline MFI material present from early on in the reaction. These Bragg peaks increase in intensity over time showing the presence of a larger amount of crystalline material in the samples.

The full width at half maximum (FWHM) values for both Bragg peaks as a function of time are shown in Figure 4.5.

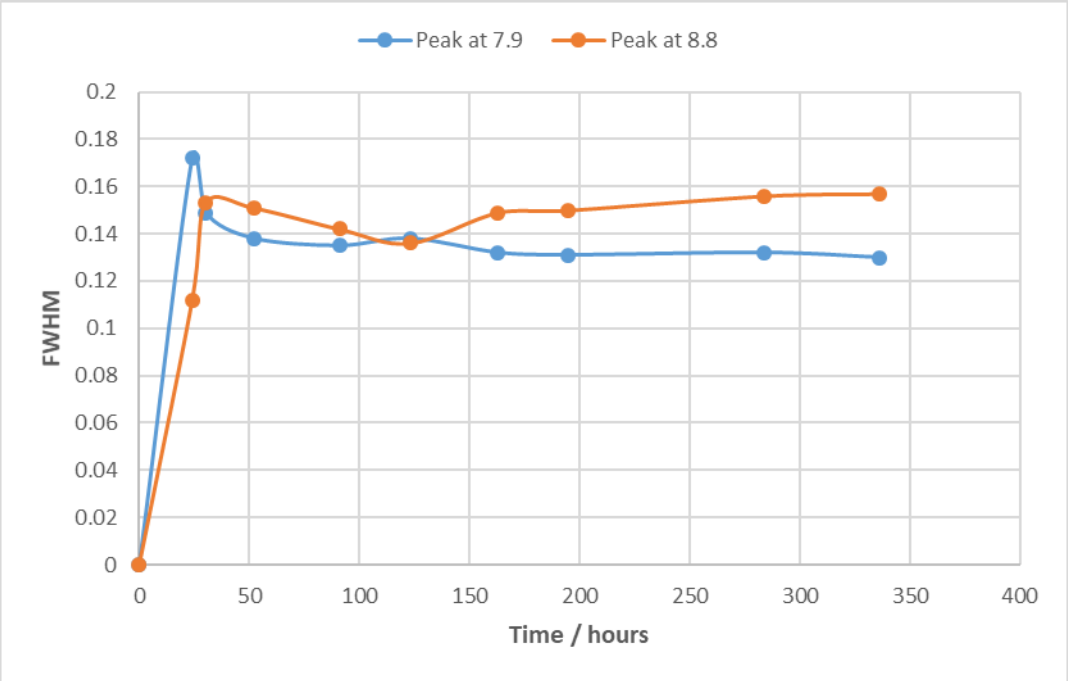

Figure 4.5. FWHM values of the Bragg peaks at 7.9° and 8.8° for the TPA mediated reaction vs time.

The FWHM data shows that the TPA mediated reaction has a rapid increase in rate from the 0 hour timepoint until the 30 hour timepoint. After which the reaction rate remains relatively steady until the final timepoint is taken.

4.4.2 MTBA mediated reaction XRD results

The stacked plot of the Bragg region for the MTBA mediated MFI material is shown in Figure 4.6.

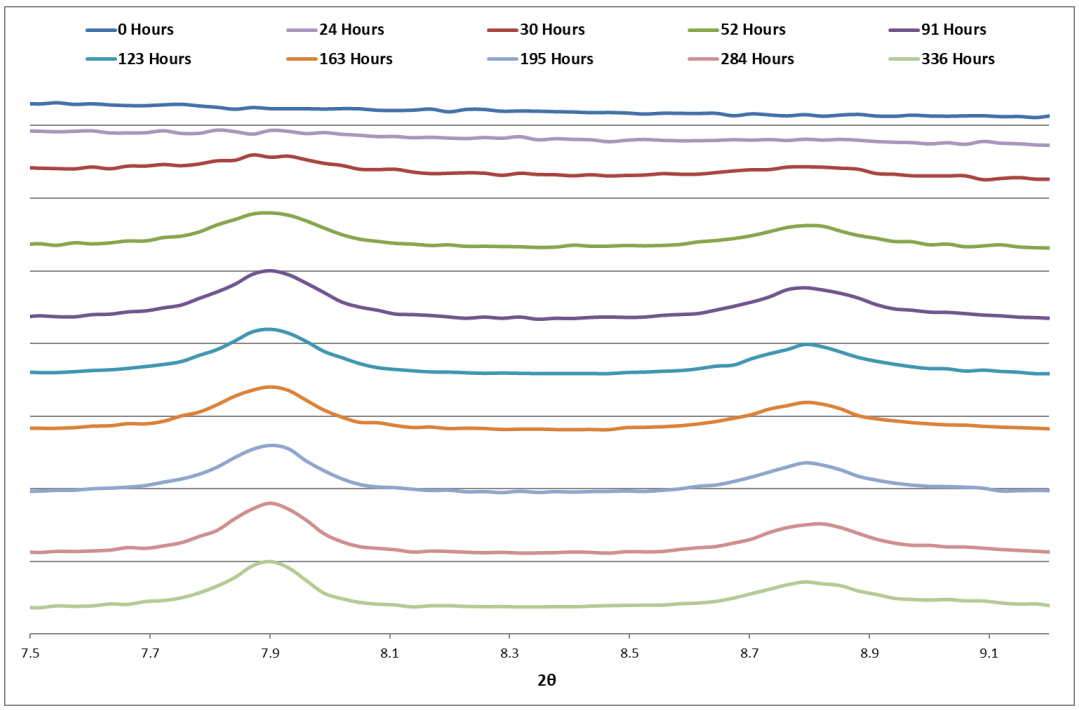

Figure 4.6. Stacked powder patterns of the Bragg region for the MTBA mediated timepoint samples.

The MTBA mediated reaction shows the presence of Bragg peaks from the 30 hour timepointed sample, later than the TPA mediated synthesis. This indicates that the MFI framework is not formed in the reaction mixture until around 30 hours. These Bragg peaks again increase in intensity over time, showing that the MFI framework is still being formed even at the later timepoints.

The full width at half maximum (FWHM) values for both Bragg peaks as a function of time are shown in Figure 4.7.

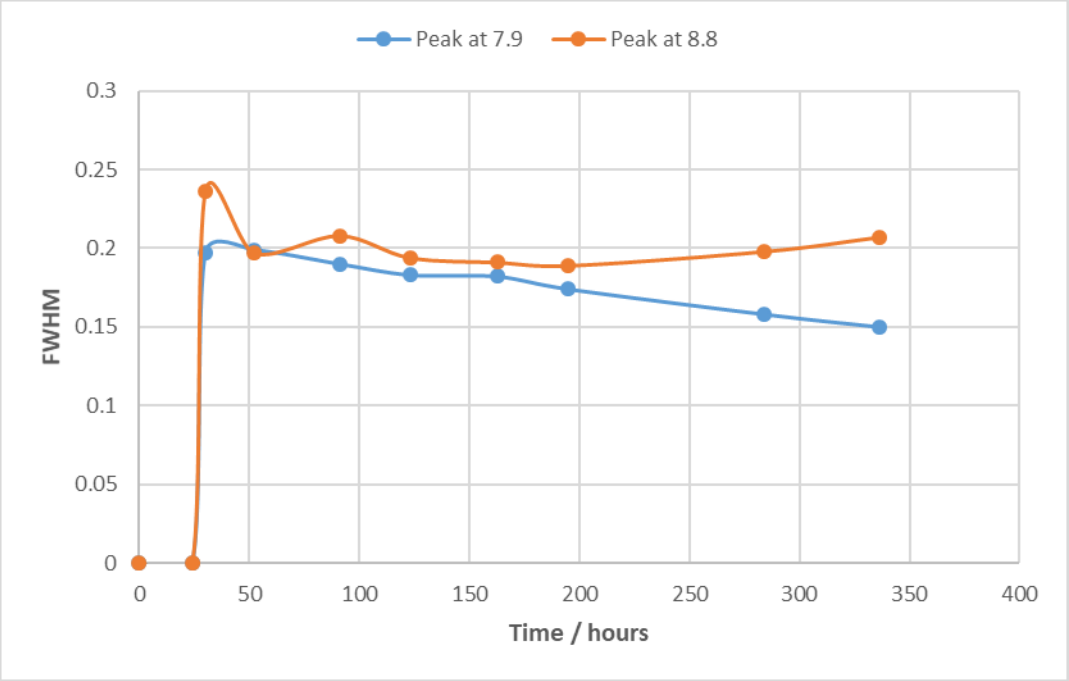

Figure 4.7. FWHM values of the Bragg peaks at 7.9° and 8.8° for the MTBA mediated reaction vs time.

The FWHM data shows that the MTBA mediated reaction has a rapid increase in rate of reaction from the 24 hour timepoint to the 30 hour timepoint. After which, much like the TPA mediated reaction, the rate is relatively stable until the final timepoint.

4.4.3 Conclusions and comparisons of the XRD results

These results indicate that as the MFI framework Bragg peaked are observed in the TPA mediated reaction before the MTBA mediated reaction, the TPA cation is able to form the MFI framework more quickly than the MTBA cation.

The FWHM values for both SDA mediated reactions remained relatively stable over time, however on examination of the powder patterns it is clear that the peaks observed are becoming more resolved as the reactions progress. This stability in FWHM values could be attributed to the presence an amorphous material with small amounts of crystalline material progressing to a completely crystalline material, as shown in Figure 4.8.

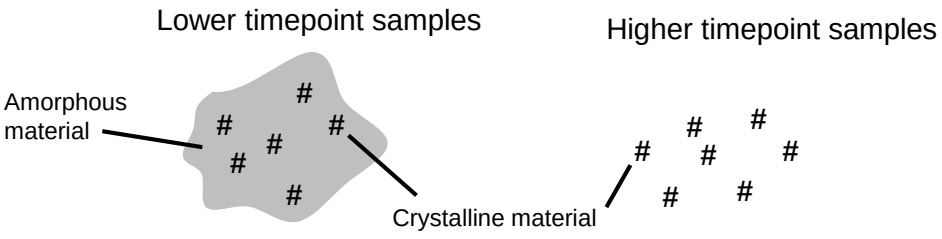

Figure 4.8. A representation of the postulated composition of the timepointed samples taken in the nanozeolite syntheses.

The suggested material compositions shown in Figure 4.8 would give rise to similar FWHM values for the observed Bragg peaks. The lower timepointed composition would result is a less intense and broad peak, whereas the high timepointed composition would result in a more intense and more resolved peak. This theory would be in favour of a spontaneous crystalline mechanism of formation as opposed to the proposed aggregative mechanism[7-12]. If an aggregative synthetic route were taking place, the FWHM values would be expected to increase as the reaction progresses due to the domino-like effect of the crystalline nanoslabs and nanoblocks etc. aggregating together, with little amorphous material present. A spontaneous crystallisation mechanism allows for the simultaneous presence of amorphous and crystalline material leading to the stable FWHM values presented.

4.5 Solid state NMR studies

The local environment of the carbon-13, in the arms of the structure directing agents, and the silicon-29 in the framework was probed to gain further insight into the formation over time of the nanosized zeolite. The carbon-13 studies allowed the location of the SDA within the channels of the zeolite framework to be studied. The silicon-29 studies allowed the framework itself to be studied.

Both NMR analyses were carried out on a select number of the timepointed samples rather than the full range taken. The analysis could not be carried out on all timepointed samples

due to the time constraints that apply to solid state NMR experiments when compared with its solution state counterparts.

4.5.1 ^{13}C {^{1}H} CP MAS NMR

The proton decoupled cross polarisation carbon-13 experiments were carried out as described in Chapter 2. These experiments, as mentioned above, allow the local environment of the hydrocarbon chains of the structure directing agents to be probed as they sit at the interchange between the so called straight and zigzag channels within the MFI framework. The orientation of the SDA cation at the intersection of the two channels in the MFI framework is very useful when trying to follow the reaction. The orientation of the arms pointing into the different channels, leads to them being in a different chemical environment which then in turn leads to the splitting of the end chain methyl group signal. The presence of the split methyl peak is therefore diagnostic of the formation of the MFI framework as this peak splitting is only seen when the channels are fully formed

The ^{13}C {^{1}H} CP MAS NMR spectra obtained for the TPA mediated timepointed samples are shown in Figure 4.9, their resonances have been assigned to the tetrapropyl ammonium salt structure in shown in Figure 4.10.

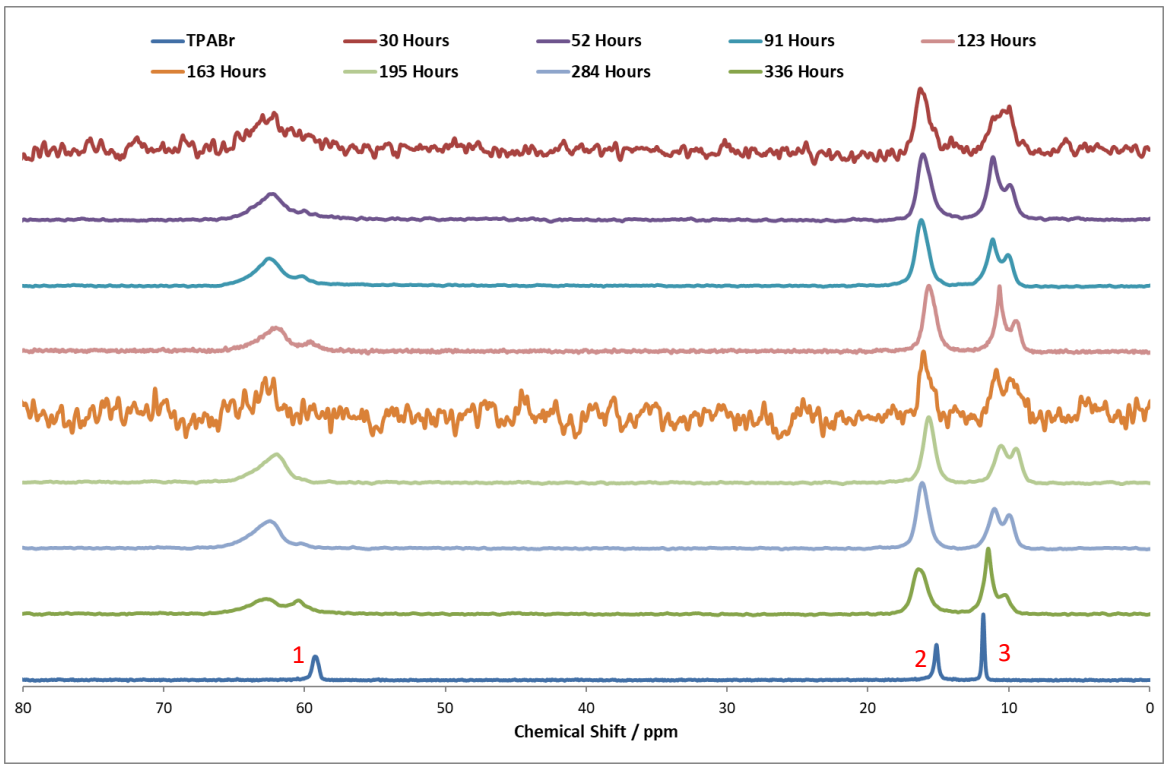

Figure 4.9. Stacked ^{13}C {^{1}H} spectra for the TPA mediated timepoint samples with the spectrum of TPA Br for comparison. Labels correspond to the TPA^{+} structure in Figure 4.10.

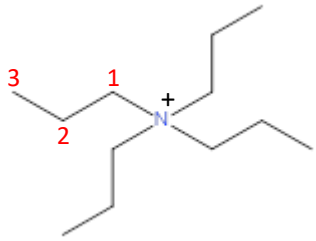

Figure 4.10. TPA^{+} structure with labels corresponding to the peaks shown in Figure 4.9.

The characteristic splitting of the end chain methyl peak, Figure 4.10 labelled atom 3, cannot be seen at the 30 hour timepoint indicating that the tetrapropyl ammonium cation is not sitting at the intersection between the two channels in the framework. Therefore, suggesting that the framework is not fully formed after 30 hours of reaction time. The 30 hour end chain methyl signal does however show a broadening of the signal, when compared to the spectrum obtained of TPABr and of the signal at a higher shift. Although solid state NMR does give broader signals that solution state NMR, this broadening of the end chain methyl signal could be caused by the TPA cation becoming contained with a semi formed zeolite

framework. This would give rise to a number of slight different chemical environments and therefore broadening the signal. The splitting of the end chain methyl peak can be seen from the 52 hour timepoint indicating that the structure directing agent is at the channel intersection and therefore the framework has been formed.

The ^{13}C {^{1}H} CP MAS NMR spectra obtained for the MTBA mediated timepointed samples are shown in Figure 4.11, their resonances have been assigned to the methyltributyl ammonium salt structure shown in Figure 4.12.

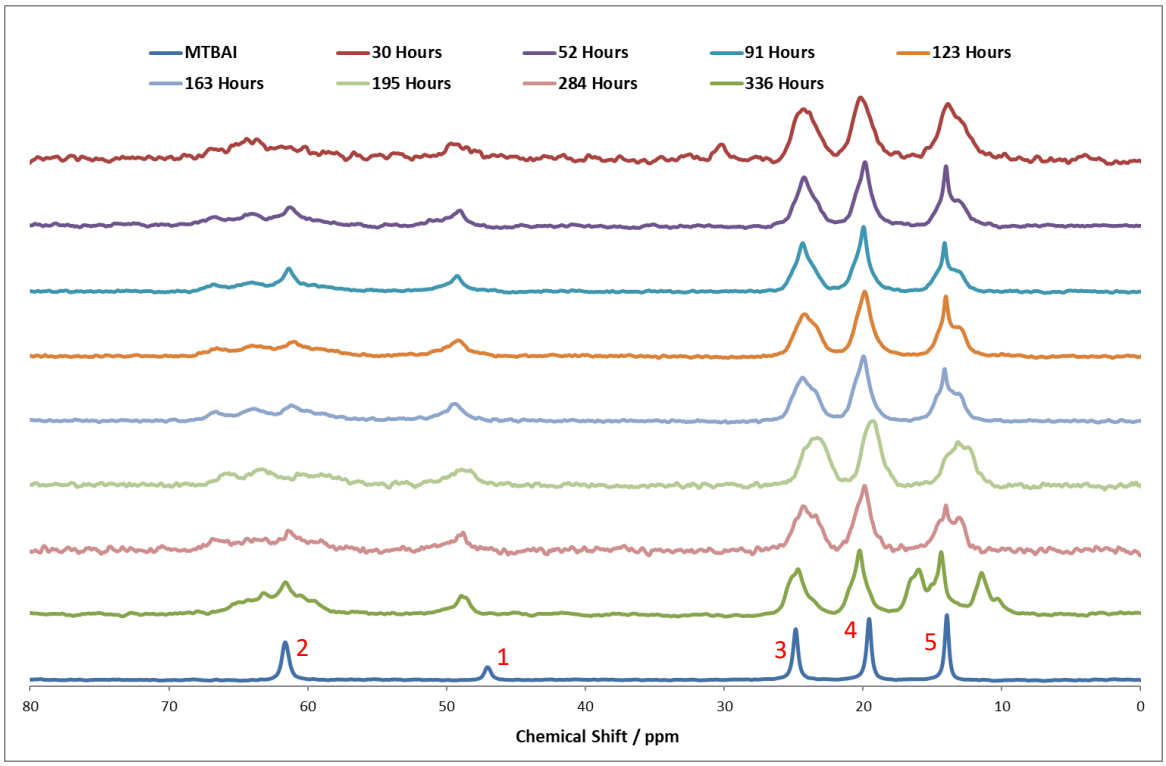

Figure 4.11. Stacked ^{13}C {^{1}H} spectra for the MTBA mediated timepoint samples with the spectrum of TPA Br for comparison. Labels correspond to the $MTBA^{+}$ structure in Figure 4.12.

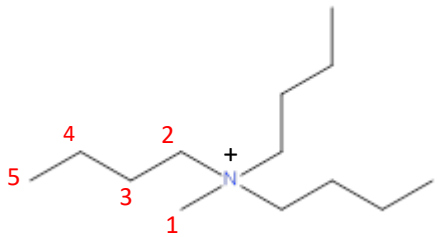

Figure 4.12. $MTBA^{+}$ structure with labels corresponding to the peaks shown in Figure 4.11.

The characteristic splitting of the end chain methyl signal, Figure 4.11 labelled atom 5 can clearly be seen for the 336 hour sample, two distinct resonances are present with a clear separation between them. This splitting confirms the formation of the extended MFI zeolite framework. The 30 hour sample does not show the splitting of the end chain methyl group, however, similar to the TPA mediated samples, the signal does show a broadening, suggesting that a semi formed zeolite framework may be present. The splitting of the end chain methyl signal is shown to start occurring by the 52 hour sample, with the formation of a shoulder to the signal, indicating the presence of the framework channels. This shoulder then increases in intensity as the reaction proceeds until the 336 hour timepoint where the signal completely splits.

From these results it is clear that the MTBA cation was more effective at forming the MFI framework after 336 hours, due to the extent of the splitting of the end chain methyl signal. The ^{13}C spectra from both reactions show that the extended zeolite framework was not formed after 30 hours but they do show indications that a semi formed framework could be present. Both nanozeolite reactions show clear evidence of the formation of the framework after 52 hours has elapsed.

4.5.2 ^{29}Si {^{1}H} CP MAS NMR

The proton decoupled cross polarisation silicon-29 experiments were carried out as described in Chapter 2. These experiments, as mentioned, allow the local environment of the silicon atoms within the MFI zeolite framework to be probed. For solid state silicon spectra, the resulting peaks are usually broad and not well resolved. These shifts are denoted by a Q number, ranging from Q1 to Q4. Q1 resonances result from $SiO(OH)_3$ species, Q2 resonances result from $SiO_2(OH)_2$ species, Q3 resonances result from SiO_3OH species and Q4 resonances result from SiO4 species. The most meaningful conclusions for zeolite samples can be drawn from the Q3 to Q4 ratio. The Q3:Q4 describes how crystalline the sample is, and for the purpose of this study, serves as an indication of the progress of

the nanozeolite reaction as the more crystalline the sample the further the reaction will have progressed from the amorphous starting material.

Figure 4.13 shows the obtained ^{29}Si {^{1}H} CP MAS NMR spectra for the TPA mediated nanozeolite reaction. It can be seen that the Q3 resonances from the 30 hour to the 336 hour sample decrease in intensity, indicating a reduction to the number of framework defects present. The Q4: Q3 ratio for the 30 hour sample was 1: 0.85 and for the 336 hour sample it was 1: 0.50, thereby confirming the increase in crystallinity and decreases in framework defects.

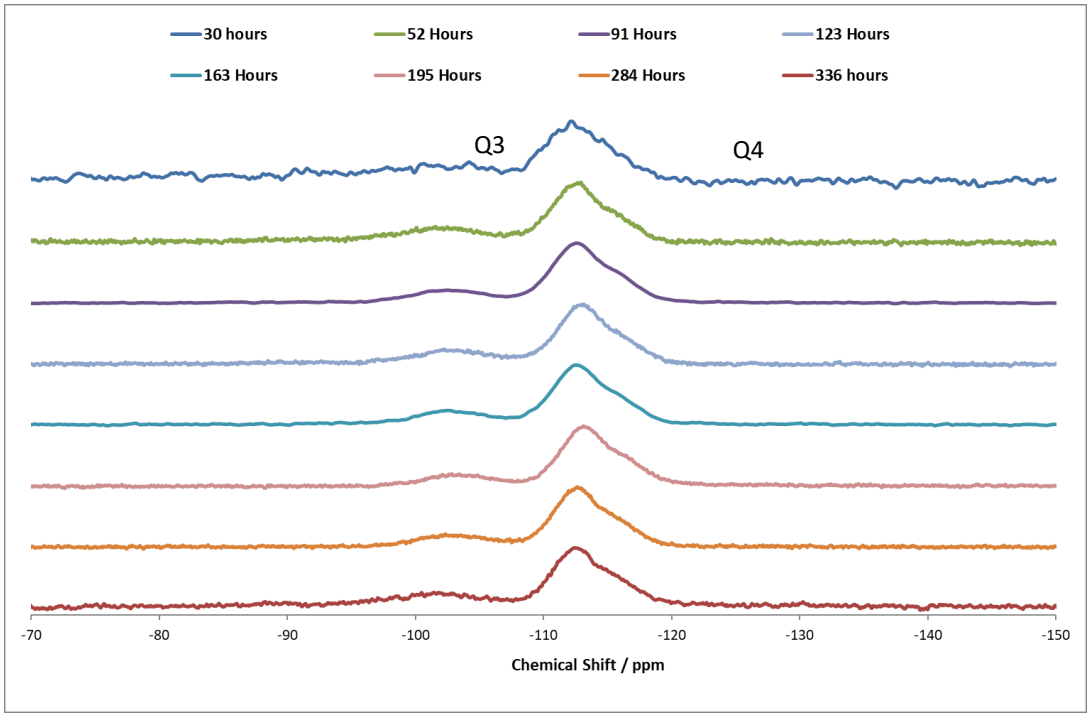

Figure 4.13. Stacked ^{29}Si {^{1}H} spectra for the TPA mediated timepoint samples.

Figure 4.14 shows the obtained ^{29}Si {^{1}H} CP MAS NMR spectra for the MTBA mediated nanozeolite reaction. The Q3 resonances between the 30 hour and the 336 hour samples are seen to significantly decrease in intensity as the reaction proceeds, along with an increase in the Q4 intensity. Again indicating the presence of the crystalline MFI framework with a decreasing number of framework defects as the reaction proceeds. The Q4: Q3 ratio

for the 30 hour sample was 1: 0.48 and for the 336 hour sample it was 1: 0.30, again confirming the increase in crystallinity and reduction of defect sites.

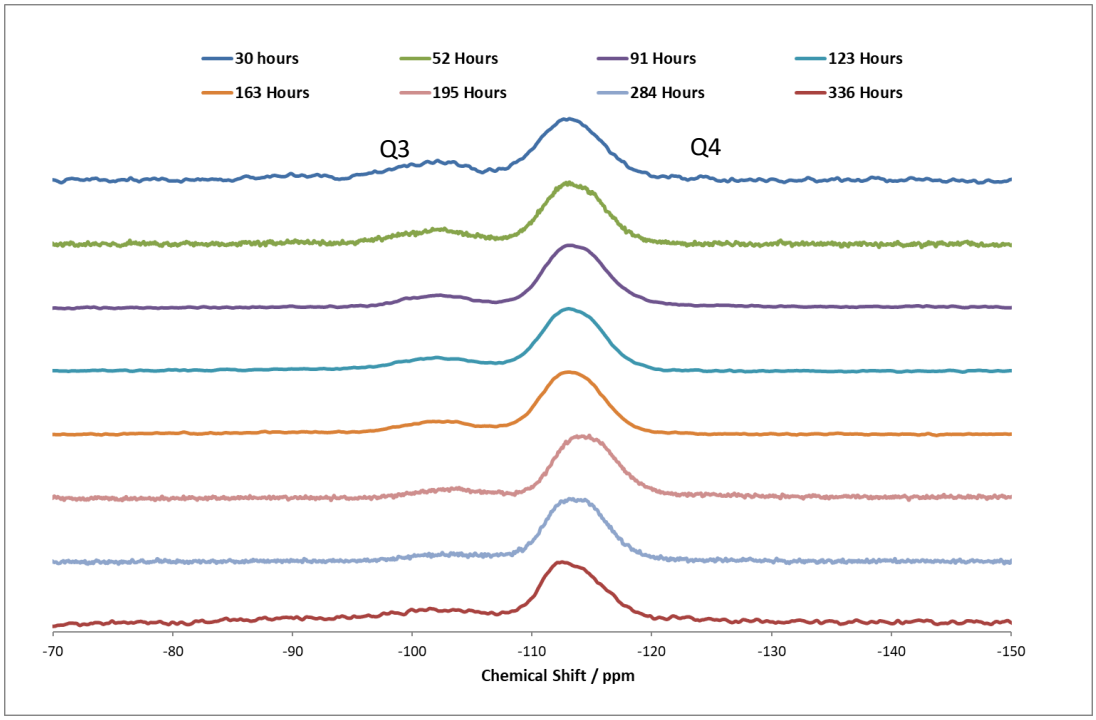

Figure 4.14. Stacked ^{29}Si {^{1}H} spectra for the MTBA mediated timepoint samples.

From these results it is clear that the MTBA template yields a more crystalline MFI framework with fewer defects. This is shown in the Q4:Q3 ratio for the 36 hour samples, in which the MTBA mediated reaction showed a higher ratio of 1: 0.3 as opposed to the ratio of the TPA mediated reaction of 1: 0.5.

4.5.3 Conclusions from the SSNMR investigations

The splitting of the end chain methyl signal in the ^{13}C studies at early timepoints for both the TPA and MTBA templates suggest that the MFI framework is beginning to form, with the SDAs sitting at the intersection between the straight and sinusoidal channels within the framework. The high Q4 to Q3 ratios, in the ^{29}Si studies, indicate the presence of a well formed and crystalline material. This is unlikely to be caused from the aggregates proposed

by Martens group[7-12], as the presence of smaller aggregates would lead to the occurrence of more Q3 silicon sites.

4.6 DLS Particle size studies

Dynamic light scattering was used to determine the change in particle size over time. The particle size was an important attribute of the timepointed sample to follow as it gives an overall indication of the progress of the reaction. The samples were prepared and analysed via the method described in Chapter 2.2.

4.6.1 TPA samples

The DLS particle size distributions for the TPA mediated nanozeolite synthesis are shown in Figure 4.15.

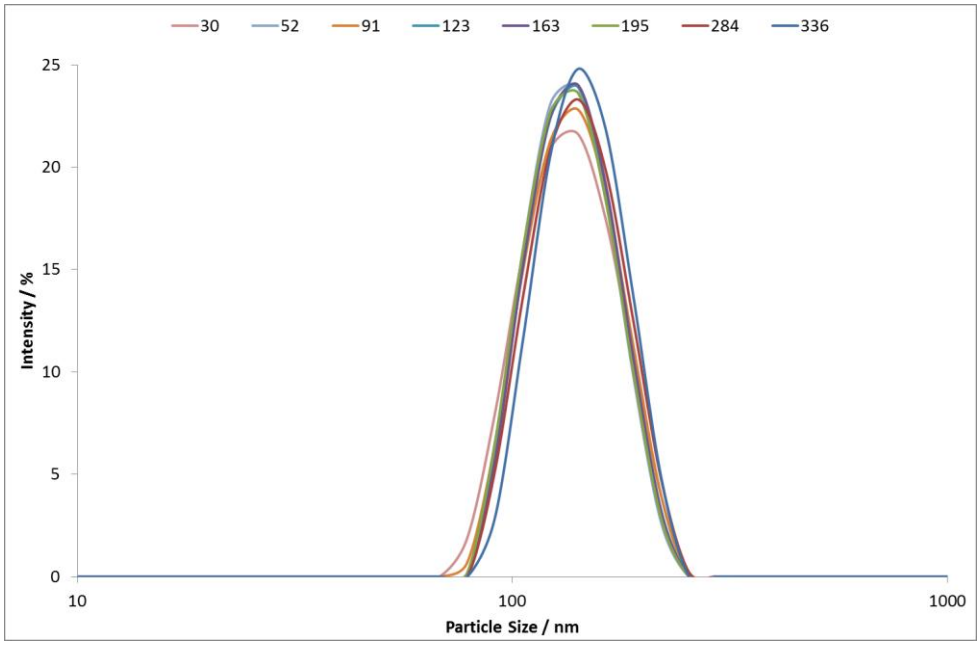

Figure 4.15. DLS distributions for the TPA mediated reaction.

From this distribution of particle sizes, it is clear that many of the timepointed samples from the TPA synthesis are localised around 135 nm. A significant change in particle size as the reaction progresses, from the 30 hour sample to the 336 hour sample, is not seen. This

would indicate that the reaction has gone to completion after just 30 hours of reaction time. The particle size distributions do not broaden or narrow over time, suggesting that the TPA template has ceased its structure directing effect, if it were still having an effect both smaller and larger particles would be formed therefore broadening the size distribution. These results are in disagreement with the suggested aggregation mechanism, suggested by the Martens group[7-12], as this would show more broad size distributions from the formation of the various nano-species such as nanoslabs and nanoblocks.

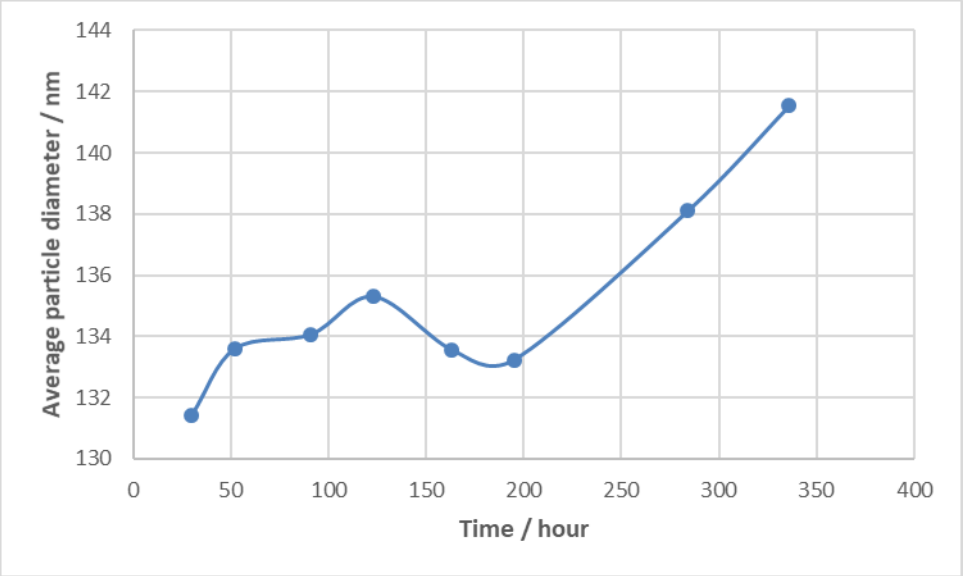

Figure 4.16. Average particle diameter vs time for the TPA mediated reaction.

The average particle sizes vs time for each TPA mediated timepoint samples are shown in Figure 4.16. It can clearly be seen that there is little difference in particle size from the 30 hour to the 336 hour samples, with an increase of approximately 10 nm. The overall increase seen is not stable over the course of the reaction, with a small decrease in particle size for the 163 and 195 hour samples. This decrease in particle size could be attributed to a sudden increase in crystallisation from an amorphous material. These results support a synthesis mechanism of spontaneous crystallisation from an amorphous mixture as opposed to the aggregative mechanism[7-12], where a decrease in particle size over time is not expected.

4.6.2 MTBA samples

The DLS particle size distributions for the MTBA mediated nanozeolite synthesis are shown in Figure 4.17.

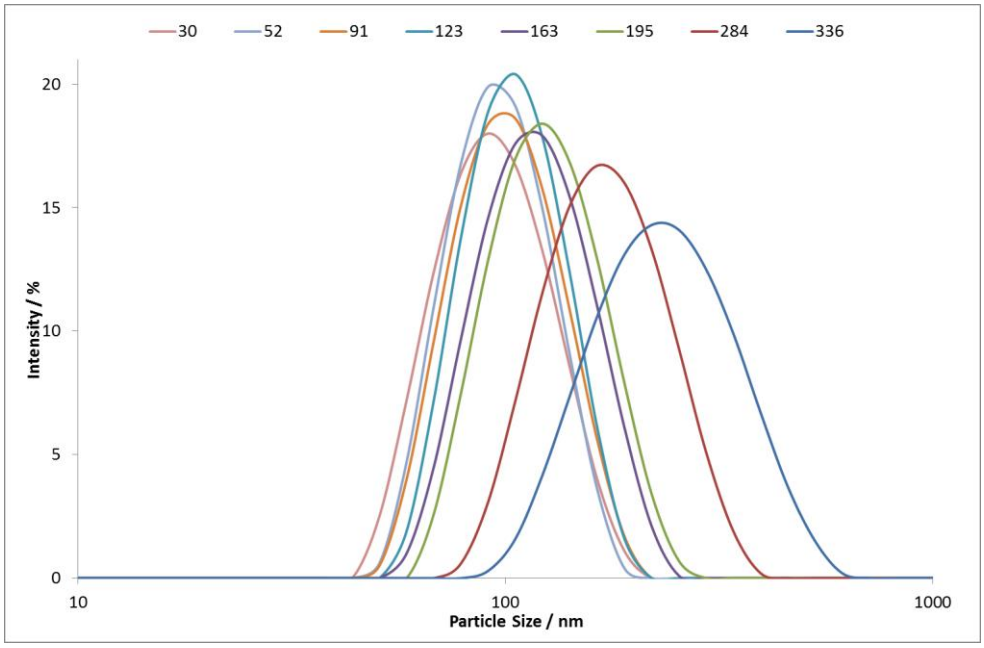

Figure 4.17. DLS distributions for the MTBA mediated reaction.

The particle size distributions for the MTBA templated reaction shows a steady increase in particle size as the reaction progresses. At the 30 hour timepoint the average particle size was found to be 98 nm. At the 336 hour timepoint the average particle size has increased to 215 nm. It is also interesting to note that as the reaction proceeds, the particle size distributions become much broader, indicating that there is a large number of varying particle sizes present in the later samples than the earlier samples. This broadening of the size distributions is in keeping with the aggregation mechanism suggested by the Martens group[7-12], and indicates the presence of a variety of differently sized species which could be attributed to the various building blocks of the aggregation mechanism.

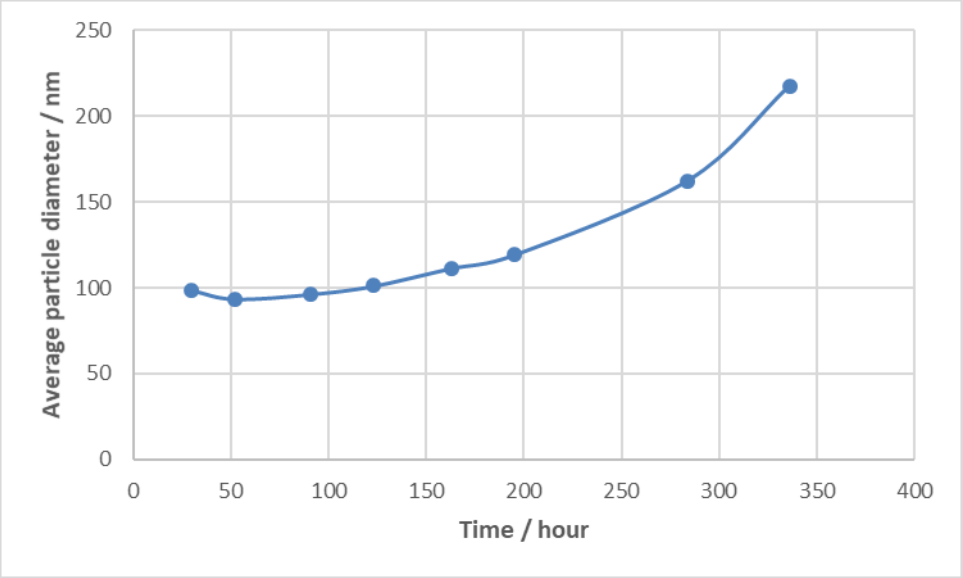

Figure 4.18. Average particle diameter vs time for the MTBA mediated reaction.

The average particle sizes vs time for each MTBA mediated timepoint samples are shown in Figure 4.18. The difference in average particle size from the 30 hour to 336 hour sample is approximately 125 nm. The overall increase follows an exponential trend, with particle size growth becoming more prevalent at later timepoints. The lack of any decrease in particle size oppose a spontaneous crystallisation mechanism and is supportive of the aggregative mechanism[7-12], where a continuous increase in particle size over time is expected.

4.6.3 Comparison and conclusions of the TPA and MTBA DLS results

When comparing the dynamic light scattering results of the TPA and MTBA mediated syntheses it is clear that they have proceeded via different routes. The particle size distributions of the two SDA templated reactions show opposing results, with the MTBA mediated reaction showing a larger size distribution than the TPA mediated reaction. These results indicate that the MTBA structure directing agent has a greater ability at forming the MFI zeolite framework over time, due to the presence of larger zeolite particles.

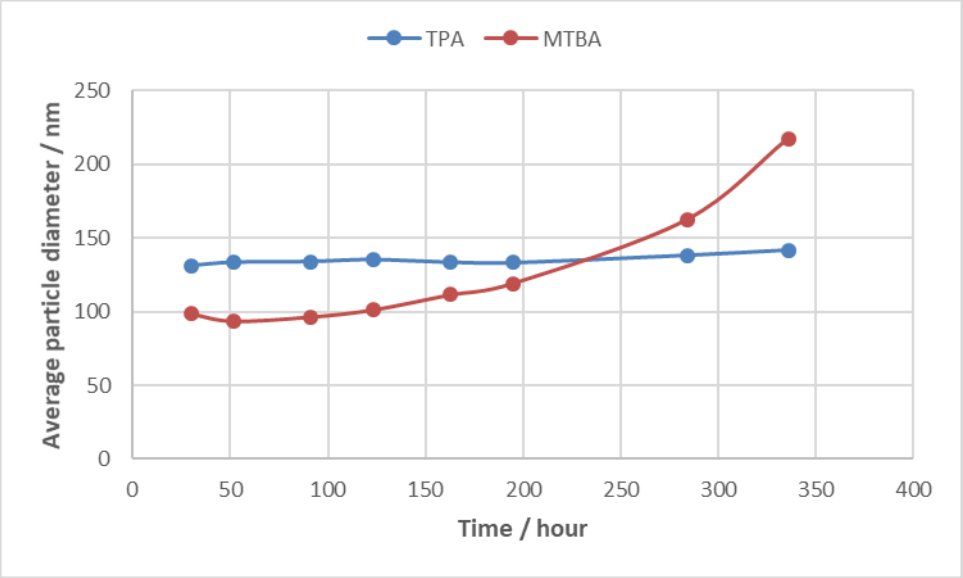

Figure 4.19. Average particle diameter vs time for the TPA and MTBA mediated reactions.

The comparison of the average particle diameter for both the TPA and MTBA mediated nanozeolite syntheses are shown in Figure 4.19. It can be clearly seen that the MTBA directed reaction allowed the formation of larger zeolite particle than the TPA mediated reaction, with a final size difference of approximately 90 nm.

The TPA directed reaction shows little evidence in agreement with the proposed aggregation mechanism, where are broader range of particle sizes would be expected. However, the MTBA directed reaction shows some indications in favour of the Martens group theory of mechanism[7-12], with a wider distribution and no decrease of particle size over the course of the reaction.

4.7 Conclusions

Two different structure directing agents, TPA and MTBA, were shown to be successful at synthesising the nano sized MFI framework. X-ray diffraction studies suggest that the TPA cation is more effective at forming the framework over a shorter time period, evidenced by the presence of Bragg peaks at earlier timepoints. The presence of these peaks at early

timepoints could suggest the aggregation mechanism is occurring, they could also however by reflecting a very rapid crystallisation mechanism. On analysis of the full width at half maximum values of the Bragg peaks for both the TPA and MTBA mediated reactions it is postulated that an aggregative mechanism is not taking place due to the stability of the data, indicating the presence of amorphous material.

Solid state NMR investigations showed that the MTBA cation is able to form a more crystalline material with fewer defects than the TPA cation, evidence by a higher Q4 to Q3 ratio. A large Q4 peak implies a well formed and crystalline material is present, which is unlikely to be the result of the many different aggregate species such as nanoslabs and nanoblocks, where more framework defects are expected due to variety of silica species present.

Dynamic light scattering results showed that the MTBA cation is more successful at forming the MFI framework over an extended period of time, as evidenced by the larger particles observed for the MTBA samples. The average particle size variation over time for the TPA mediated reaction suggests a spontaneous crystallisation mechanism is taking place. However, the average particle size variation over time for the MTBA mediated reaction suggests an aggregative mechanism is taking place.

As the conditions for both the TPA and MTBA reactions were the same, it is likely that the differences observed in the analyses between the two are due to the variations in size of the two SDAs. Further work in this area using different sized symmetrical and asymmetrical SDAs would allow more conclusive comparisons to be made as to the effect of the SDA used.

From these results it is difficult to make definitive conclusions on the synthesis mechanism taking place. However, the X-ray diffraction and solid state NMR results do strongly suggest that the aggregation mechanism is not occurring. The dynamic light scattering results for the TPA mediated reaction also disagree with the aggregative mechanism. It is therefore

concluded that the most likely mechanism of formation for the nanosized zeolites is that of spontaneous crystallisation from an amorphous mixture.

4.8 References

1. Exxon Mobil Oil Corp. US Pat. 3702886A. 1972.

2. Flanigen EM, Patton RL. US Pat. 407 865, 1978.

3. International Zeolite Association. Database of Zeolite Structures [Internet]. 2015. Available from: http://www.iza-structure.org/databases/

4. Fyfe C, Darton R, Schneider C, Scheffler F. Solid-State NMR Investigation of the Possible Existence of “Nanoblocks” in the Clear Solution Synthesis of MFI Materials. Journal Phys Chem C. 2007;112(1):80-88

5. Dib E, Gimenez A, Mineva T, Alonso B. Preferential Orientations of Structure Directing Agents in Zeolites. Dalton T. 2015;44(38):16680-16683.

6. Brace S, Wormald P, Darton R. The effect of structure directing agents on the ordering of fluoride ions in pure silica MFI zeolites. Phys Chem Chem Phys. 2015;17:11950-11953

7. Kirschhock CE a, Ravishankar R, Verspeurt F, Grobet PJ, Jacobs PA , Martens JA. Identification of precursor species in the formation of MFI zeolite in the TPAOH-TEOS-H2O system. J Phys Chem B. 1999;103:4965–4971.

8. Kirschhock CE. Mechanism of transformation of precursors into nanoslabs in the early stages of MFI and MEL zeolite formation from TPAOH-TEOS-H_2O and TBAOH-TEOS-H_2O. J Phys Chem B. 1999;103(24):4972-4978.

9. Kirschhock CE, Ravishankar R, Jacobs PA, Martens JA. Aggregation Mechanism of Nanoslabs with Zeolite MFI-Type Structure. J Phys Chem B. 1999;103(50):11021–11027.

10. Kirschhock CEA, Ravishankar R, Verspeurt F, Grobet PJ, Jacobs PA, Martens JA. Reply to the Comment on “Identification of Precursor Species in the Formation of MFI Zeolite in the TPAOH-TEOS-H_2O System.” J Phys Chem B. 2002;106(12):3333–3334.

11. Kirschhock CE, Kremer SPB, Grobet PJ, Jacobs PA, Martens JA, Centrum V, *et al*. New Evidence for Precursor Species in the Formation of MFI Zeolite in the

Tetrapropylammonium Hydroxide-Tetraethyl Orthosilicate-Water System. J Phys Chem B. 2002;106(19):1–4.

12. Kirschhock CEA, Buschmann Â, Kremer S, Ravishankar R, Houssin CJY, Mojet BL, *et al*. Zeosil Nanoslabs: Building Blocks in nPr_4N^+-Mediated Synthesis of MFI Zeolite. Angew Chem Int Edit. 2001;40(14):2637–2630.

5.0 Nano vs Micron sized Ni-MFI Catalysis

5.1 Introduction

As previously discussed in Chapter 1, the catalysis of methane reforming plays an important role in the modern world. Methane dry reforming potentially not only removes harmful carbon dioxide from the atmosphere but is also a source of hydrogen, which is becoming more heavily used as an energy source. It is therefore vital that the efficiency of catalysis is continually improved to allow these sources of hydrogen to be fully utilised.

Previous studies with the MFI framework being used a catalyst focussed on the micron sized crystals and also on the reforming of methane with carbon dioxide[1,2], shown in Equation 1.4. There are potential improvements to be made to the catalysis by reducing the particle size down to the nanoscale. On reduction of the particle size the surface area of the material becomes much greater allowing for certain surface reactions to happen at a much faster rate. Reducing the particle size also has another affect in which the diffusion limitations within the material are reduced, merely because there is a shorter distance for the species diffusing to travel. This shorter diffusion pathway does not however alter the selectivity shown by the framework to certain shapes and sizes of compounds and therefore retains its functionality.

It is therefore important to explore the effect of changing the particle size of the catalyst on the different methods of reforming methane.

5.2 Synthesis of Ni containing MFI zeolites

Prior to carrying out any catalytic testing, the MFI framework was first synthesised to contain nickel, which acts as the catalytically active metal for the reaction. To achieve the nickel containing material a sodium containing MFI intermediate was used, which was then ion-exchanged with nickel to yield to final catalyst material. This preparation was discussed further in depth in Chapter 2.

The powder XRD patterns for the nano and micron sized catalyst materials are shown in Figure 5.1. It can clearly be seen that the MFI framework is formed and is still intact after the calcination and ion-exchange processes for both the nano and micron sized materials. The powder pattern from the fluorinated MFI material and the simulated powder pattern from the IZA database[3] were both used as comparisons to ensure that the MFI framework remained intact after the heating and exchanging processes.

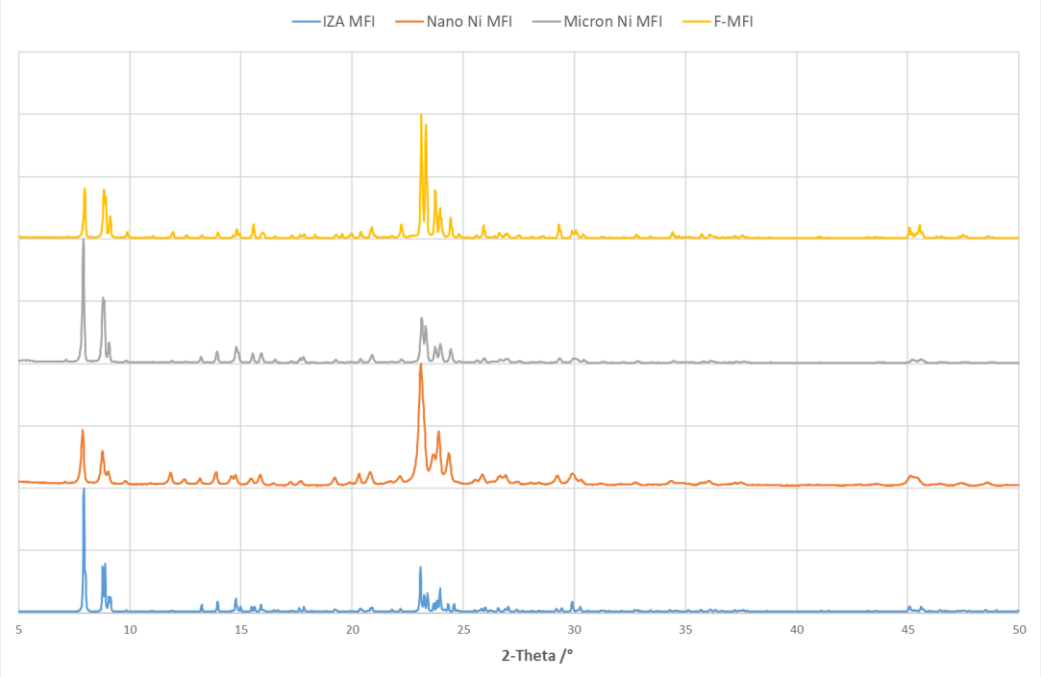

Figure 5.1. Powder patterns obtained for the Nano and Micron sized Ni MFI I comparison with the F-MFI powder pattern and the IZA simulated pattern[3].

Once confirmed to be intact the materials were then tested for their catalytic capabilities via the methods described in Chapter 2.5.3.

5.3 Reforming of biogas

As the naturally occurring mixture of biogas has a higher percentage of methane than carbon dioxide, the dry reforming reaction tested for the nickel containing MFI materials was a 2:1 mixture of methane and carbon dioxide.

5.3.1 Temperature programmed biogas reforming

The forward, heating, reaction profiles for the nickel containing micron and nano sized MFI materials are shown in Figures 5.2 and 5.3 respectively.

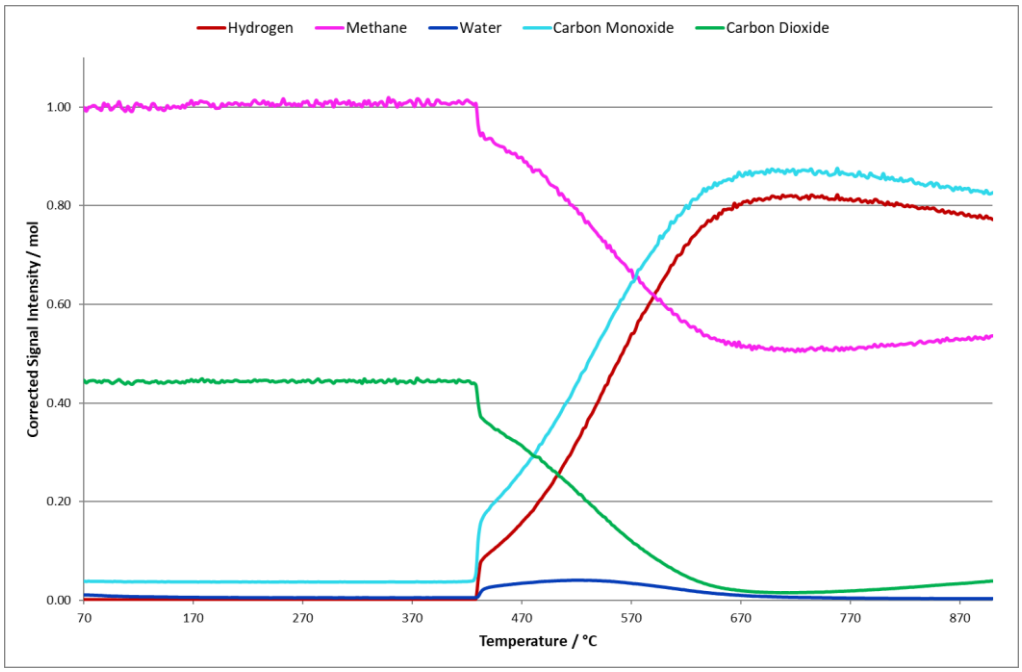

Figure 5.2. Temperature programmed biogas reforming forward reaction over micro Ni MFI.

The micron sized material shows the beginning of the reforming reaction from 430 °C, with the vast majority of the carbon dioxide being consumed. The activity present has a sharp start at 430 °C and then steadily increases to its maximum activity at approximately 670 °C. As the temperature increases up to the maximum of 900 °C the activity begins to fall.

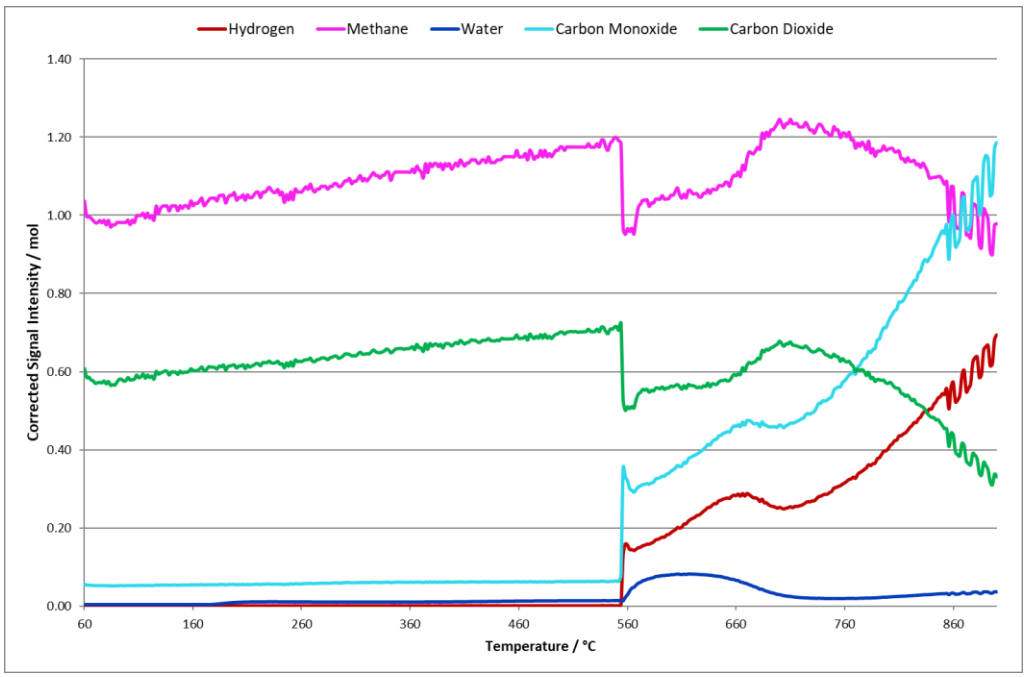

Figure 5.3. Temperature programmed biogas reforming forward reaction for nano Ni MFI.

For the nano sized material no reforming activity is observed until approximately 550 °C. After this point the reforming activity increases to its maximum activity at the maximum temperature of 900 °C. For both materials the reverse water gas shift reaction, Equation 1.5, occurs as the reforming activity begins.

The reverse, cooling, reaction profiles for both the micron and nano-sized materials are shown in Figure 5.4 and 5.5 respectively.

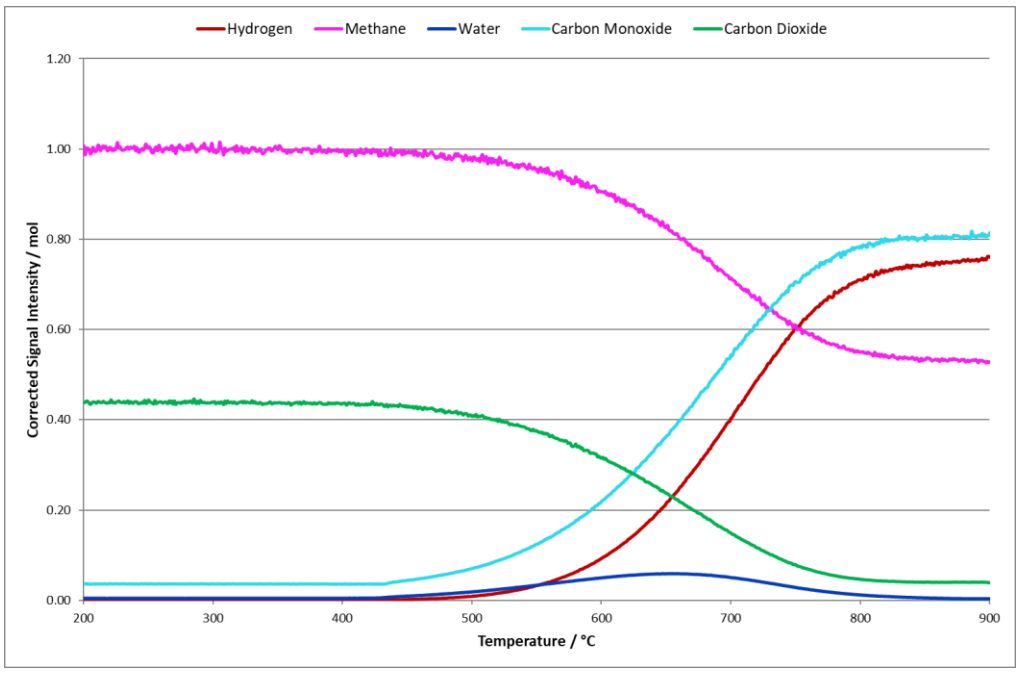

Figure 5.4. Temperature programmed biogas reforming reverse reaction for micro Ni MFI.

The reverse reaction for the micron size nickel containing material shows a similar reaction profile to that of the forward reaction, showing that the hysteresis between them is small. The reforming activity is seen to continue until approximately 800 °C after which the activity steadily decreases as the temperature decreases, there is no reforming activity observed after 400 °C. A small amount of the reverse water gas shift is still present from 400 to 800 °C.

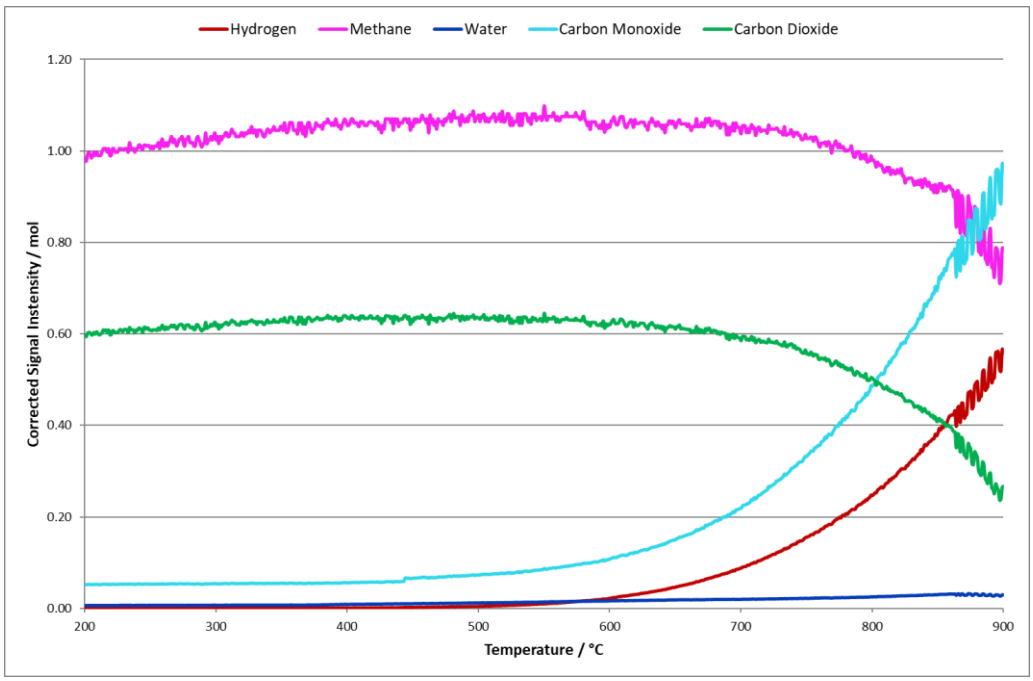

Figure 5.5. Temperature programmed biogas reforming reverse reaction for nano Ni MFI.

The nano sized material reverse reaction profile shows a steady decline in activity as the temperature decreases, with no reforming activity observed after 350 °C.

The temperature controlled oxidation experiment, described in Chapter 2.5.4, was carried out for both the micron and nano sized materials to determine the level of carbon deposition on the catalyst surface. These experiments yielded 0.135 mg of observable carbon for the micron sized MFI material, which is equal to 3.375 mg of carbon deposited per gram of catalyst used, and 0.238 mg for the nano sized MFI material, which is equal to 5.95 mg of carbon deposited per gram of catalyst used. This coking is likely due to the thermal decomposition of methane at the high temperatures and also the Boudouard reaction, in which carbon monoxide is converted into carbon dioxide and elemental carbon.

5.3.2 Isothermal biogas reforming

The isothermal biogas reforming reaction were carried out at 900 °C as a standard for all materials analysed. The reforming of biogas is an endothermic process; therefore, higher temperatures should yield a higher production of hydrogen.

The isothermal biogas reforming using the micron sized nickel containing catalyst at 900 °C is shown in Figure 5.6.

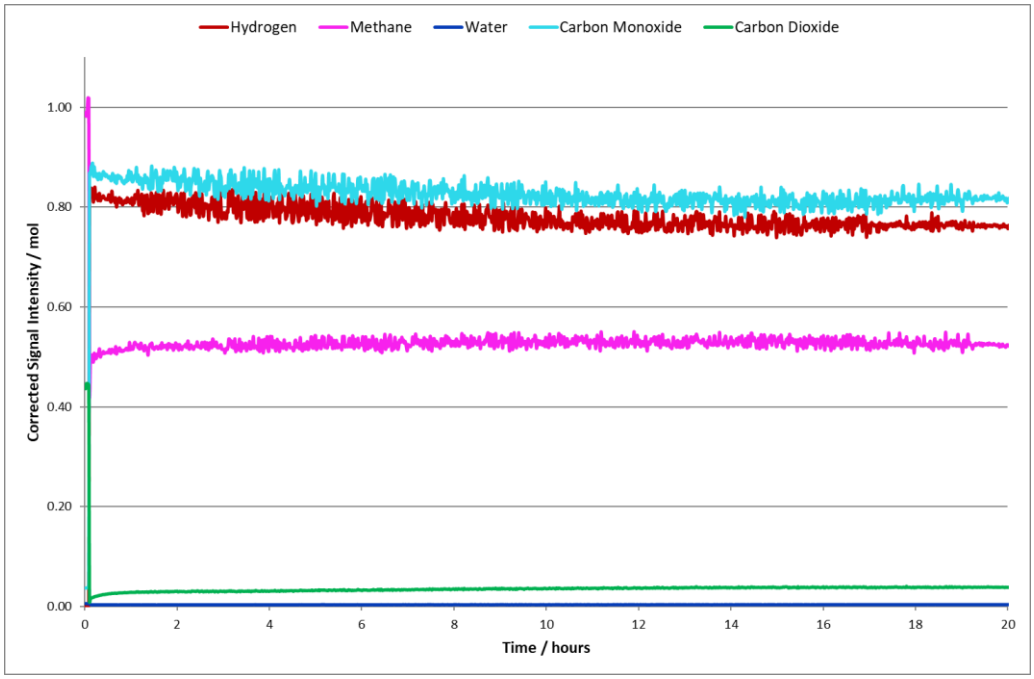

Figure 5.6. Isothermal biogas reforming over micro Ni MFI at 900 °C.

A relatively high level of reforming activity can be seen, in which 47% of the methane has been consumed. As there is a 2:1 mixture of methane to carbon dioxide being used for these investigations, it is to be expected that a maximum of 50% if the methane will be consumed through its reforming with carbon dioxide. Therefore, as the micron sized material has consumed 47% of the methane supplied, its activity is very high.

The isothermal biogas reforming reaction profile for the nanosized nickel containing MFI zeolite at 900 °C is shown in Figure 5.7.

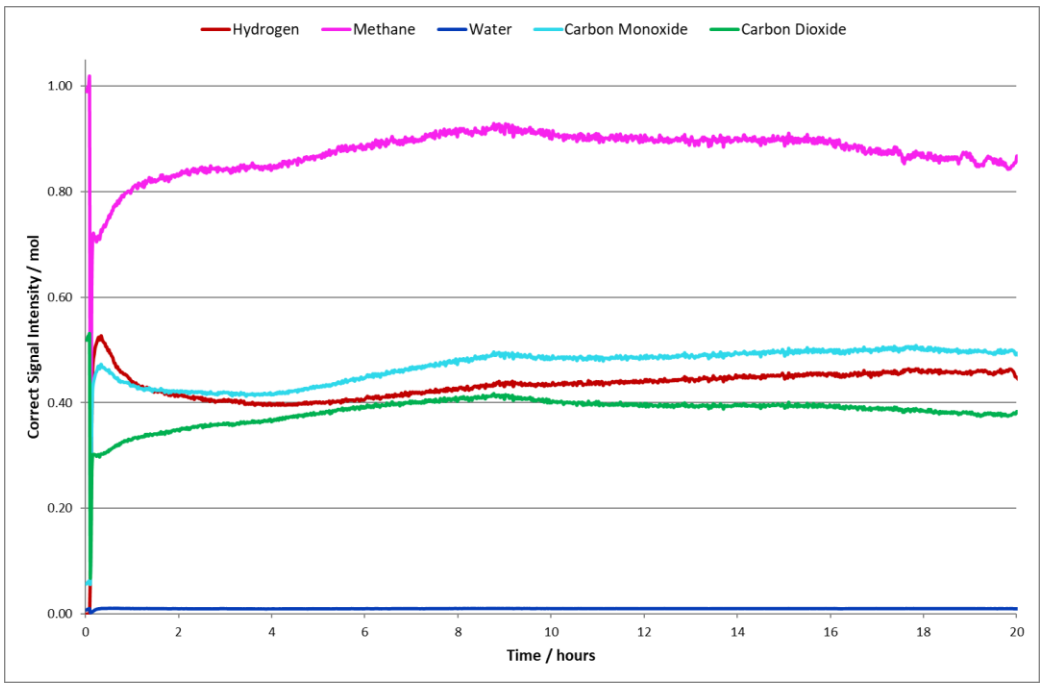

Figure 5.7. Isothermal biogas reforming over nano Ni MFI at 900 °C.

A significantly reduced activity for biogas reforming is seen for the nano sized material on comparison with its micron sized counterpart. A much smaller amount of methane, 13%, has been consumed with the use of the nanosized catalyst.

The temperature programmed oxidation experiment to yield the amount of carbon deposition was again carried out on both materials. These experiments yielded 0.0647 mg of observable carbon for the micron sized material, which is equal to 1.16175 mg of carbon deposited per gram of catalyst used, and 0.0454 mg of observable carbon for the nano sized material, which is equal to 1.135 mg of carbon deposited per gram of catalyst used. As approximately 40 mg of each catalyst material was used, and the amount of observable carbon measured on the nano catalyst was lower than that of the highly active micron sized material, it is unlikely that the lack of activity shown by the nano material is due to deactivation through carbon deposition.

5.3.3 Biogas reforming conclusions

The Biogas reforming over the nickel doped nanosized and micron sized material was carried out. For the temperature programmed reactions, the materials showed a similar activity towards the reforming, with both evolving approximately 0.80 mol of product. However, for the isothermal reforming reactions at 900 °C the micron sized nickel containing MFI type zeolite show a significantly higher activity towards the reforming of biogas than the nanosized MFI material. This is in disagreement with the theory that the nanosized material would show a higher level of activity as a result from its smaller particle size. This difference could be due to the micron sized material having more nickel sites than the nano sized material.

5.4 Partial Oxidation

The partial oxidation of methane is another technique used in the formation of synthesis gas. One of the main disadvantages to this method is that the balance between the partial oxidation (POx) and the total oxidation (TOx) of methane is a difficult to find.

5.4.1 Temperature programmed partial oxidation of methane

The partial oxidation of methane reaction profiles for the micron and nano sized MFI materials are shown in Figure 5.8 and 5.9 respectively.

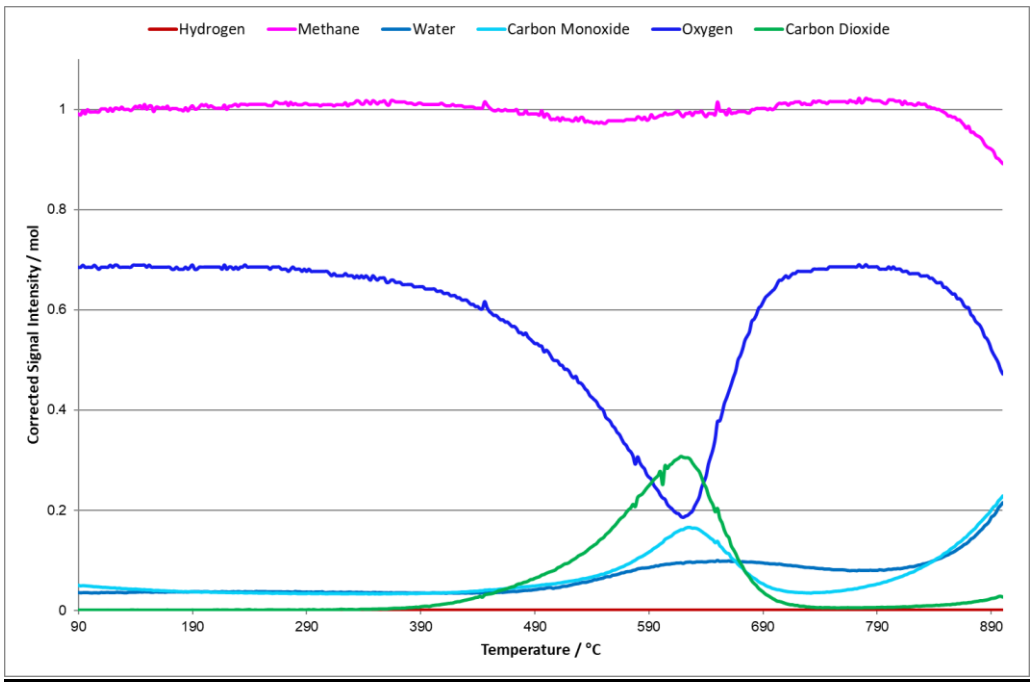

Figure 5.8. Temperature programmed POx forward reaction for micro Ni MFI.

The micron sized material shows catalytic activity between approximately 400 °C and 700 °C. This activity yields the species carbon dioxide, water and carbon monoxide. As the latter is formed via partial oxidation this could be an indication that POx activity is present, however, as no hydrogen is yielded alongside it, this is unlikely to be the case. The presence of carbon dioxide and water indicate that the activity is that of TOx. The formation of the CO is most likely due to the reaction between the methane and the oxygen, giving water and carbon monoxide.

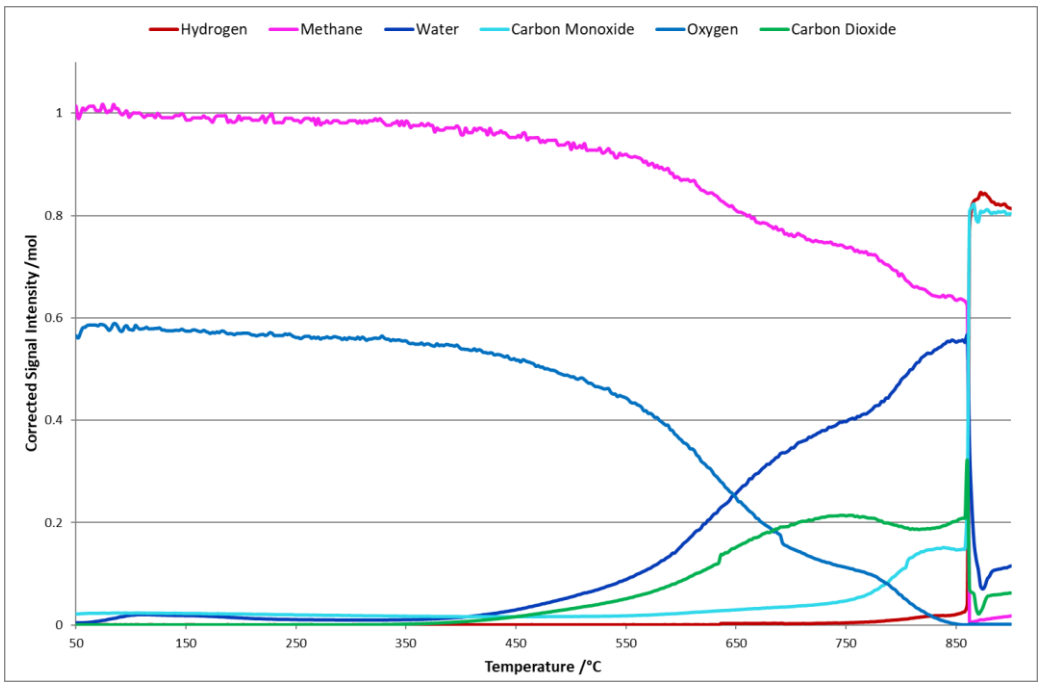

Figure 5.9. Temperature programmed POx forward reaction for nano Ni MFI.

The forward reaction for the partial oxidation of methane over the nanosized material shows vastly different reaction profile. From approximately 350 °C to 860 °C the catalytic activity present is that of total oxidation, with a small amount of reverse water gas shift. However, at 860 °C there is an abrupt change to from TOx to POx, with almost all the methane being consumed, with an 80% conversion to hydrogen. Some low level total oxidation remains producing water and carbon dioxide but it is minimal in comparison to the POx activity.

The reverse reaction profiles for the partial oxidation of methane over the micron and nanosized MFI materials is shown in Figure 5.10 and 5.11 respectively.

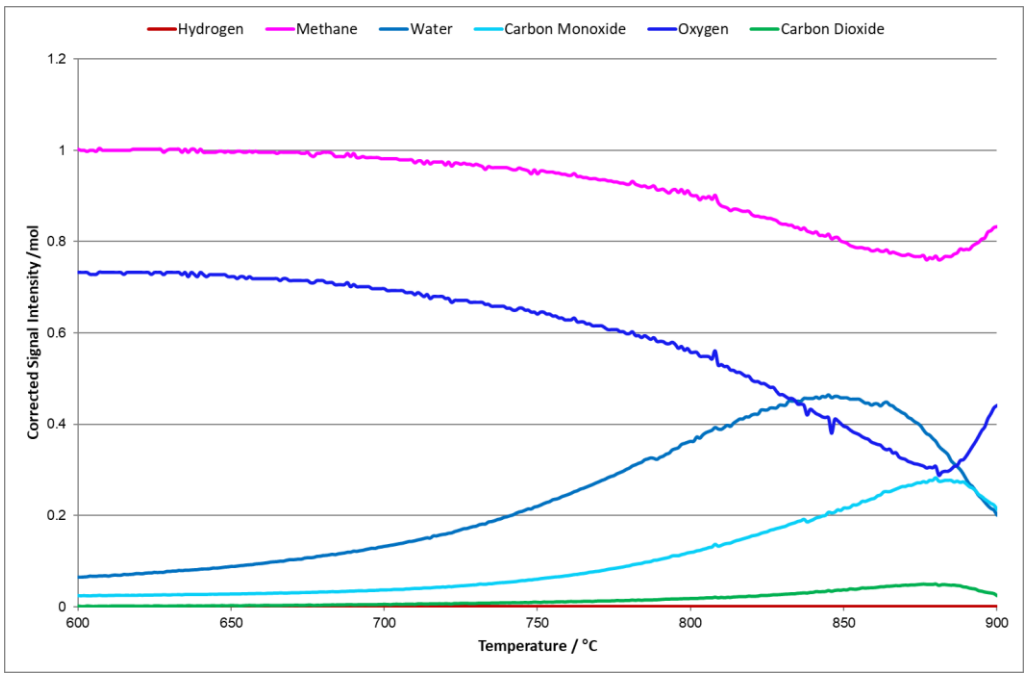

Figure 5.10. Temperature programmed POx reverse reaction for micro Ni MFI.

For the micron sized material, the total oxidation activity continues for the remainder of the experiment down to 600 °C, at no point is any POx activity present.

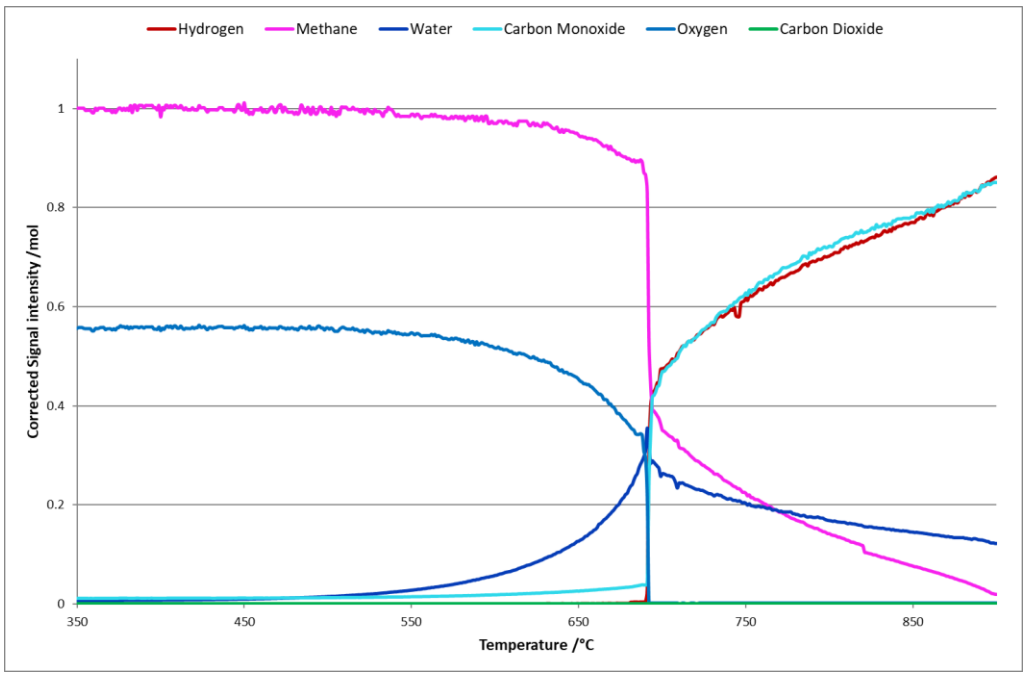

Figure 5.11. Temperature programmed POx reverse reaction for nano Ni MFI.

The reaction profile for the nano sized material however, shows POx activity down to 690 °C, albeit decreases in activity as the temperature decreases. During this cooling period between 900 °C and 690 °C all of the oxygen in the mixture is being consumed. The TOx activity present slowly increases as the temperature and POx activity decrease, at 690 °C all total oxidation activity decreases as the temperature decreases. As the methane undergoes total oxidation, there is a selectivity towards the formation of water over the formation of carbon dioxide.

The temperature programmed oxidation experiments to determine the carbon deposition on the catalysts were carried out and yielded, 0.28 mg of observable carbon for the micron sized material, which is equal to 7 mg of carbon deposited per gram of catalyst, and 0 mg of observable carbon for the nanosized material. The deposition of the carbon on the micron MFI surface is likely due to the combination of the Boudouard reaction and the thermal decomposition of methane at elevated temperatures. The lack of observable carbon for the nano MFI material does not prove that there is no carbon deposition it simply means that the amount of carbon present is below the detection limit of the instrument.

5.4.2 Isothermal partial oxidation of methane

The isothermal reaction profile of the partial oxidation of methane at 900 °C over the nickel containing micron sized MFI zeolite catalyst is shown in Figure 5.12.

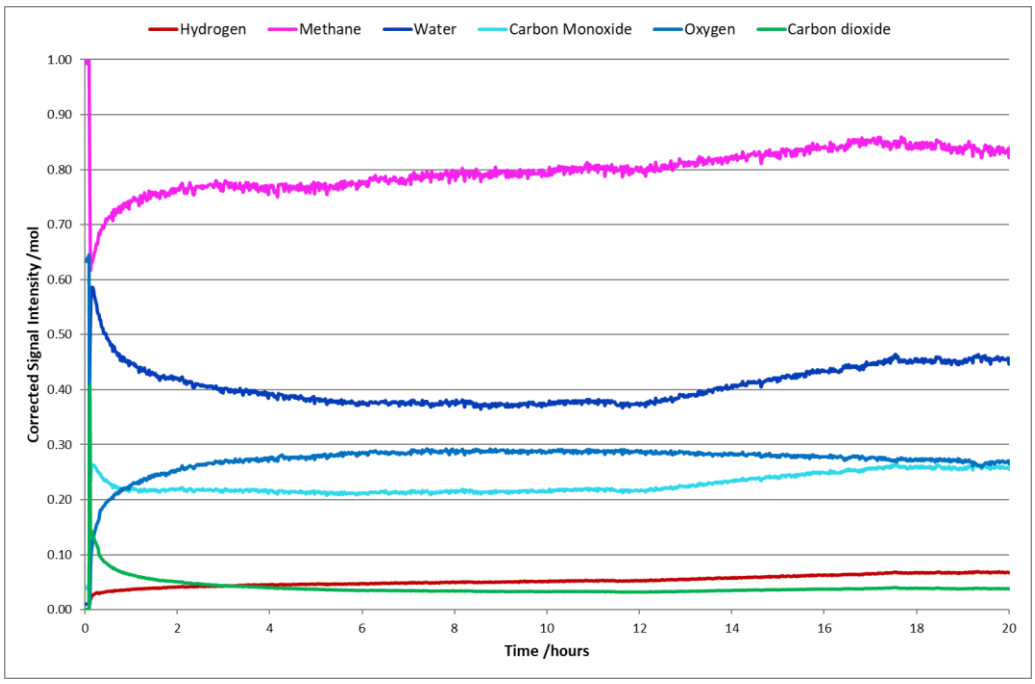

Figure 5.12. Isothermal POx reaction over micro Ni MFI at 900 °C.

The micron sized material shows very little POx activity during the 20 hour isothermal experiment, with some hydrogen produced, however, this could be a result of the forward water gas shift reaction. Total oxidation activity is present throughout the experiment, however, this activity only consumed 16% of the methane present in the mixture after 20 hours.

The isothermal reaction profile for the partial oxidation of methane at 900 °C over the nickel containing nano sized MFI zeolite catalyst is shown in Figure 5.13.

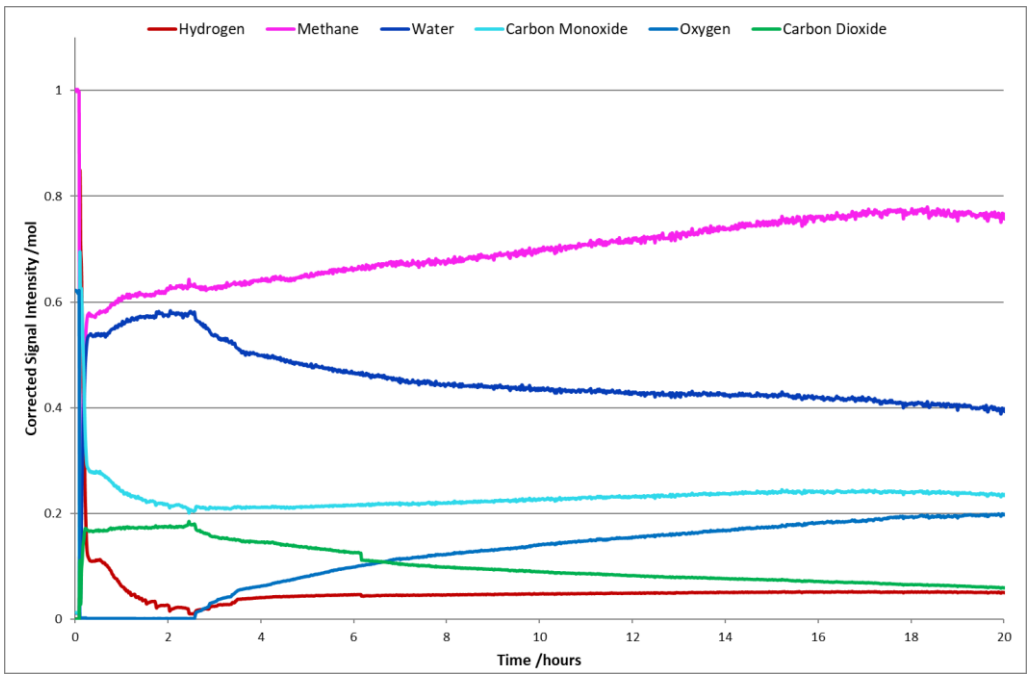

Figure 5.13. Isothermal POx reaction over nano Ni MFI at 900 °C.

In contrast to its activity during the temperature controlled reaction above, the nano sized material shows little POx activity, however there could be a low level activity as a small amount of hydrogen is formed. Total oxidation is occuring for throughout the 20-hour experiment, after 20 hours 23% the methane has been consumed by the TOx activity. Again the total oxidation activity shows a selectivity for the formation of water over carbon dioxide. As the hydrogen level is so low and the evolved water trace shows a mirror of the hydrogen trace it was thought that the hydrogen was also being oxidised along with the methane to produce water, this was further investigated in Chapter 5.5.

The temperature controlled oxidation reactions were carried out for both materials to yield the carbon deposition. For the micron sized material, the amount of observable carbon was found to be 0.0515 mg, which is equal to 1.2875 mg of carbon deposited per gram of catalyst used, and for the nano sized material it was determined that 0.040 mg of observable carbon was present on the surface, which equal 1 mg of carbon deposited per gram of catalyst used. These are relatively low amounts of observable carbon indicating that the thermal decomposition of methane and the Boudouard reaction were not present to any great extent,

5.4.3 Partial oxidation conclusions

The partial oxidation of methane over the nickel doped micron sized and nano sized MFI material was carried out. The temperature programmed reactions showed that the nano sized material is better suited to partial oxidation than its micron sized counterpart, with the micron sized material showing little hydrogen evolution. However, for the isothermal partial oxidation experiment at 900 °C, the activity of the nanosized material did not reflect that shown for the temperature programmed experiment, with the material showing an oxidative preference for the evolved hydrogen over the methane. The higher level of activity shown by the nano sized material is in agreement with the theory that the reduction in particle size results in more efficient catalysis.

5.5 The oxidation of synthesis gas over the nanosized material

Due to the selectivity shown by the nickel containing nanosized MFI zeolite towards the total oxidation of methane to water, it was theorised that it would show the same selectivity towards the hydrogen formed. The isothermal POx experiment conducted over the nanosized catalyst showed a mirroring of the hydrogen and water signal indicating that the hydrogen was also being oxidised to water. To test this theory an oxidation of synthesis gas experiment was setup to investigate whether the oxidation of hydrogen can be seen. These experiments were conducted as per the description in Chapter 2.5.3.

5.5.1 Temperature programmed oxidation of syn-gas

The reaction profile of the temperature controlled oxidation of syn-gas over the nano nickel containing material is shown in Figures 5.14 and 5.15.

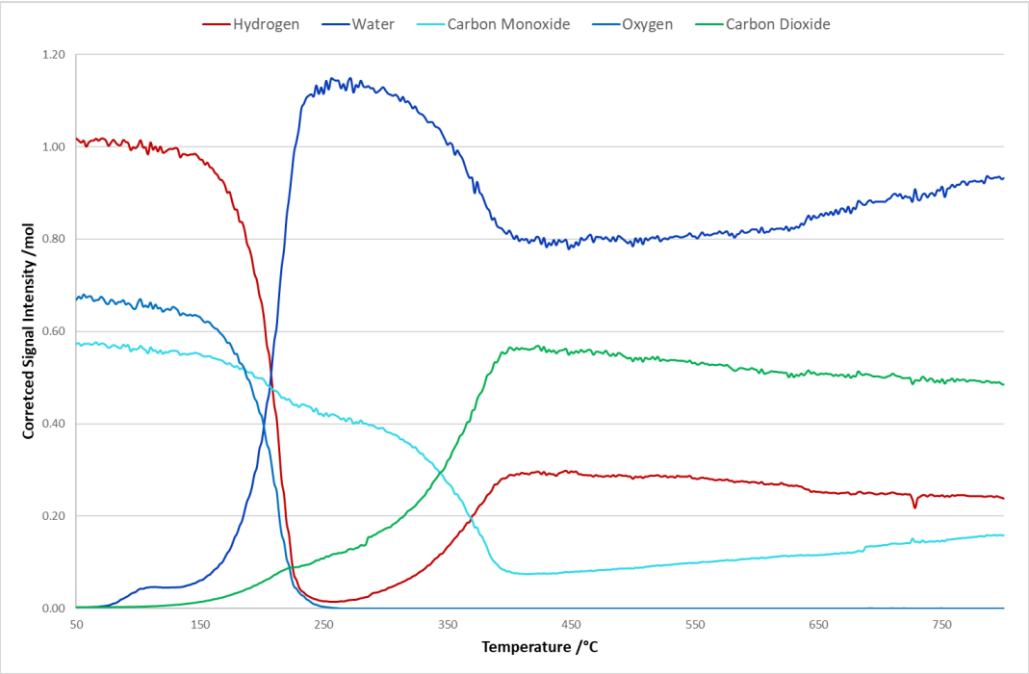

Figure 5.14. Temperature programmed forward syn-gas oxidation over nano Ni MFI.

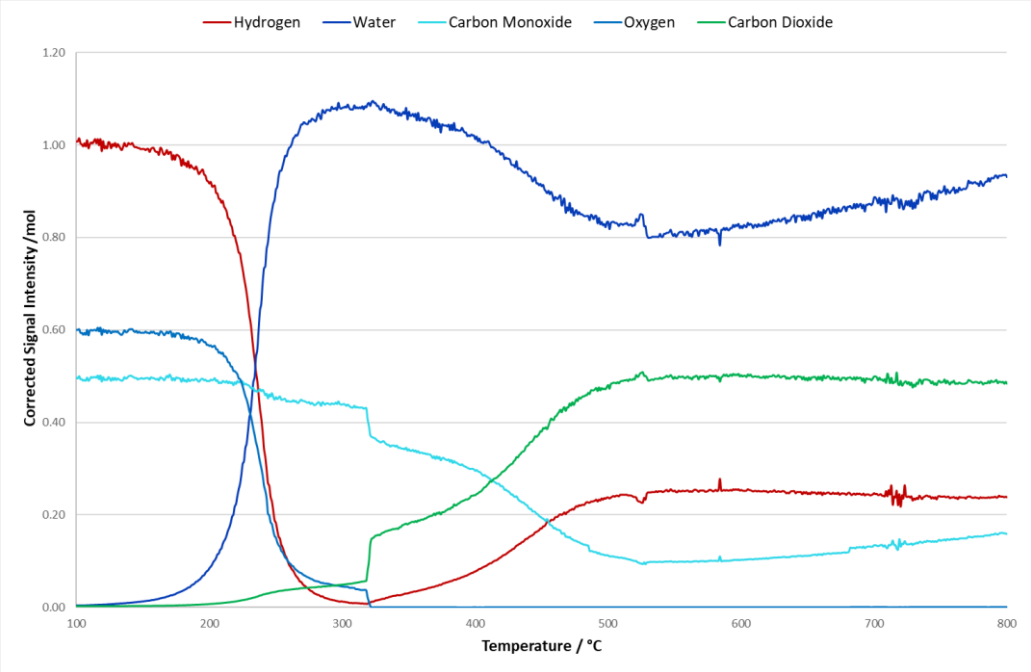

Figure 5.15. Temperature programmed reverse syn-gas oxidation over nano Ni MFI.

From very low temperatures the selectivity towards hydrogen oxidation over carbon monoxide oxidation can be seen. The small evolution of water seen at 100 °C can be

attributed to the removal of the occluded water from within the MFI channel system. A large amount of water then follows, at a low temperature of 150 °C, a product of the oxidation of hydrogen which continues up to 800 °C. The oxidation of the carbon monoxide follows shortly after the hydrogen oxidation. On cooling, the production of the carbon dioxide ceases before the water production, further indicating that the preference of the material to oxidise hydrogen.

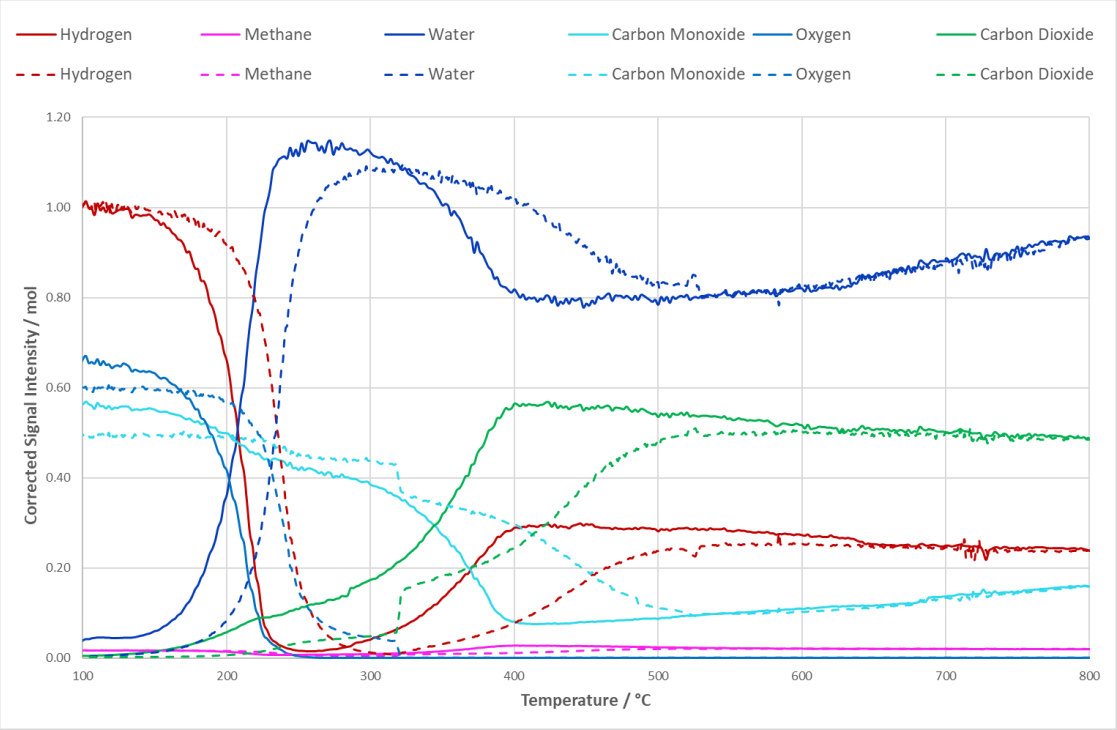

Figure 5.16. Temperature programmed forward (full-line) and reverse (dashed line) syn-gas oxidation over nano Ni MFI.

The hysteresis between the forward and the reverse reactions can clearly be see in Figure 5.16. The reverse reaction (dashed) is slightly shifted to a higher temperature, showing a smaller average shift at lower temperatures of approximately 50 °C, increasing to approximately 100 °C at higher temperature. The higher difference in temperature between the forward and reverse reaction is expected due to the constraints of the temperature regulation system.

The temperature programmed oxidation reaction to determine the carbon deposition on the surface of the nanosized material yielded 0.0535 mg of observable carbon, which is equal to 1.3375 mg of carbon deposited per 1 g of catalyst used. As there is no methane to undergo thermal decomposition the most likely source of carbon deposition is the Boudouard reaction.

5.5.2 Isothermal oxidation of syn-gas

As the temperature programmed reaction of the syn-gas oxidation above showed catalytic activity at a low temperature, an isothermal reaction was carried out to investigate if this low temperature activity is maintained over 20 hours.

From the temperature programmed reaction above shows water evolution from 150 °C, it was decided to carried out an isothermal oxidation of syn-gas at that temperature, the reaction profile for which is shown in 5.17.

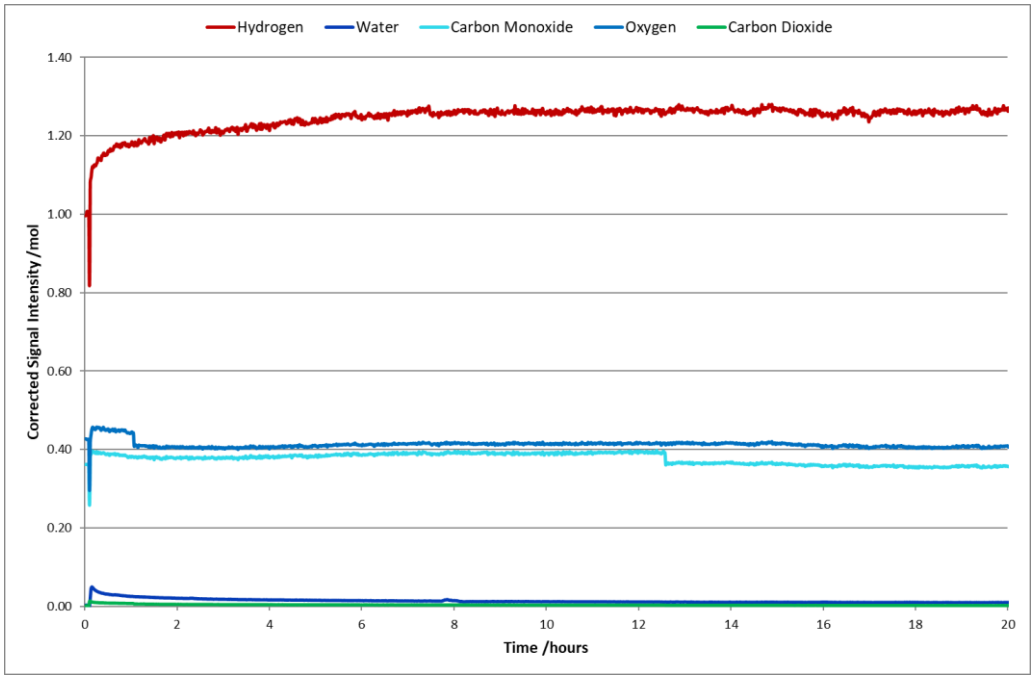

Figure 5.17. Isothermal syn-gas oxidation over nano Ni MFI at 150 °C.

The isothermal oxidation of syn-gas over the nano nickel containing zeolite catalyst shows no activity towards either the oxidation of hydrogen or carbon dioxide. This lack of activity is sustained over the 20-hour experiment.

It was then decided to increase the temperature to 200 °C. During the temperature programmed reaction in Chapter 5.5.1, at 200 °C the hydrogen evolution was increasing, it was therefore thought that the isothermal reaction at this temperature would show more activity than at 150 °C. The reaction profile for the isothermal oxidation of syn-gas at 200 °C is shown in Figure 5.18.

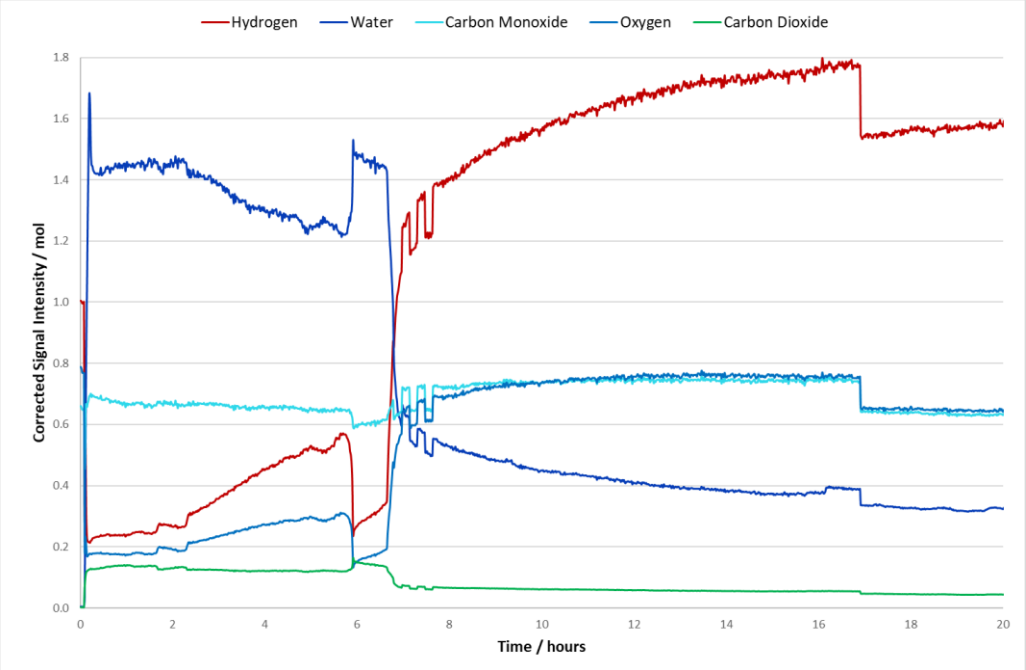

Figure 5.18. Isothermal syn-gas oxidation over nano Ni MFI at 200 °C.

The profile for the isothermal reaction at 200 °C shows a relatively stable oxidation activity for the first 2.5 hours which slowly starts to diminish over time. After approximately 6 hours there is a spike in oxidation activity before it decreases again. This spike in activity could be due to the ‘cleaning’ of the catalyst surface, allowing the sudden switch to a reactive regime. At 6.5 hours, the oxidation activity falls significantly, however, t he selectivity towards the oxidation of hydrogen over carbon monoxide is still present.

As an increase in temperature of 50 °C from 150 °C to 200 °C, had a significant impact on the catalysis another increase of 50 °C was investigated.

The isothermal oxidation of syn-gas reaction profile at 250 °C is shown in Figure 5.19.

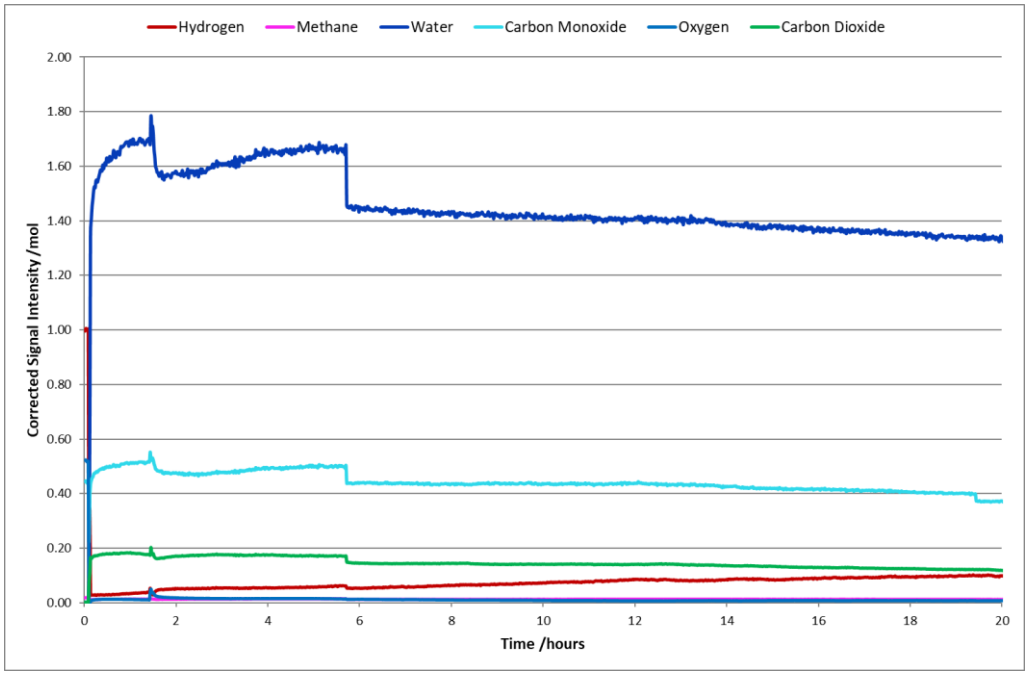

Figure 5.19. Isothermal syn-gas oxidation over nano Ni MFI at 250 °C.

The reaction profile at 250 °C shows a high level of oxidation activity, where the vast majority of the hydrogen is oxidised to water. The selectivity towards the hydrogen oxidation is still present, with a low level of carbon monoxide oxidation taking place. The oxidation activity slowly diminishes over time but is still high in comparison to that shown at the lower temperatures.

The isothermal oxidation of syn-gas reaction profile at 300 °C is shown in Figure 5.20.

The reaction profile for the oxidation of syn-gas at 300 °C is very similar to that at 250 °C. The selectivity towards hydrogen oxidation is present with a much lower oxidation activity towards the carbon monoxide. As with the 250 °C isothermal reaction the activity diminishes over time, however there is still a relatively high level of hydrogen oxidation occurring after 20 hours.

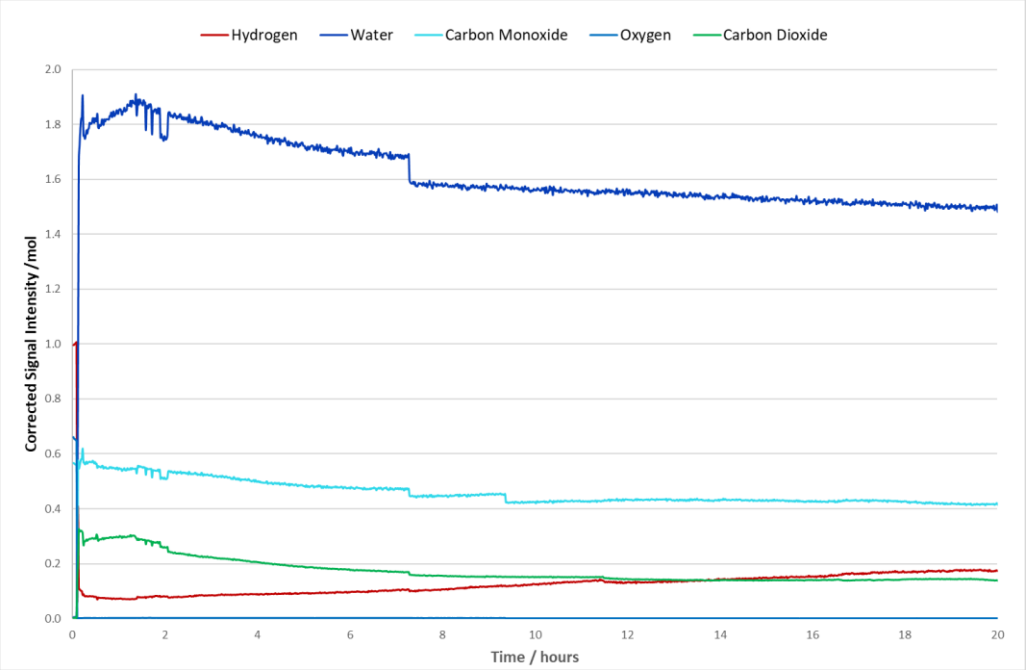

Figure 5.20. Isothermal syn-gas oxidation over nano Ni MFI at 300 °C.

The temperature programmed oxidation reactions to determine the level of carbon deposition were carried out after all the discussed isothermal reactions. The amounts of observable carbon obtained are shown in Table 5.1.

Table 5.1. Mass of carbon deposition for the isothermal oxidation of syn-gas reactions.

Temperature of reaction / °C	Mass of observable carbon / mg	Mass of carbon per gram of catalyst / mg
150	0.000508	0.0127
200	0.00688	0.172
250	0	0
300	0	0

As expected the carbon deposition at the low temperature reactions is very low, due to the lack of thermal decomposition, with the 250 and 300 °C reactions yielding no observable carbon above the detection limit of the instrumentation.

5.5.3 Syn-gas oxidation conclusions

The oxidation of syn-gas was carried out over the nickel containing nanosized MFI type zeolite. The temperature programmed reaction showed the preferential oxidation of the hydrogen over the carbon monoxide beginning at low temperatures of approximately 150 °C. The isothermal reaction was carried out a variety of temperatures to ascertain the effect of temperature on the selectivity and overall activity. The 150 °C isothermal syn-gas oxidation showed little oxidative activity, whereas the oxidation at 200 °C showed a hydrogen selective oxidative activity for approximately 6.5 hours, after which the activity severely diminished. This sudden change in activity could be due to the deactivation of the catalyst through carbon deposition, or the oxidation of the catalyst itself. The isothermal reactions at 250 °C and 300 °C both show a high activity for the preferential oxidation of hydrogen from the synthesis gas mixture.

From these results it is clear that the nickel containing nanosized MFI zeolite is active for the low temperature oxidation of syn-gas, in which there is a selectivity towards the oxidation of the hydrogen over the carbon monoxide.

5.6 Conclusions

Two nickel doped zeolites with the MFI framework were synthesised, the clear solution method was used to yield a nano sized material and the hydrothermal method was used to yield a micron sized material. The catalytic testing for the nano- and micron- sized materials was carried out to allow the understanding of effect of the change in particle size on the catalytic activity. This study has shown that the nickel containing nano sized MFI zeolite has

a higher activity for the partial oxidation of methane over the its micron sized counterpart, in agreement with the theory that the reduction in particle size leads to the improve in catalytic efficiency. However, the biogas reforming investigations concluded that the micron sized material is a better catalyst, showing a much high activity for the reforming than the nanosized material. This is in disagreement with the proposed theory of the improvements to be gained from the reduction in particle size. The micron sized material showing a higher activity over the nano sized material could be due to the availability of the nickel sites, with there being more present in the micron sized zeolite. The difference in activity in comparison with proposed theory could also be due the fact the gases used for testing are small gases, therefore the diffusion limitations will be small regardless of the material size.

During the partial oxidation studies the nano sized material showed an oxidation selectivity towards a product of that reaction, hydrogen. This oxidative selectivity was investigated via the oxidation of synthesis gas where the nano sized catalyst showed an overwhelming selectivity towards hydrogen oxidation over carbon monoxide oxidation. This oxidation is able to occur at low temperatures from 200 °C with the catalysis remaining at a high level for the hydrogen oxidation for at least up to 20 hours.

From these results it can be concluded that the optimum zeolite particle size for the reforming of methane with either carbon dioxide or oxygen different methods lies somewhere between the nano and micron sized materials tested in this study. It would be difficult to obtain such a material in a controlled and reproducible manner, and as such is an area where the study could be expanded.

5.7 References

1. Frontera P, Macario A, Aloise A, Crea F, Antonucci P, Nagy J *et al*. Catalytic Dry-Reforming on Ni–Zeolite Supported Catalyst. Catal Today. 2012;179(1):52-60.

2. Frontera P, Macario A, Aloise A, Antonucci P, Giordano G, Nagy J. Effect of Support Surface on Methane Dry-Reforming Catalyst Preparation. Catal Today. 2013;218-219:18-29.

3. International Zeolite Association. Database of Zeolite Structures [Internet]. 2015. Available from: http://www.iza-structure.org/databases/

6.0 MEL and MTW Type Zeolite Catalysis of Reforming Reactions

6.1 Introduction

To gain a further insight into Ni-doped zeolite catalysis and to improve efficiency, it is important to explore every 'avenue'. In the case of zeolites there are a wide range of framework types that have not been studied for their methane reforming capabilities, studies have focused on the MFI type zeolite[1,2]. It was therefore decided to investigate zeolite framework types not too dissimilar to the MFI-type studied in Chapter 5. MEL and MTW were chosen for a number of reasons. Firstly, they are five-ring zeolites like MFI and are therefore formed in a similar way. MFI, MEL and MTW are all common intergrowths of each other meaning that they are able to form under the same conditions. These zeolite types were also chosen as their syntheses are well documented and therefore should be relatively unproblematic to synthesise.

6.1.1 MEL type zeolite

The MEL framework type was first reported in 1973 by the Mobil Oil company[3], the same company that reported the MFI framework ZSM-5[4]. This MEL framework material was denoted Zeolite Socony Mobil-11 (ZSM-11). One year later, Bibby *et al*[6]. reported the all-silica analogue of the material, Silicalite-2.

As a commonly found intergrowth with the MFI material, it is no surprise that the MEL framework type is also a part of the pentasil family of zeolites, with the characteristic five membered ring linkage.

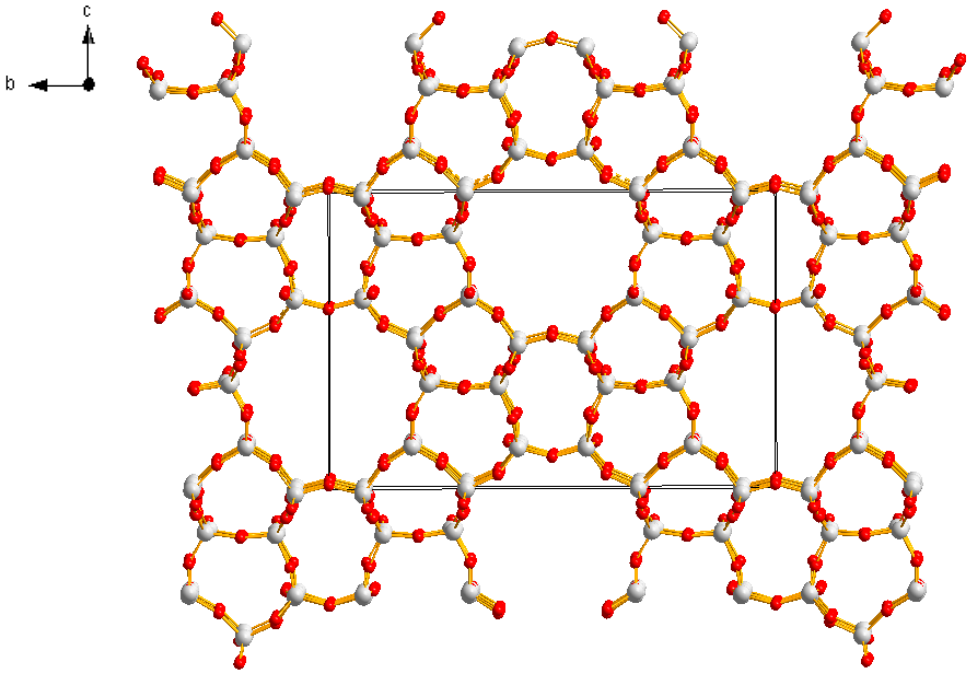

Figure 6.1. Framework structure of MEL[6], where red atoms are oxygen and white atoms are silicon.

At room temperature, the MEL material has a tetragonal framework symmetry with a space group I-4m2 and cell parameters a = 20.27 Å, b = 20.27 Å, c = 13.56 Å and α = β = γ = 90 °. The MEL framework has a dual channel system with each channel being perpendicular to the other. The pores within the framework have a 10 ring opening, where the straight channel is parallel to the (100) plane[6]. The occupiable volume of an idealized framework is 701.92 Å^3, which is 12.69 % of the framework model[6].

6.1.2 MTW type zeolite

The MTW framework was first reported in 1981 by Hickson[7] and denoted CSH-5. Many other materials with the MTW framework have also been reported including NU-13[8], TPZ-12[9], Theta-3[10] and ZSM-12[11], the latter being another of the Mobil Oil company patented materials. The main difference between these listed materials is their silica to alumina ratio and the method in which they are synthesised.

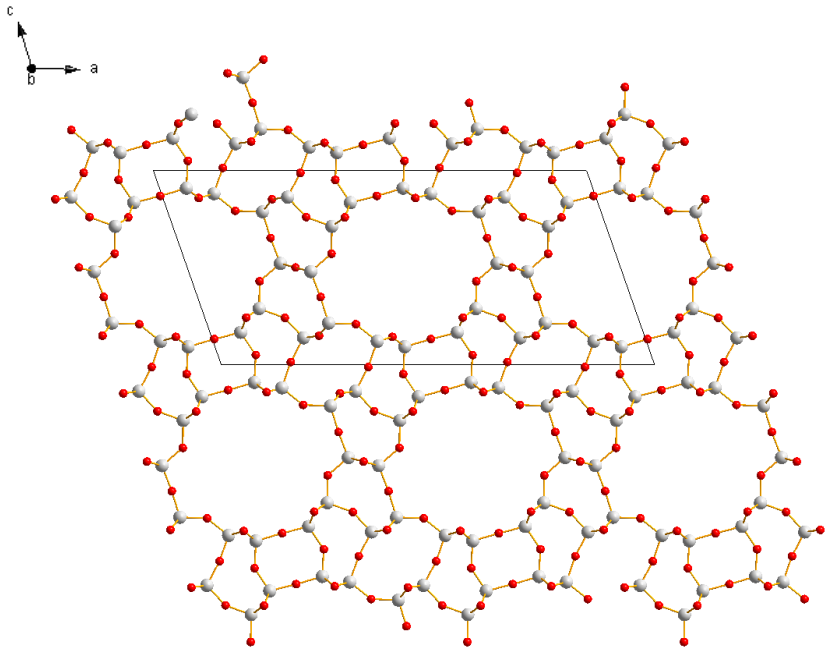

Figure 6.2. Framework structure of MTW[6], where red atoms are oxygen and white atoms are silicon.

At room temperature, the MTW material has a monoclinic framework symmetry with a *C2/m* space group and cell parameters a = 25.55 Å, b = 5.26 Å, c = 12.12 Å and α = γ = 90 ° and β = 109.312 °. The MTW framework has a single channel system. The pores within the framework have a ten ring opening, where the straight channel is parallel to the (010) plane[6]. The occupiable volume of an idealized framework is 146.61 $Å^3$, which is 9.55 % of the framework model[6].

6.2 Synthesis of Ni-MEL catalyst

The nickel containing MEL zeolite was synthesised via the hydrothermal method as described in Chapter 2.2. The presence of the MEL framework was confirmed by X-ray

diffraction analysis, shown in Figure 6.3. The simulated powder pattern for the MEL framework from the IZA database was used a comparison.

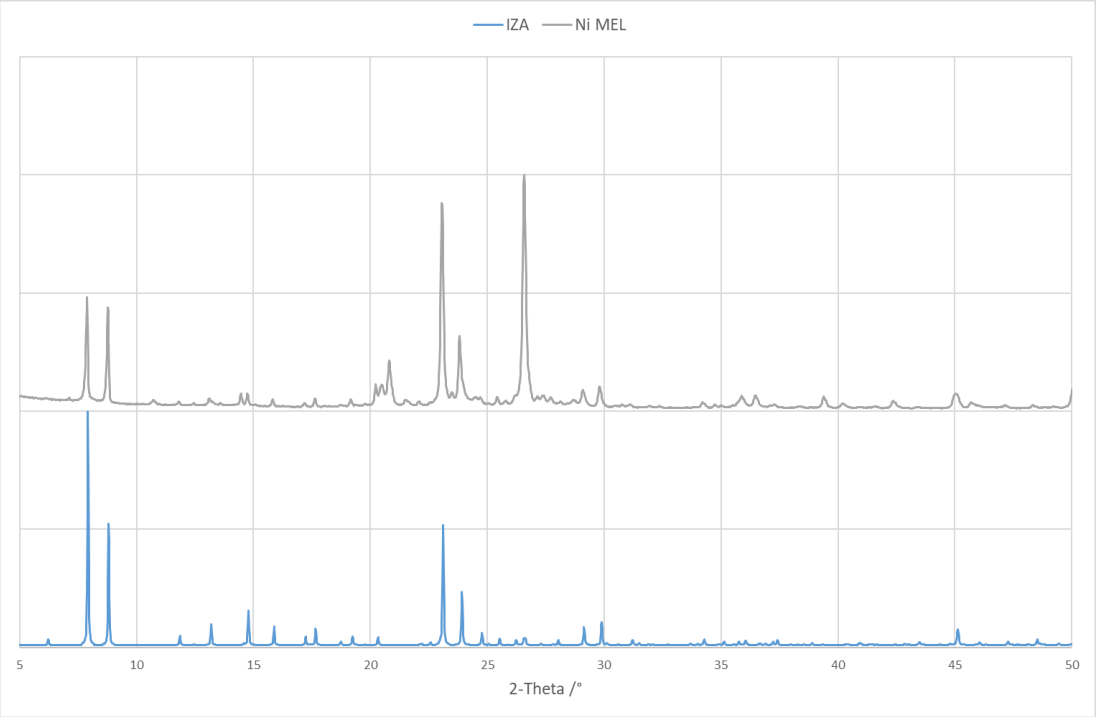

Figure 6.3. Powder pattern of the Ni MEL zeolite with the simulated IZA pattern[6].

6.3 Synthesis of Ni-MTW catalyst

The nickel containing MTW zeolite was synthesised via the hydrothermal method described in Chapter 2.3. The presence of the MTW framework was confirmed via X-ray diffraction analysis, shown in Figure 6.4. The simulated powder pattern for the MTW framework from the IZA database[6] was used a comparison.

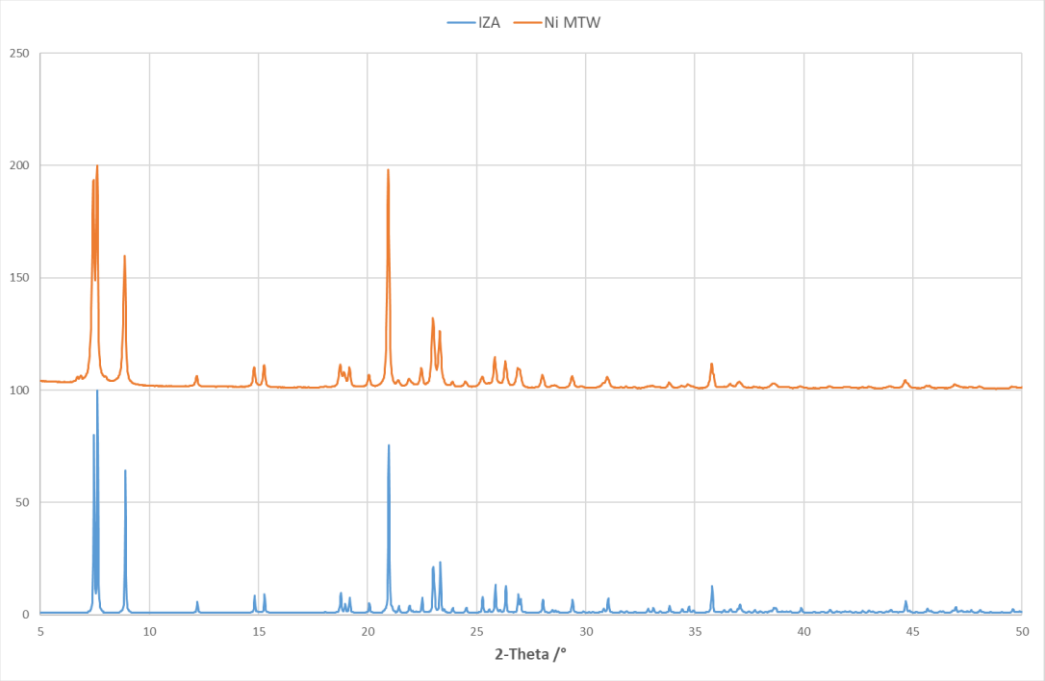

Figure 6.4. Powder pattern of the Ni MTW zeolite with the simulated IZA pattern[6].

In addition to the X-ray analysis, an interesting crystal morphology for the MTW type materials was observed via microscopy, shown in Figure 6.5. The crystal formed from these syntheses appear to have a star like shape to them, shown previously by Wang *et al*[12], which is most likely occurring from a single nucleation point with multiple crystals stacking on top on one another. This shape could be reproduced via the same hydrothermal method for a reaction length of both 14 and 23 days.

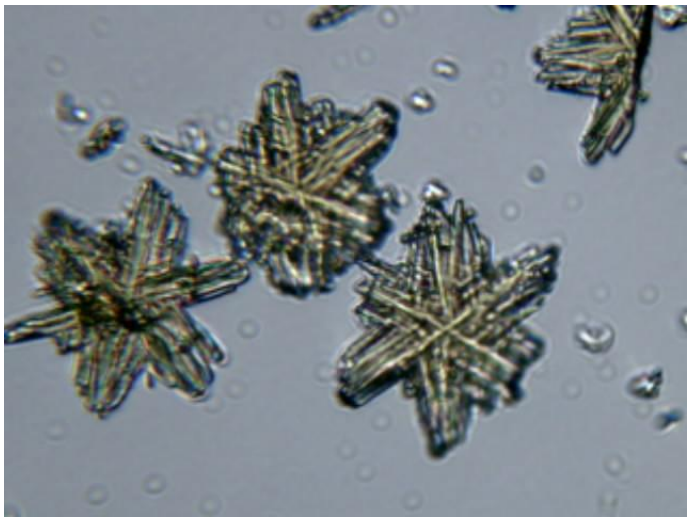

Figure 6.5. Microscopy images of the MTW crystal morphology.

6.4 Dry reforming

The catalysis of the dry reforming of methane was investigated via the method described in Chapter 3.4.3. Both the temperature programmed and isothermal dry reforming reactions were carried out.

6.4.1 Temperature programmed dry reforming

The results from the forward temperature programmed dry reforming reactions for both the MEL and MTW type materials are shown in Figures 6.6. and 6.7 respectively.

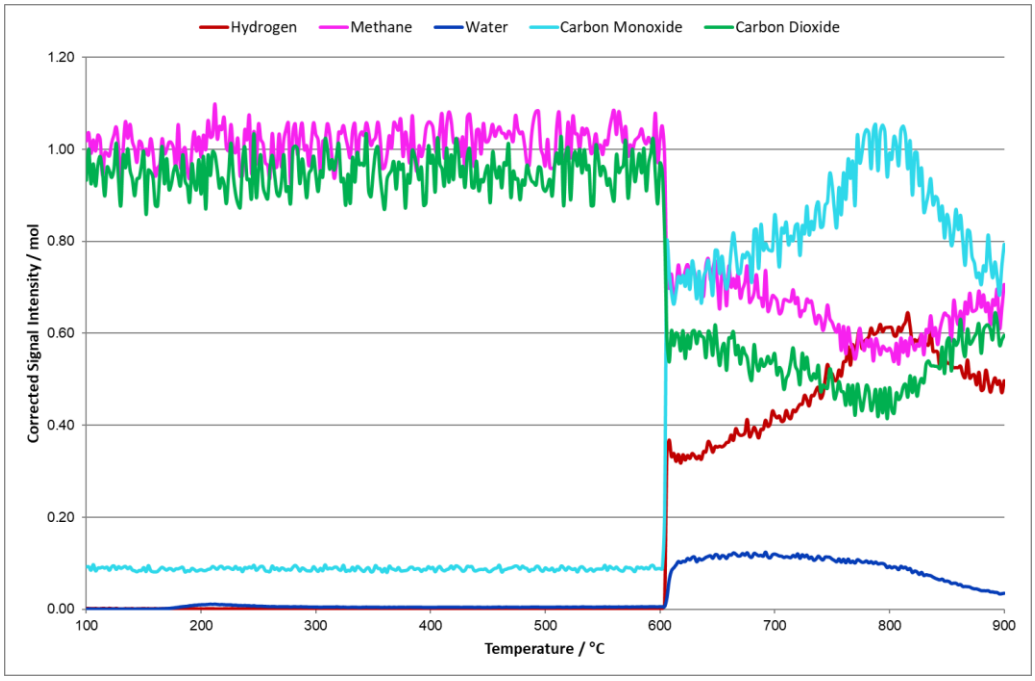

Figure 6.6. Temperature programmed dry reforming forward reaction over Ni MEL.

It can clearly be seen that for both materials, the start of the reforming is very sudden, at approximately 600 °C for MEL and 500 °C for MTW. The MTW material shows a stable increase in catalytic activity as the temperature increases and utilises a larger percentage of the methane present. The MEL material on the other hand, shows a much poorer performance which is not sustained as the temperature increases. The reverse water gas shift reaction is occurring in conjunction with the methane reforming for both the MEL and

MTW materials. When looking at the molar signal intensity it is clear that the MTW material is a much more effective catalyst than MEL.

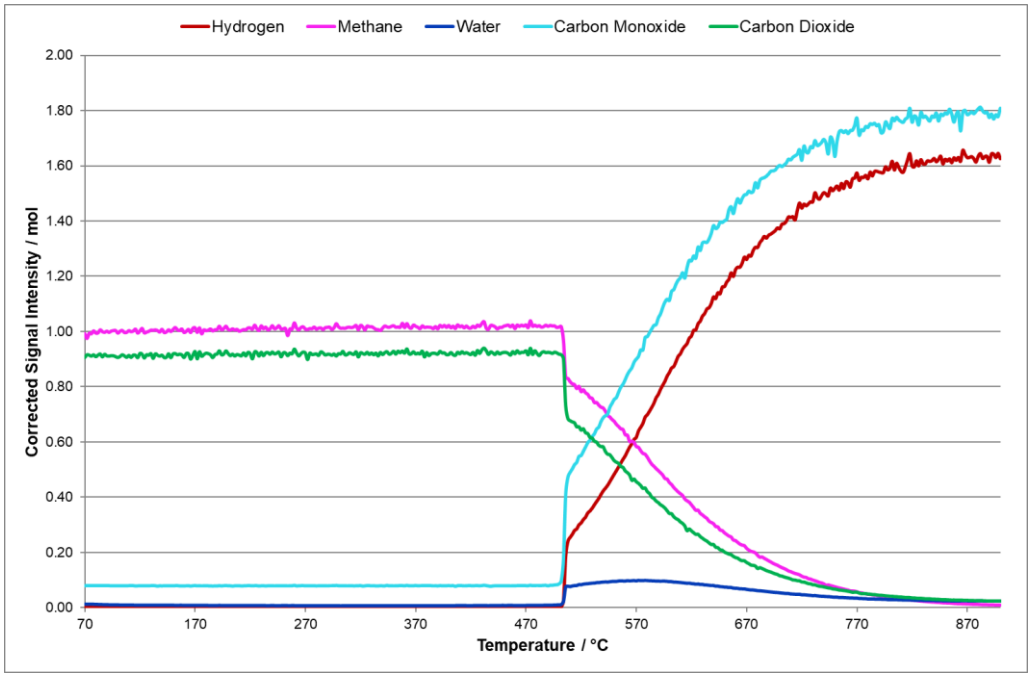

Figure 6.7. Temperature programmed dry reforming forward reaction over Ni MTW.

The reverse, cooling, dry reforming reaction for them MEL and MTW material are shown in Figure 6.8 and 6.9 respectively.

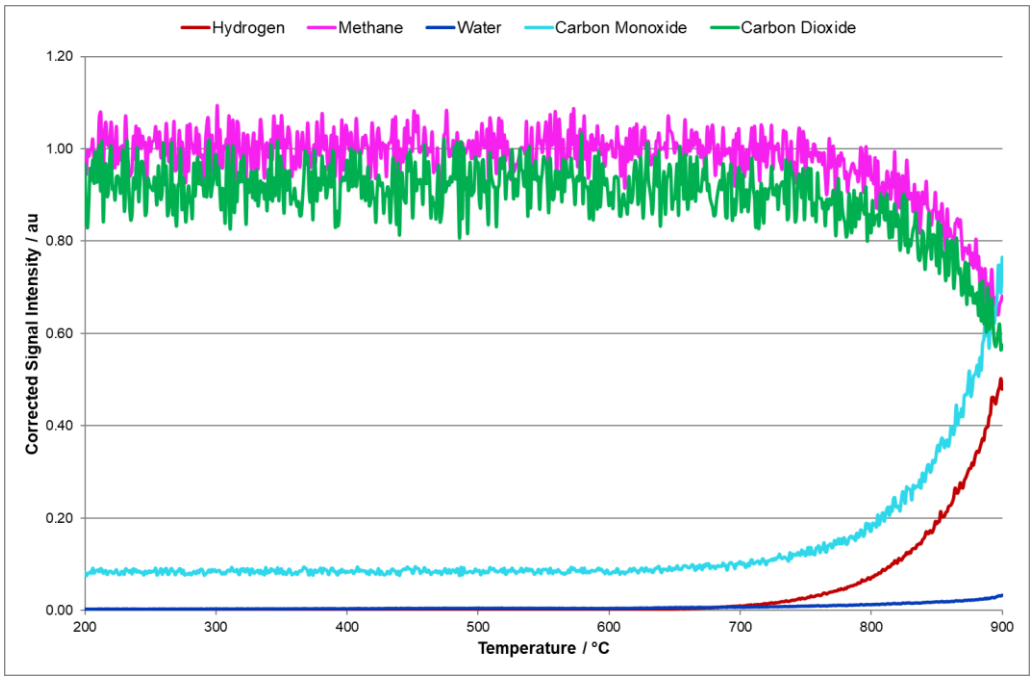

Figure 6.8. Temperature programmed dry reforming reverse reaction over Ni MEL.

The little activity shown by the MEL catalyst drops off very quickly for the reverse reaction, with no activity observed below 600 °C. The reverse reaction for the MTW material shows a steady decrease in activity, with a slight occurrence of the reverse water gas shift reaction. There is no catalytic activity observed after 350 °C.

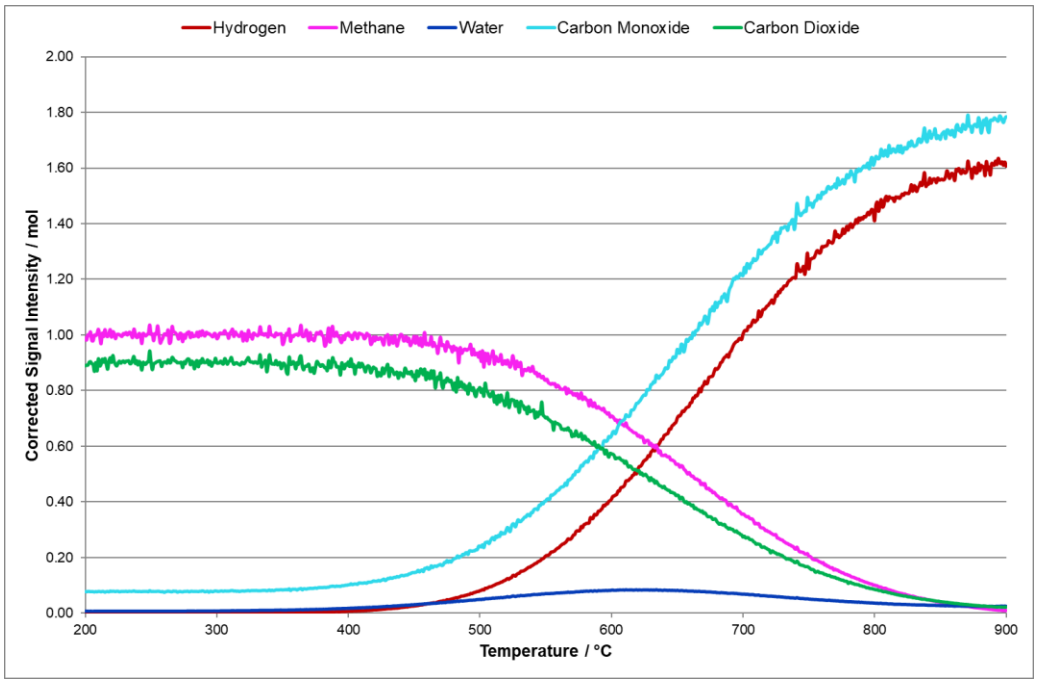

Figure 6.9. Temperature programmed dry reforming reverse reaction over Ni MTW.

For these reactions the amount of carbon deposition on the surface of the catalyst was measured using the oxidation reaction described in Chapter 3.4.4. For the MEL material the amount of observable carbon was 0.0677 mg, which is equal to 1.6925 mg of carbon deposited per gram of catalyst used, and for MTW it was 0.0574 mg, which is equal to 1.435 mg of carbon deposited per gram of catalyst used.

6.4.2 Isothermal dry reforming

The isothermal dry reforming reaction for MEL at 900 °C is shown in Figure 6.10. It is clear from the reaction trace that the nickel containing MEL material rapidly loses most of its activity within the first three hours. After which a low level activity is observed, along with the reverse water gas shift reaction.

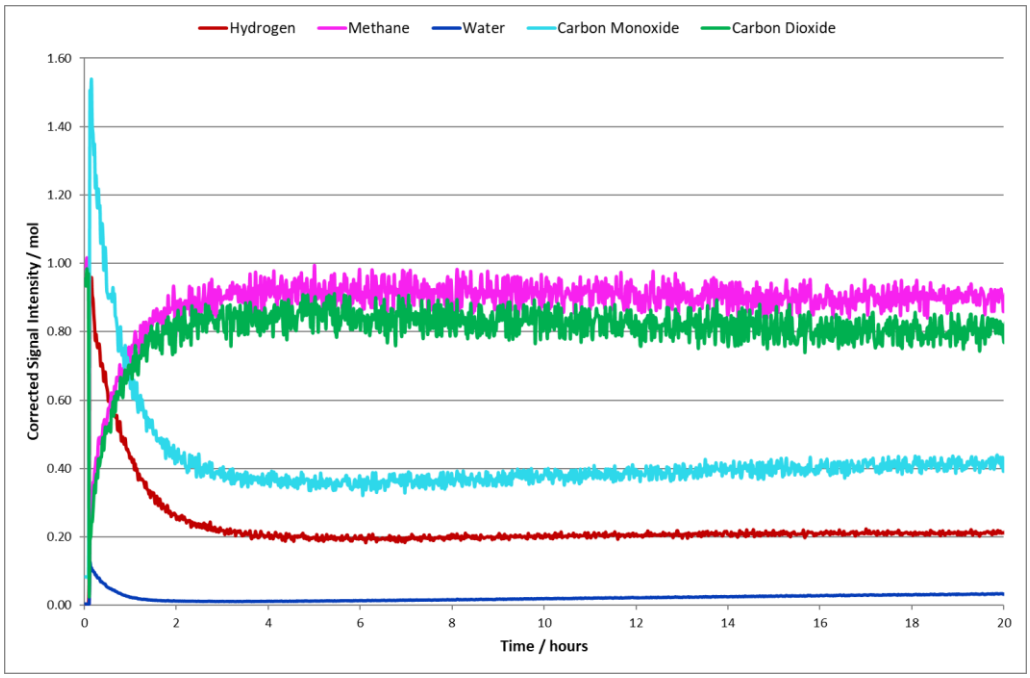

Figure 6.10. Isothermal dry reforming over Ni MEL at 900 °C.

The temperature programmed oxidation reaction to determine the amount of carbon deposition was carried out and yielded 0.0652 mg of observable carbon for the MEL material, which is equal to 1.63 mg of carbon deposited per gram of catalyst used.

The isothermal dry reforming of methane at 900 °C over the nickel containing MTW material is shown in Figure 6.11.

In comparison with Figure 6.10, the activity for the MTW material is much higher than that for MEL. It can be seen that the activity is decreasing over time for the MTW material but a relatively high activity, when compared to the MEL material, is maintained up until the end of the study at 20 hours. Again a small amount of the water gas shift reaction is

occurring, which steadily increases as the activity of the catalyst decreases. The temperature programmed oxidation reaction to determine the amount of carbon deposition was carried out and yielded 0.056 mg of observable carbon for the MTW material, which is equal to 1.4 mg of carbon deposited per gram of catalyst used.

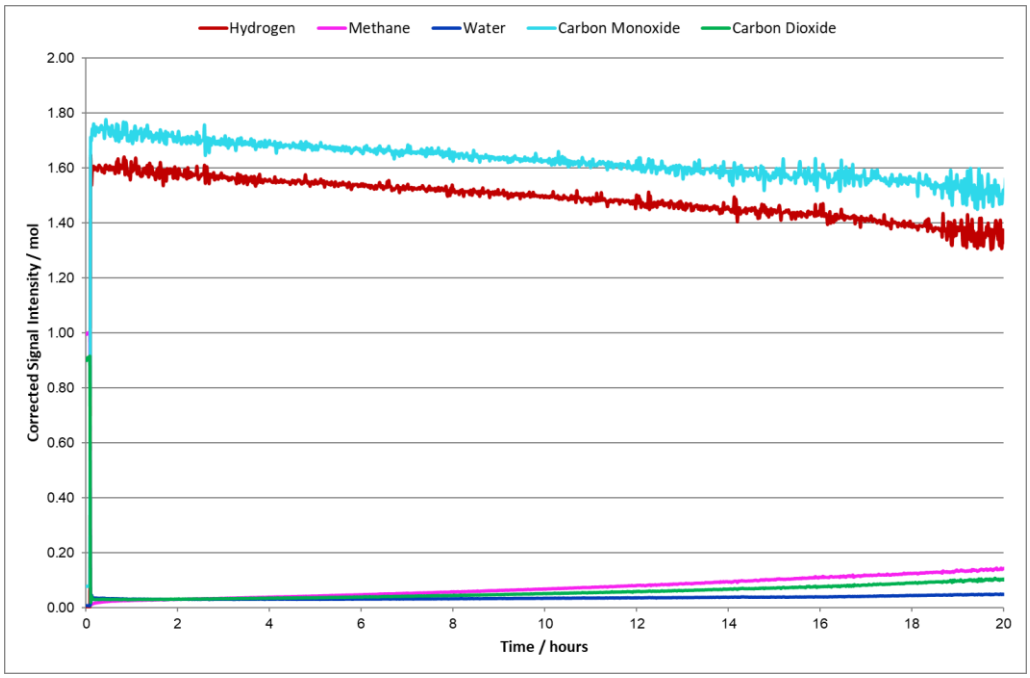

Figure 6.11. Isothermal dry reforming over Ni MTW at 900 °C.

It is clear that for dry reforming, the MTW type zeolite is a better catalyst than its MEL counterpart, in terms of both levels of activity and longevity of catalysis.

6.4.3 Dry reforming conclusions

The dry reforming of methane over the MEL and MTW nickel containing materials was carried out. Both materials showed a sudden ‘switch on’ of reforming activity, at approximately 600 °C for the MEL material and at approximately 500 °C for the MTW material. The sudden switch on could be caused by the conditioning or cleaning of the catalyst surface, allowing the active nickel sites to be become accessible. A large difference between the dry reforming capabilities of the materials was seen, with the MTW material consuming almost all of the methane present as the temperature reached 900 °C.

The MEL material on the other hand only consumed up to 40 % of the methane present as the temperature reached it maximum. For the isothermal reactions, the MTW material was shown to outperform the MEL material, with a difference in methane consumption of nearly 70 %. From these results it is clear that the MTW material is far more suited for the catalysis of the dry reforming of methane than the MEL material. This difference in activity could be due to the differences in the channel structures of the materials with the MTW materials possessing channels in only one direction, allowing for a much faster diffusion through the framework.

6.5 Biogas reforming by carbon dioxide

Biogas reforming was carried out as described in Chapter 3.4.3, where the methane to carbon dioxide ratio was 2:1. This more closely simulates the mixture of these gases within naturally occurring biogas, rather than the synthetic mixture in dry reforming.

As with the dry reforming studies in Chapter 6.4, the biogas reforming was conducted under temperature programmed and isothermal conditions.

6.5.1 Temperature programmed biogas reforming

The forward temperature programmed biogas reforming reaction traces for the nickel containing MEL and MTW materials are shown in Figures 6.12 and 6.13.

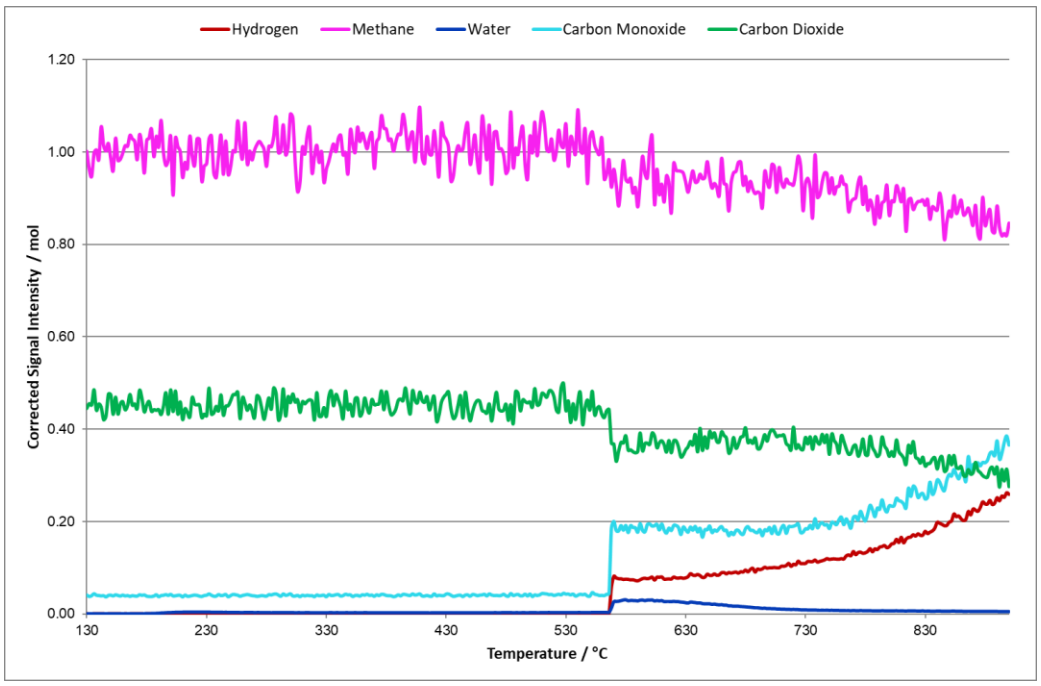

Figure 6.12. Temperature programmed biogas reforming forward reaction for Ni MEL.

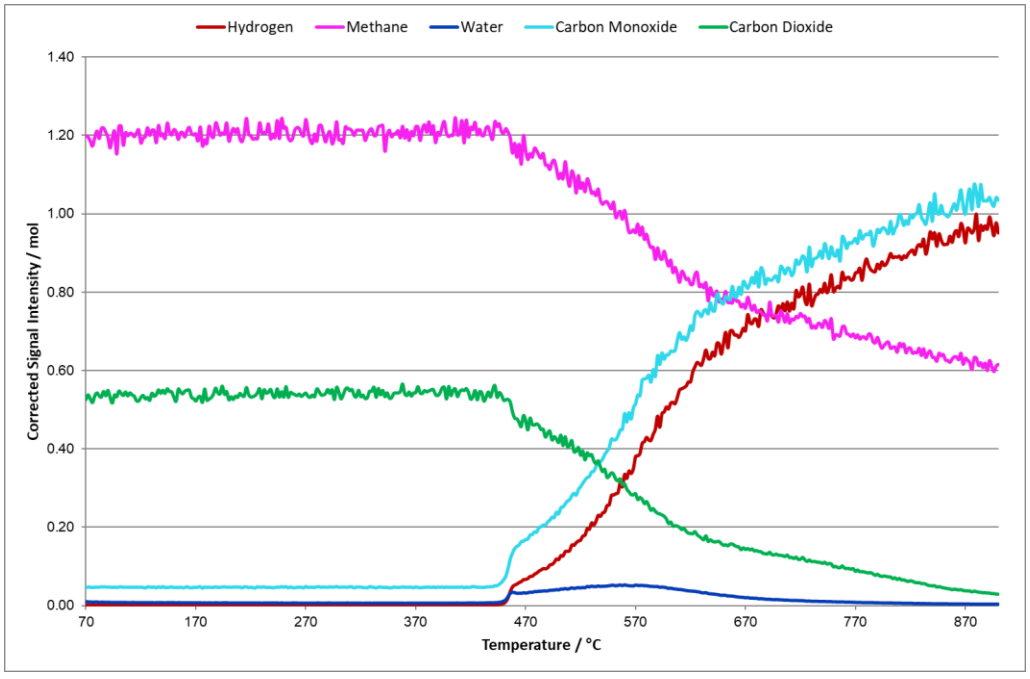

Figure 6.13. Temperature programmed biogas reforming forward reaction for Ni MTW.

Similar to the dry reforming results above, the MTW material shows a higher activity than its MEL counterpart. The MEL reaction trace shows very little reaction occurring with a small amount of reforming and reverse water gas shift after approximately 580 °C. The

activity slowly increases as the temperature nears 900 °C but not to any great extent. The MTW mediated reaction however shows a much higher activity for biogas reforming. As 50% of the methane and nearly all of the carbon dioxide is consumed as the temperature reaches 900 °C the reaction is nearing peak activity. All of the methane is not expected to be consumed during 2:1 simulated biogas reforming as there is not enough carbon dioxide present. A very small amount of the reverse water gas shift reaction is occurring from approximately 450 °C but reduces as the temperature increases.

The reverse reaction profiles are shown in Figures 6.14 and 6.15. Again it can be clearly seen that the MEL material has very little activity for biogas reforming which stops after 600 °C.

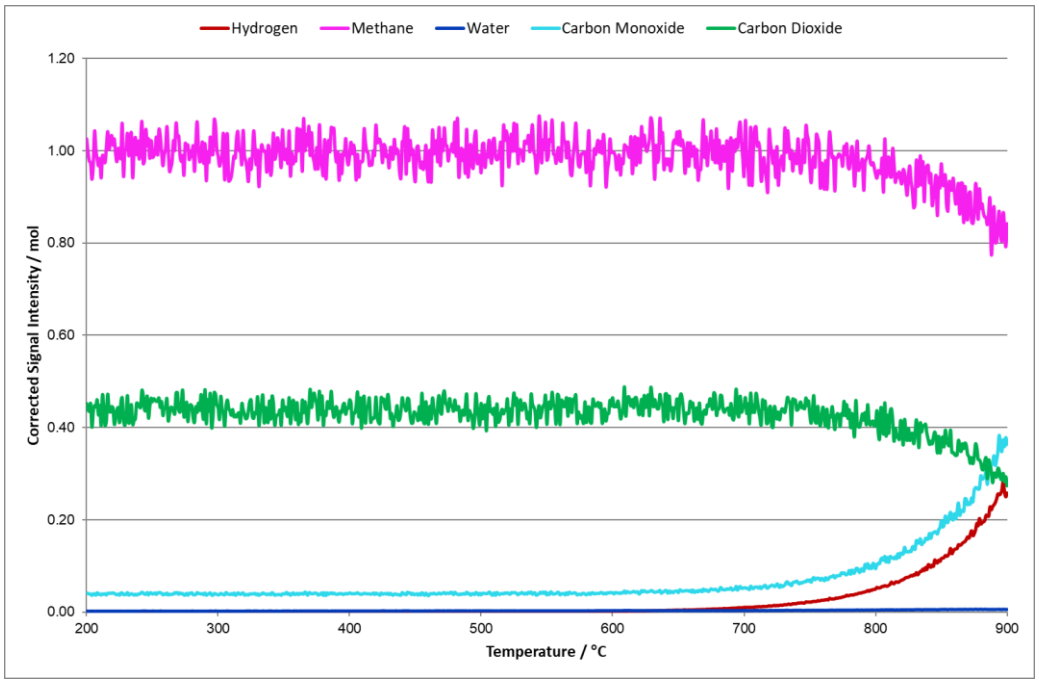

Figure 6.14. Temperature programmed biogas reforming reverse reaction for Ni MEL.

The MTW reverse reaction however, shows a very similar profile to that of the forward reaction, showing that the hysteresis in this case is relatively small. The activity of the reforming reaction slowly reduces until it ceases at approximately 400 °C.

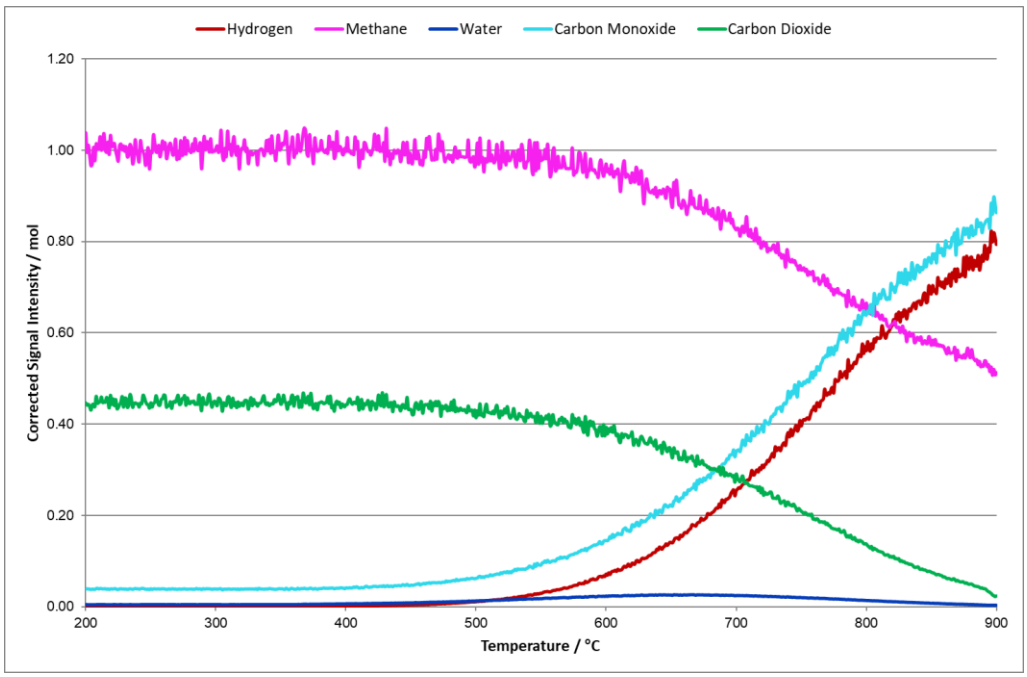

Figure 6.15. Temperature programmed biogas reforming reverse reaction for Ni MTW.

The temperature programmed oxidation to determine the carbon deposition on the catalyst surface was carried out and yielded 0.0733 mg of observable carbon for the MEL material, which is equal to 1.8325 mg of carbon deposited per gram of catalyst used, and 0.0863 mg of observable carbon for the MTW material, which is equal to 2.1575 mg of carbon deposited per gram of catalyst used.

6.5.2 Isothermal biogas reforming

The isothermal biogas reforming at 900 °C reaction profile for the MEL catalyst is shown in Figure 6.16. It can be seen that there is a low level of biogas reforming activity that is decreasing over time. There does not appear to be any reverse water gas shift reaction occurring.

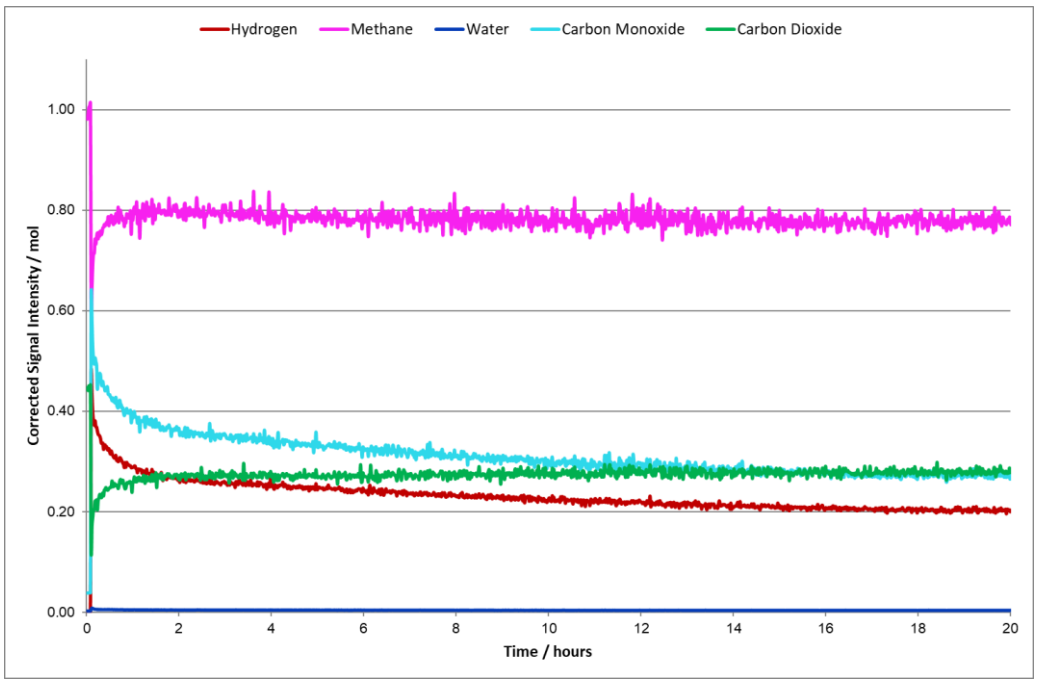

Figure 6.16. Isothermal biogas reforming over Ni MEL at 900 °C.

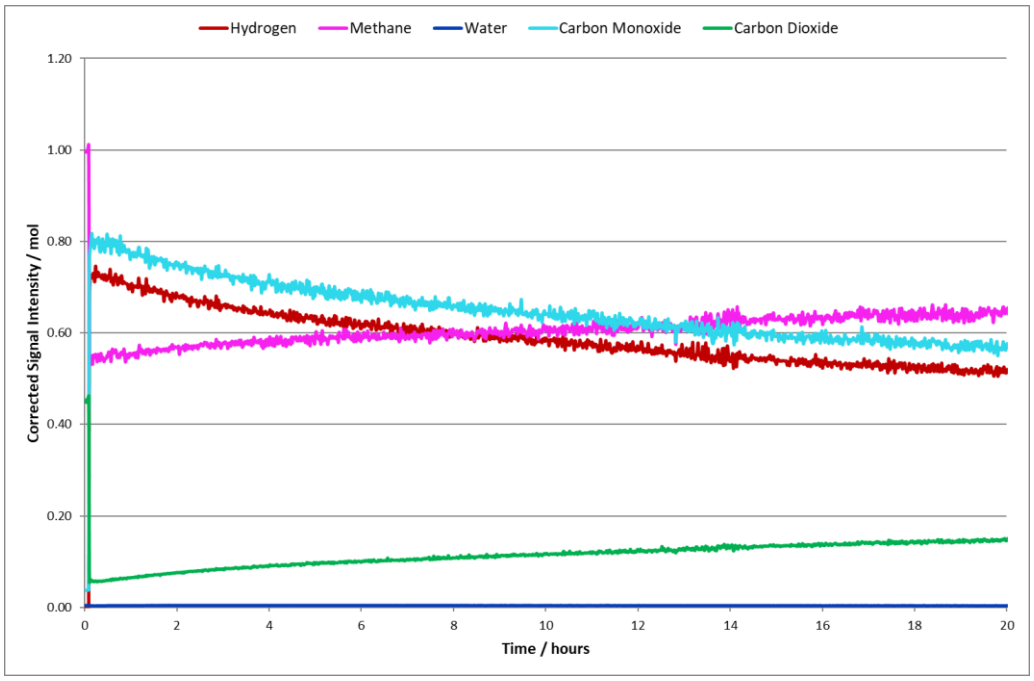

Figure 6.17. Isothermal biogas reforming over Ni MTW at 900 °C.

The isothermal biogas reforming at 900 °C reaction profile for the MTW material is shown in Figure 6.17. There are higher levels of activity for the MTW catalyst than the MEL

counterpart. The catalytic activity decreases over time but a reasonable methane conversion is still present after 20 hours.

The temperature programmed oxidation to yield the carbon deposition was carried out for both catalyst materials. The MEL catalyst yielded 0.1 mg of observable carbon, which is equal to 2.5 mg of carbon deposited per gram of catalyst used, and the MTW catalyst yielded 0.0687 mg of observable carbon, which is equal to 1.7175 mg per gram of catalyst used.

6.5.3 Biogas reforming conclusions

The biogas reforming of methane over the MEL and MTW nickel containing materials was carried out. As with the dry reforming, the MTW material showed a higher reforming activity than the MEL material. For both the temperature programmed and isothermal reactions, both materials showed little difference with the MEL material consuming approximately 20 % of the methane and the MTW material consuming approximately 40 % of the methane. This difference is reforming activity could again be due to the channel system in the MTW material compared to that of the MEL. The straight channel in the MTW material will mean that the diffusion limitations of the reforming will be minimised with the reactants and products being able to enter and exit the channel system more easily.

6.6 Partial Oxidation

Investigation into the reforming of methane via its partial oxidation was carried as per the method in Chapter 2.5.3. The partial oxidation of methane (POx) is one of the more difficult of the reforming reactions to investigate. The balance between partial oxidation and total oxidation (TOx) is an issue many catalysis scientists face.

6.6.1 Temperature programmed oxidative reforming

The temperature programmed partial oxidation of methane reaction traces for the nickel containing MEL and MTW materials are shown in Figure 6.18 and 6.19 respectively.

The MEL material favours the total oxidation reaction with very little hydrogen production even at high temperatures. It is clear that total oxidation is occurring due to the presence of the water signal. There may be a slight occurrence of the reverse Boudouard reaction at high temperatures leading to the formation of carbon monoxide.

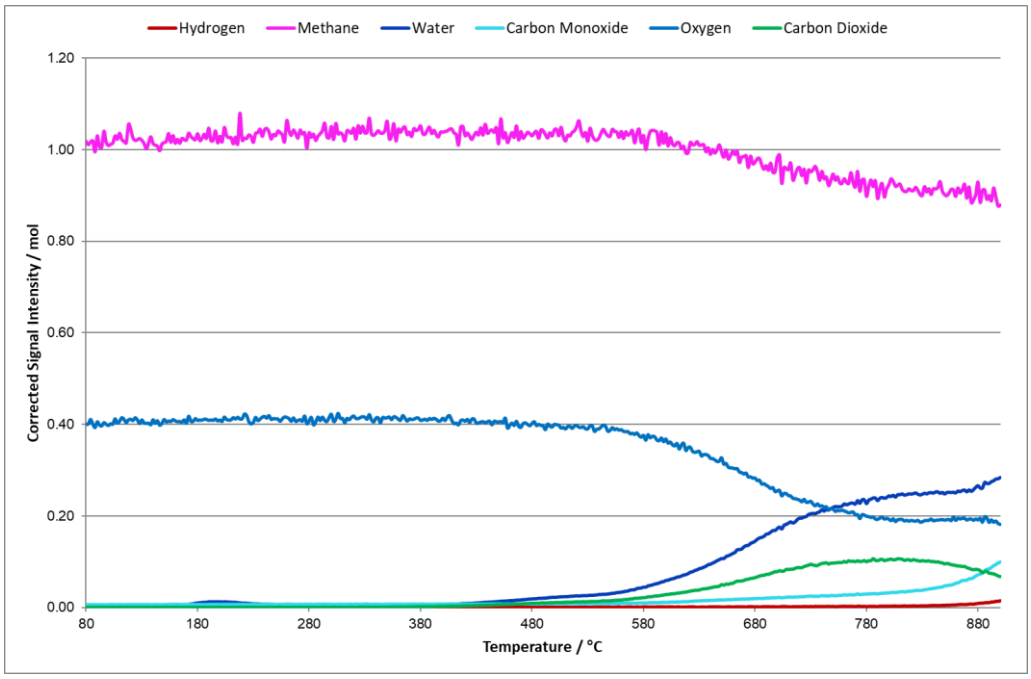

Figure 6.18. Temperature programmed POx forward reaction over Ni MEL.

The MTW material on the other hand shows a preference towards total oxidation at lower temperatures with a sudden change to partial oxidation at approximately 800 °C. A significant percentage, of the methane is being converted to hydrogen and carbon monoxide as the temperature reaches 900 °C.

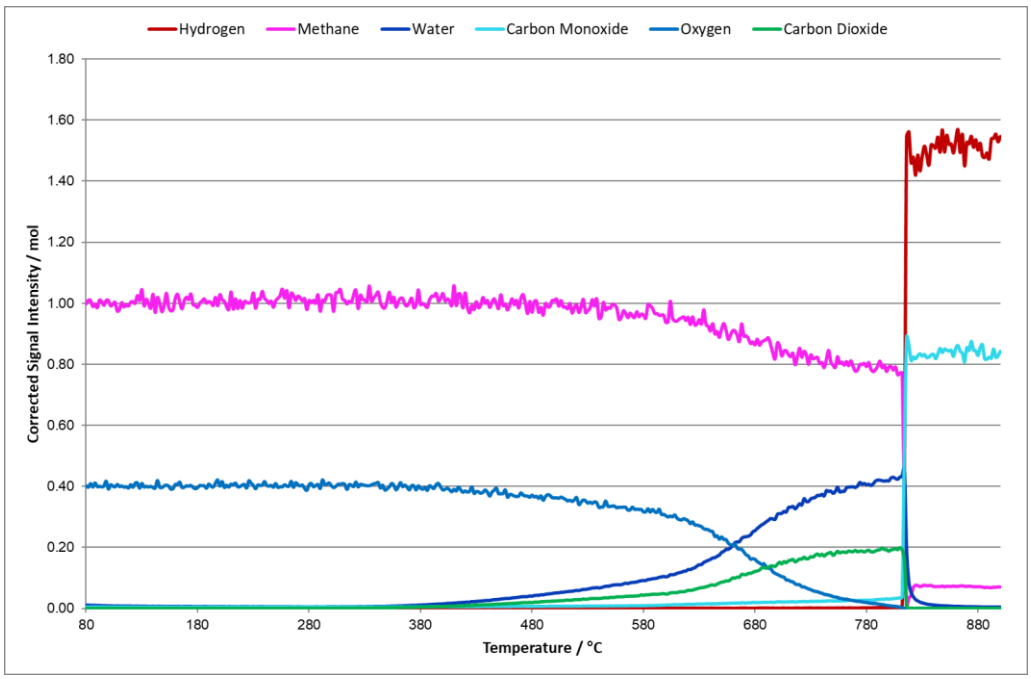

Figure 6.19. Temperature programmed POx forward reaction over Ni MTW.

The reverse temperature controlled POx of methane reaction profiles for both materials are shown in Figure 6.20 and 6.21.

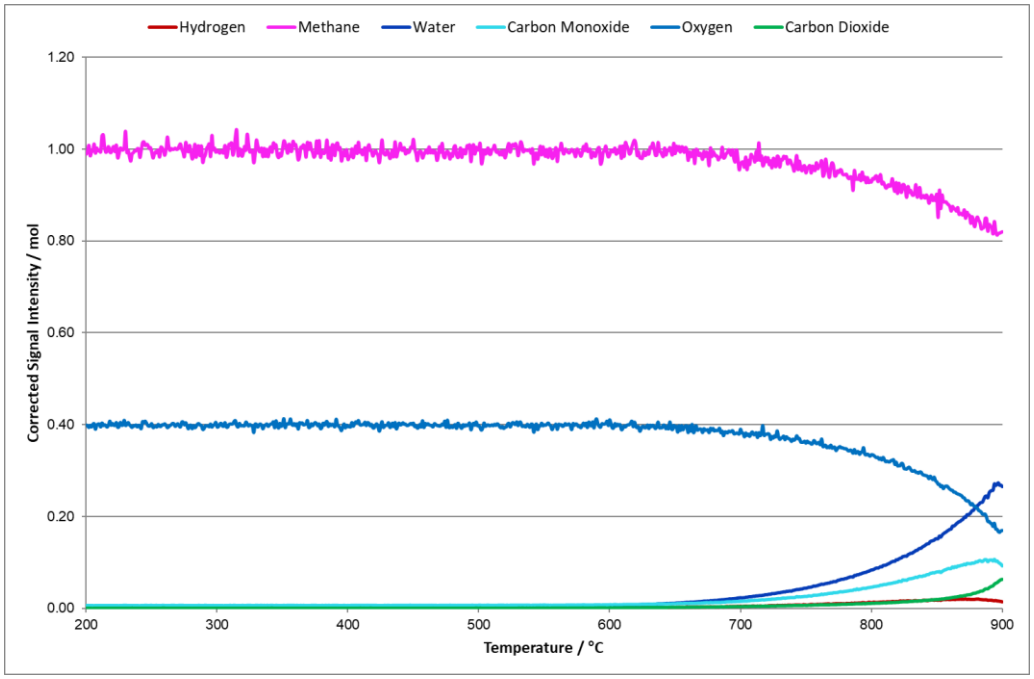

Figure 6.20. Temperature programmed POx reverse reaction over Ni MEL.

It is clear that the MEL material is not active for the partial oxidation of methane even after being heated to 900 °C. The low level activity the material shows towards total oxidation has diminished after 600 °C.

The MTW material on the other hand retains a relatively high activity towards partial oxidation down to 800 °C after which the POx activity decreases as the TOx activity increases. That is until approximately 675 °C where all activity ceases.

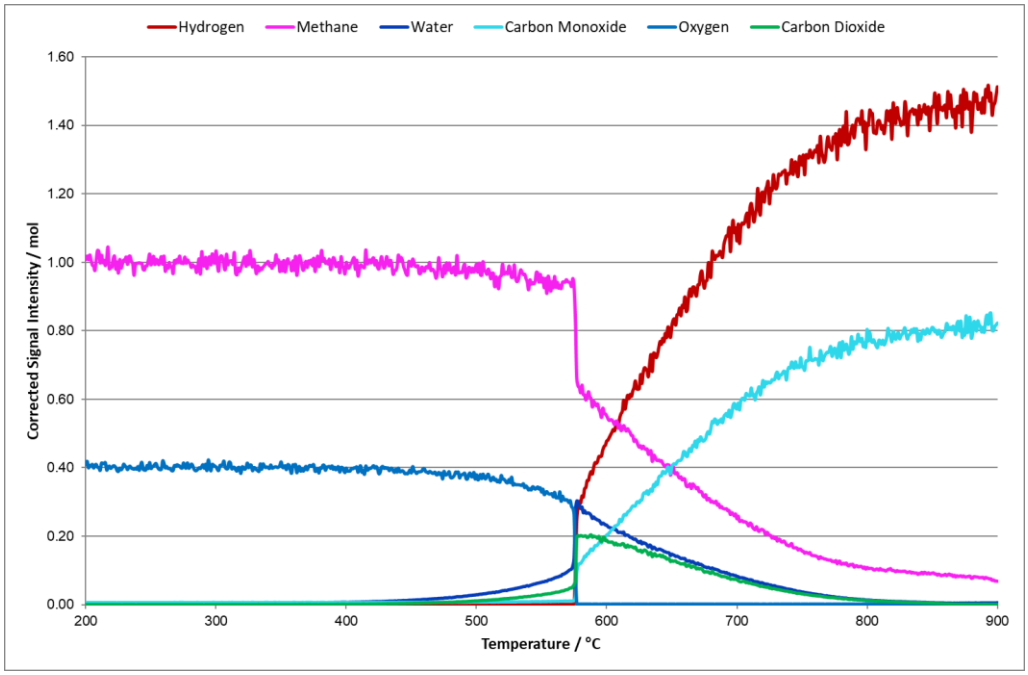

Figure 6.21. Temperature programmed POx reverse reaction over Ni MTW.

The temperature programmed oxidation reaction to determine the amount of carbon deposition on the catalyst surface were carried out and yielded 0.0468 mg of observable carbon for the MEL material and 0.307 mg for the MTW material.

6.6.2 Isothermal oxidative reforming

The isothermal partial oxidation reforming of methane at 900 °C for the nickel containing MEL material is shown in Figure 6.22. It can clearly be seen that there is no activity towards the partial oxidation reaction and is instead towards total oxidation. This total oxidation activity however is very low level and only approximately 10% of the methane is being consumed. The reverse Boudouard can be seen to be taking place with the evolution of carbon monoxide without the presence of hydrogen.

The isothermal partial oxidation of methane reaction profile for the MTW catalyst at 900 °C is shown in Figure 6.23. The initial activity shown towards the partial oxidation rapidly declines within the first two hours of study, after which the POx activity decreases as the TOx activity increases, this change in regime could be due to the deposition of carbon on the catalyst or it could be that the catalyst itself is being oxidised favouring the total oxidation of the methane. It is interesting to note however that this TOx activity is not as high as the POx activity as a large percentage of the methane is left unreacted.

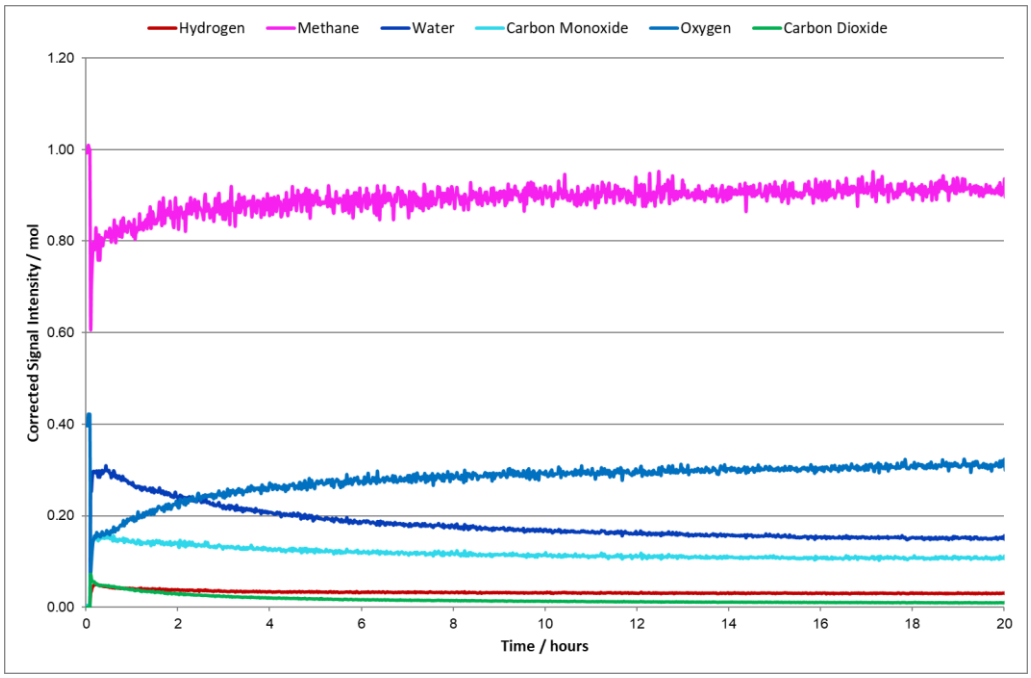

Figure 6.22. Isothermal POx reaction over Ni MEL at 900 °C.

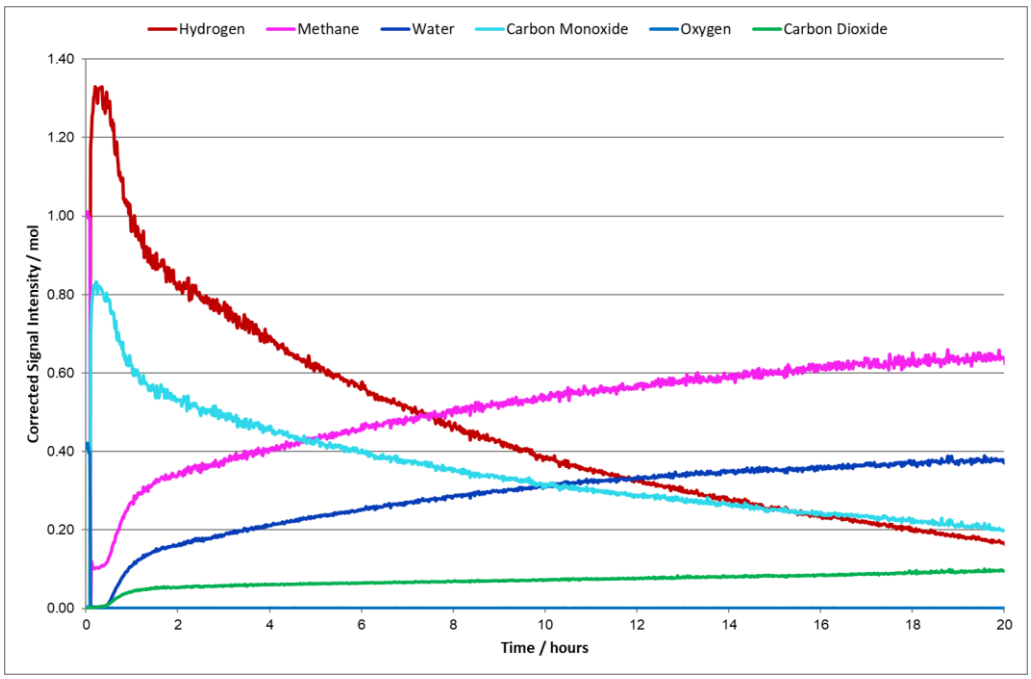

Figure 6.23. Isothermal POx reaction over Ni MTW at 900 °C.

The temperature programmed oxidation reactions to yield the carbon deposition was carried out for both materials, giving values of 0.0789 mg of observable carbon for the MEL material, which is equal to 1.9725 mg of carbon deposited per gram of catalyst used, and 0.0162 mg of observable carbon for the MTW material, which is equal to 0.0405 mg of carbon deposited per gram of catalyst used.

6.6.3 Partial oxidation reforming conclusions

The partial oxidation reforming of methane over the MEL and MTW nickel containing materials was carried out. As with the other reforming reactions, the MTW shows a far superior activity for the partial oxidation of methane than the MEL material. The MTW catalysed reaction showed a 90 % consumption of the methane present as the temperature reached it maximum, whereas the MEL material showed only a 10 % methane consumption. These results are reflected in the isothermal reactions at 900 °C with the MEL material still only consuming 10% of the methane and the MTW material consuming 90%. It is interesting to note that the little activity shown by the MEL material is sustained throughout the 20 hour experiment. In contrast, the MTW material shows a

significant drop off in the oxidative activity with on 40 % of the methane being consumed after 20 hours has elapsed. This drop off in activity could be due to the deactivation of the catalyst though carbon deposition or the oxidation of the catalyst itself. The MTW has been shown to be the far superior catalyst for the partial oxidation of methane, with the difference most likely stemming from the difference in framework channel structures as previous discussed.

6.7 Oxidation of synthesis gas

The oxidation of synthesis gas was again studied to ascertain whether the MEL and MTW nickel containing materials also show the selectivity towards the hydrogen over the carbon monoxide.

6.7.1 Temperature programmed oxidation of syn-gas

The forward temperature programmed oxidation of syn-gas reaction profiles for the nickel containing MEL and MTW catalysts are shown in Figure 6.24 and 6.25.

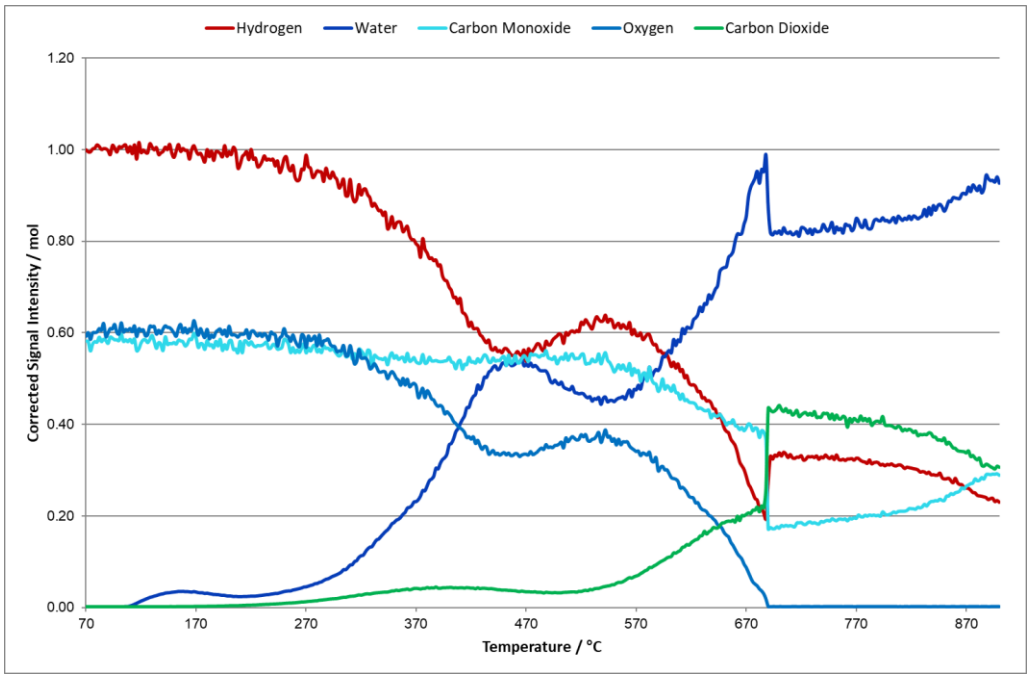

Figure 6.24. Temperature programmed forward syn-gas oxidation over Ni MEL.

It can be seen that in the MEL reaction profile the hydrogen is selectively oxidised over carbon monoxide at lower temperatures. There is a period of reduced activity around 470 °C after which the oxidation resumes and the activity increases as the temperature increases. At approximately 670 °C there is a sudden change in oxidation selectivity from the hydrogen and towards the carbon monoxide, the change in selectivity is brief and thereafter converts back to favouring the hydrogen oxidation. At temperatures above 670 °C the reverse water gas shift reaction is occurring, as shown by the decrease in both hydrogen and the carbon dioxide levels are decreasing and the carbon monoxide level is increasing.

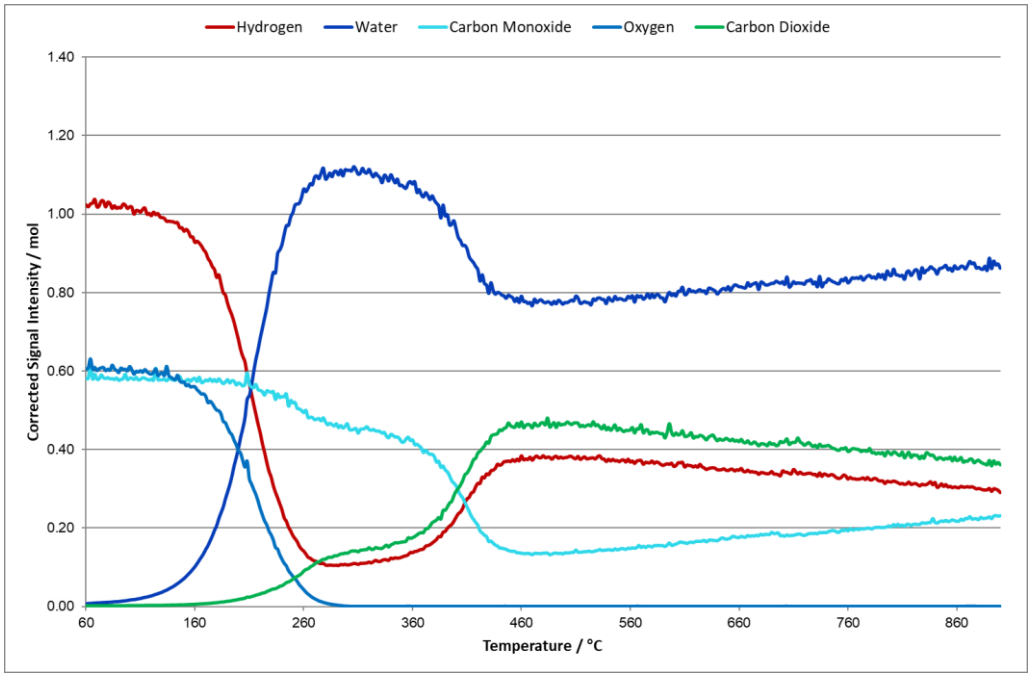

Figure 6.25. Temperature programmed forward syn-gas oxidation over Ni MTW.

The MTW material also shows a selectivity towards the oxidation of hydrogen over carbon monoxide. It does not however show the same dip in activity as the MEL catalyst. For the MTW mediated reaction all the oxygen is being consumed from approximately 300 °C as opposed to approximately 700 °C for its MEL counterpart. At approximately 450 °C there

is a change in the oxidation selectivity in which the carbon monoxide oxidation is favoured over the hydrogen oxidation.

The reverse, cooling, reaction profiles for the MEL and MTW materials are shown in Figures 6.26 and 6.27.

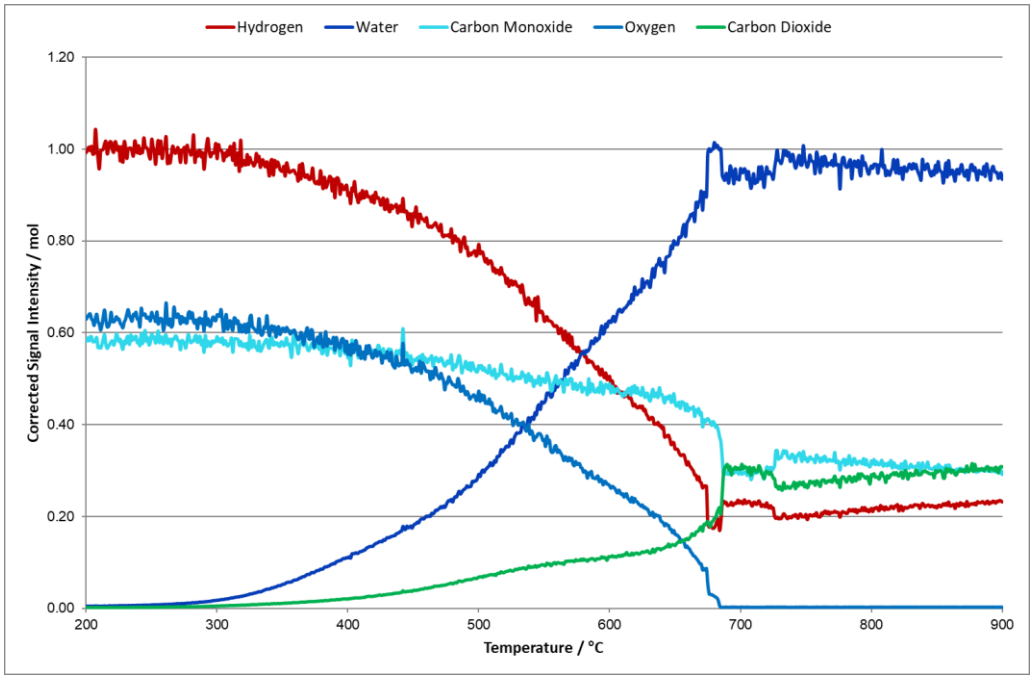

Figure 6.26. Temperature programmed reverse syn-gas oxidation over Ni MEL.

The MEL profile shows a similar profile to the forward reaction if the drop in activity had not occurred. There is a general favour towards the hydrogen oxidation with a slight jump in activity for the oxidation of both hydrogen and carbon monoxide approximately 690 °C.

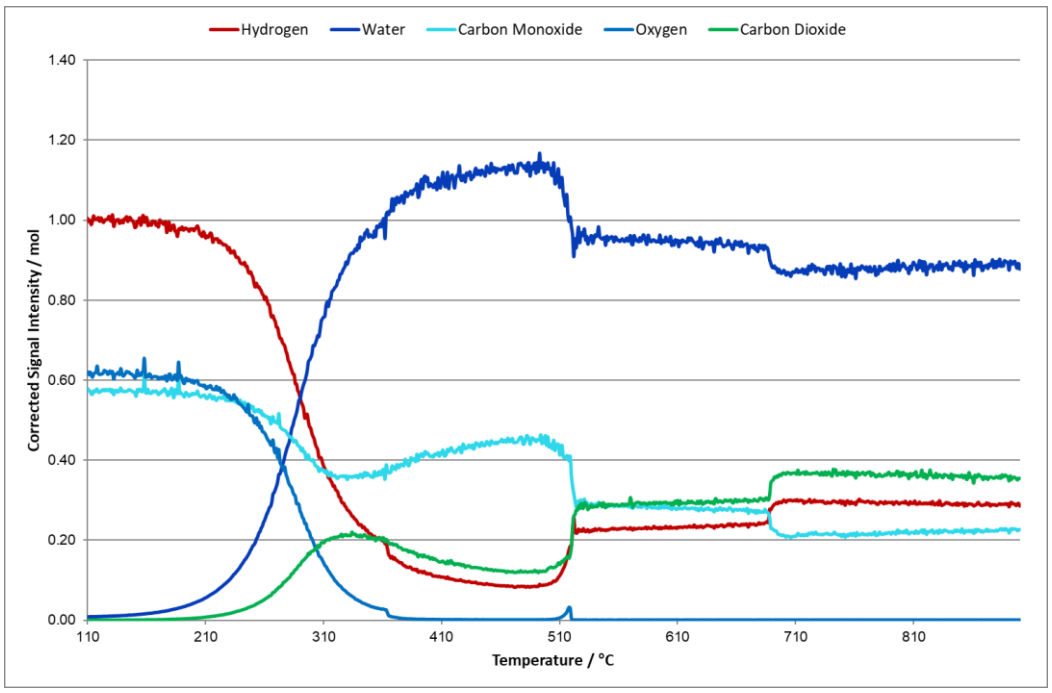

Figure 6.27. Temperature programmed reverse syn-gas oxidation over Ni MTW.

On cooling of the MTW material, the oxidation selectivity shows number of changes. At higher temperatures the selectivity lies with the hydrogen oxidation, but at approximately 700 °C it switches and the carbon monoxide oxidation is favoured. That is until approximately 510 °C, at which point the selectivity changes again to favour the hydrogen oxidation. There is also a moment of brief activity reduction at 510 °C at which all the oxygen is not consumed. As this change in selectivity and reduction in activity occur at the same time it is clear that this selectivity changing is not an immediate process and may involve a change to the surface chemistry, which was much slower at 510 °C than at 700 °C than on the previous switching of selectivity.

The temperature programmed oxidation of the materials to ascertain the amount of carbon on the catalyst surface was carried out for both materials. The MEL catalyst yielded 0.0525 mg of observable carbon, which is equal to 1.3125 mg of carbon deposited per gram of catalyst used. The MTW material yielded 0.0174 mg of observable carbon, which is equal to 0.435 mg of carbon deposited per gram of catalyst used.

6.7.2 Isothermal oxidation of syn-gas

The isothermal reaction for the oxidation of syn-gas was studied at 250 °C as opposed to the 900 °C used for the other reforming reactions. This is due to the fact that at 250 °C all three zeolite catalysts studied in this thesis showed a selectivity towards hydrogen oxidation at this temperature, and there was an intrigue to see if this selectivity and activity could be maintained over 20 hours.

The reaction profile of the isothermal oxidation of syn-gas at 250 °C over the MEL catalyst is shown in Figure 6.28.

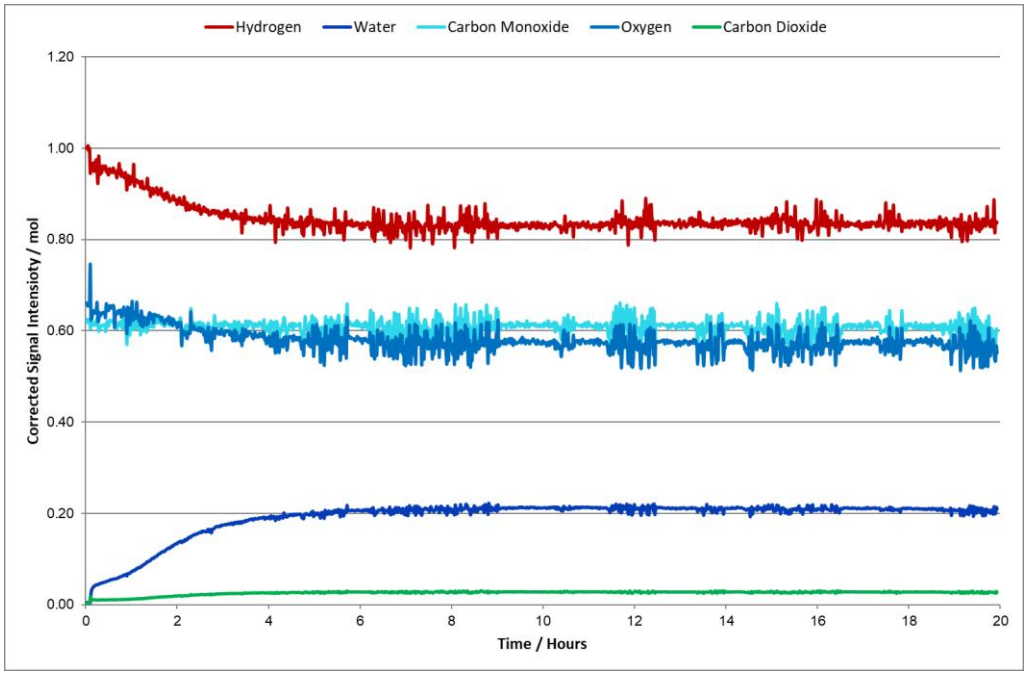

Figure 6.28. Isothermal syn-gas oxidation over Ni MEL at 250 °C.

The isothermal reaction profile for the MEL material shows a selectivity towards the hydrogen, seen from the larger percentage of hydrogen consumed as opposed to carbon monoxide. The signals for all gases within the reaction show a fluctuation rather than a flat line, which is a consequence of the instrumentation and not the reaction. It can be seen that all the oxygen is not consumed in this reaction, however the activity that is present is sustained throughout the 20 hour experiment.

The isothermal reaction profile for the oxidation of syn-gas over the nickel containing MTW catalyst at 250 °C is shown in Figure 6.29.

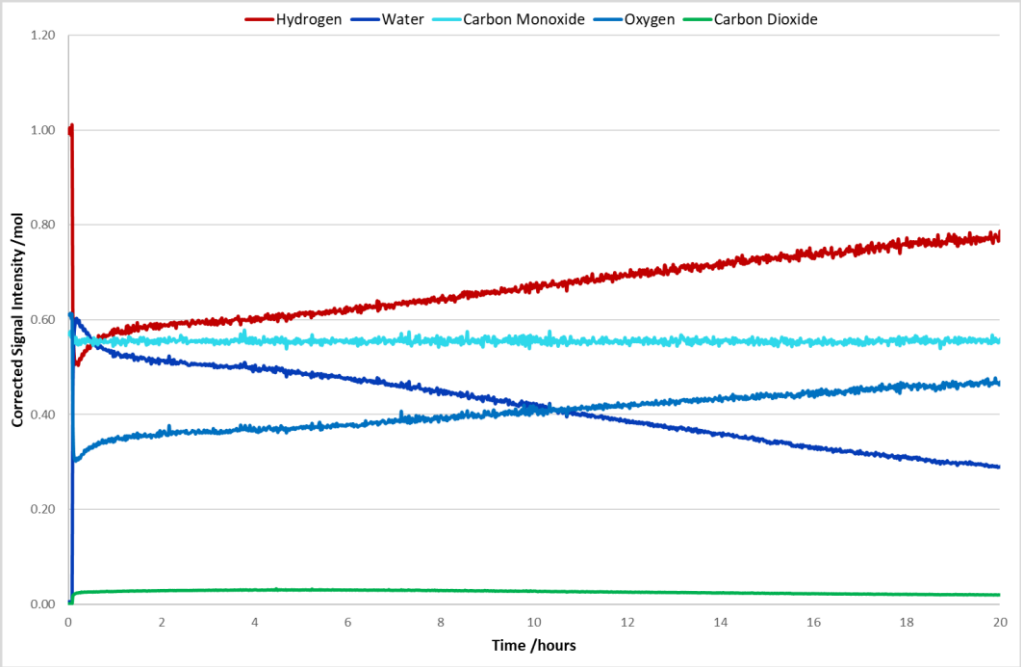

Figure 6.29. Isothermal syn-gas oxidation over Ni MTW at 250 °C.

The isothermal reaction profile for the MTW material again shows a selectivity towards the hydrogen oxidation with very little of the carbon monoxide being oxidised. Approximately 50% of the oxygen is consumed. As time elapses the activity of the oxidation decreases substantially, however some hydrogen oxidation remains after 20 hours of reaction time.

The temperature programmed oxidation was carried out on both materials to ascertain the amount of carbon deposition on the surface of the catalysts. This analysis yielded 0.0234 mg for the MEL material, which is equal to 0.585 mg of carbon deposited per gram of catalyst used, and 0.0401 mg for the MTW material, which is equal to 1.0025 mg of carbon deposited per gram of catalyst.

6.7.3 Oxidation of syn-gas conclusions

The oxidation of syn-gas over the MEL and MTW nickel containing materials was carried out. Both the MEL and MTW materials show a selectivity towards the oxidation of the hydrogen in the syn-gas mixture over the carbon monoxide, evidenced by the evolution of water without the evolution of carbon monoxide, i.e. not the reverse water gas shift reaction. The MEL material shows a consumption of 80 % of the hydrogen and the MTW material a 70 % consumption, as the temperature reaches the maximum. The isothermal reactions at 900 °C showed only a 20 % hydrogen consumption over the MEL material, which remained relatively stable over the 20 hour reaction time. The MTW material showed a 50 % hydrogen consumption which steadily decreased to 20 % after the 20 hours had elapsed, indicating the catalyst is becoming deactivated, most likely by carbon deposition or slow oxidation of the catalyst itself.

6.8 Conclusions

Two nickel containing zeolites were synthesised using the hydrothermal method, an MEL type zeolite and an MTW type zeolite. The catalytic activity of both materials for a variety of methane reforming reactions and the oxidation if synthesis gas was tested.

Overall the MTW material appears to be a superior catalyst showing a general higher activity than its MEL counterpart which shows little or no activity for the reforming of simulated biogas, dry reforming of methane and for the partial oxidation of methane. AS previously mentioned it is postulated that this difference in activity is due to the difference in the channel systems of the two materials, with the MEL having a multi-channel system and the MTW having a single directional channel system. In the MEL framework, reactant gaseous species are more likely to become trapped between the perpendicular channels, whereas in the MTW material the gaseous species can only diffuse through in one direction.

As with the nano MFI material studied in Chapter 5, both the MEL and MTW materials show a low temperature selectivity for the oxidation of hydrogen over carbon monoxide.

This study confirms that the framework structure of the zeolite plays an important role in the catalysis and does not merely act as a support for the active nickel metal.

6.9 References

1. Frontera P, Macario A, Aloise A, Crea F, Antonucci P, Nagy J *et al*. Catalytic Dry-Reforming on Ni–Zeolite Supported Catalyst. Catal Today. 2012;179(1):52-60.

2. Frontera P, Macario A, Aloise A, Antonucci P, Giordano G, Nagy J. Effect of Support Surface on Methane Dry-Reforming Catalyst Preparation. Catal Today. 2013;218-219:18-29.

3. Exxon Mobil Oil Corp. US Pat. 3709979A. 1973.

4. Exxon Mobil Oil Corp. US Pat. 3702886A. 197.

5. Bibby D, Milestone N, Aldridge L. Silicalite-2, A Silica Analogue of the Aluminosilicate Zeolite ZSM-11. Nature. 1979;280:664-665.

6. International Zeolite Association. Database of Zeolite Structures [Internet]. 2015. Available from: http://www.iza-structure.org/databases/

7. Hickson DA. UK Pat Appl. GB 2079735A. 1981.

8. Whittam TV. Eur Patent Appl. EPA 0059059. 1982.

9. Sumitani K, Sakai T, Yamasaki Y, Onodera T. US Pat. 4557919. 1985.

10. Barow TM. Eur Pat Appl. 162719. 1985.

11. Exxon Mobil Oil Corp. US Pat. 4391785A. 1981.

12. Wang L, Zhu S, Shen M, Tian H, Xie S, Zhang H *et al.* Fractal MTW Zeolite Crystals: Hidden Dimensions in Nanoporous Materials. Angew Chem Int Edit. 2017;56(39):11764-11768.

7.0 Conclusions and Further Work

7.1 Conclusions

Two nanosized materials were synthesised via the clear-solution method with two different structure directing agents, a tetrapropylammonium salt and a methyl tributylammonium salt. The mechanism of formation of these nanosized zeolites was investigated through the implementation of three characterisation techniques, X-ray diffraction, solid state NMR and dynamic light scattering. X-ray diffraction studies showed that the TPA template is able to form the MFI framework over a shorter time period than the MTBA template, however, solid state NMR studies revealed that the MTBA mediated reaction yielded more crystalline material with fewer framework defects. From these results it is difficult to make definitive conclusions as to the mechanism of formation of these nanozeolites, however it is likely that a mechanism of spontaneous rapid crystallisation is occurring. The XRD patterns showing peaks at early timepoints could be due to the presence of the aggregates or they could be due to a very rapid crystallisation, however, the stability of the FWHM data indicates a rapid crystallisation mechanism is occurring. The solid state NMR investigations disagree with the process of the aggregation mechanism, due to the presence of a large Q4 silicon peak which is inconsistent with the presence of aggregates in the reaction mixture. The DLS results for the MTBA mediated indicate a wide distribution of particle sizes which could be attributed to the aggregates, however on analysis of the average particle sizes for each timepoint the TPA mediated reaction suggests a mechanism of spontaneous crystallisation. On analysis of the data as a whole, it is concluded that the most likely mechanism of formation for the nanosized zeolite during a clear-solution synthesis is that of spontaneous crystallisation. However, definitive conclusions cannot be made, further work into the area needs to be carried out, outlined in Chapter 7.2.

Four nickel containing zeolite catalysts were formed through the implementation of either a clear-solution or hydrothermal synthesis method. These materials were formed via sodium

or potassium intermediates which were then ion-exchanged and calcined to yield the final nickel containing materials.

The effect of particle size on the reforming of methane was probed using nano and micron sized nickel ‘doped’ MFI zeolites. The nano sized material was shown to have a higher catalytic activity towards the partial oxidation of methane opposed to the micron sized material. However, this activity was reversed for biogas reforming, with the micron sized material showing a higher level of catalysis. From these results it is clear that the reduction in particle size of a zeolite catalysts does not always infer an improvement to the performance, it is dependent upon the reaction undergoing catalysis. The nano sized material showed an interesting property during the partial oxidation of methane studies in which it displayed a selectivity towards the oxidation of methane and hydrogen. This selectivity was investigated by the oxidation of synthesis gas. The results of this syn-gas study showed that at most temperatures the nanosized MFI zeolite shows a selectivity towards the oxidation of hydrogen over carbon monoxide, with the oxidation of such occurring at low temperatures of approximately 200 °C. The differences seen between the two materials is most likely due to the availability of nickel sites, stemming from the difference in particle size, and the diffusion limitations imposed by the different frameworks. From the results presented, it is concluded that the optimum particle size for the MFI type catalyst lies somewhere between the nano and micron sized materials investigated, however the control over the particle size may be difficult to achieve.

The effect of changing the zeolite framework type was studied using nickel containing MEL and MTW nickel ‘doped’ zeolites, in addition to the previous MFI particle size zeolite catalysis study. The MTW material showed a much higher methane reforming activity than the MEL material, which showed little or no activity for the reforming reactions. The difference in catalytic activity shown by the two materials is most likely due to their different channel systems which will have a significant effect on the diffusion pathways for the reactant gaseous molecules.

On comparison of the MTW and MFI catalytic capabilities, it is clear that for biogas reforming the micronsized MFI zeolite is the superior catalyst. For the partial oxidation of methane, the MTW material shows the greatest reforming activity however, this activity cannot be sustained for a prolonged time period. The MTW, MEL and nano MFI materials show a selectivity towards the oxidation of hydrogen over carbon monoxide in the oxidation of syn-gas. However, at 250 °C the nanosized MFI material shows a far better ability to catalyse the oxidation of hydrogen, which can be sustained over prolonged periods. The differences seen, again, will most likely be due to the availability of the nickel sites and the diffusion pathways within the materials.

The results of this study show that the change in zeolite framework type does have a large impact on the level of catalysis activity exhibited by the material. These nickel containing zeolites show a great potential for the catalysis of methane reforming, however, one material may not be suited to all types of methane reforming.

7.2 Further Work

The studies into the mechanism of formation of the nanozeolites could be further investigated by solid state NMR to probe the local environments of ^{14}N and ^{61}Ni. The ^{14}N spectra would allow the local environment of the central nitrogen atom within the template to be probed, gaining further insight into formation of the framework. The ^{31}Ni spectra would allow insight into the location of the nickel within the framework. Rotational echo double resonance (REDOR) NMR could be used to further characterise the zeolite framework, the entrained SDA and the relationship between them. The implementation of X-ray absorption fine structure (XAFS) would allow the nickel in the framework to be further investigated to gain insight into the oxidation state and the local environment.

The use of different symmetric and asymmetric structure directing agents could be used to understand the effect of the SDA conformation on the final product and the mechanism of formation. It may be that different SDAs have different formation mechanisms, with some

showing spontaneous crystallisation, some showing the aggregation mechanism and other potentially a mixture if the two.

Further investigations into the control of the final particle size could be carried out. This would not only allow further understanding of the mechanism of formation but would also allow further investigations into the effect of particle size on the catalytic capabilities of the material. The control of the particle size to yield a product in the range between the micron and nano materials presented here may prove difficult.

Zeolite catalysis could be further investigated by again changing the zeolite types, as there are now 239 confirmed zeolite types this leaves many possibilities for an improved catalyst to be discovered. A different active metal, such as platinum or palladium, could also be investigated, however the cost-benefit analysis would have to determined. For the materials studied in this thesis, the steam reforming capabilities could also be investigated.